Coherence and adiabaticity in dressed matter waves

Alessandro Zenesini

Advisor:
Prof. Ennio Arimondo

Università degli Studi di Pisa
Dipartimento di Fisica *E. Fermi*
Corso di Dottorato in Fisica
XX Ciclo
December 2008

A mio nonno Luigi

"...one of the strongest motives that lead men to art and science is escape from everyday life with its painful crudity and hopeless dreariness, from the fetters of one's own ever-shifting desires. A finely tempered nature longs to escape from the personal life into the world of objective perception and thought."

Albert Einsten

Acknowledgements

Before arriving in Pisa, my undergraduate studies had been about thermonuclear fusion and my subject was MK temperatures, not nK! I have to thank Prof Arimondo who gave me the possibility to work on what I like most in physics, quantum mechanics. This big jump into the cold was enormously smoothed by Oliver Morsch and Donatella Ciampini who helped me to overcome theoretical and experimental difficulties. And if the hard job in the lab has been done always with enthusiasm, professionalism, fun and friendship, I have to thank my colleagues-friends-brothers Carlo Sias and Hans Lignier. In less than three years of this job we were able to do a huge amount of work, suffering, discussing (about physics, cinema, music, politics, life ...), teaching and learning, always together, inside and outside the lab. I thank also Matteo Cristiani, an incredibly clear and professional helper in my first year of the PhD. I don't want to forget Jagoda Radogostowicz, Yesh Pal Singh, Sandro Wimberger. After the fire that *smoked* our setup in 2005, nothing could have been possible without all the persons of the Pisa team, Enrico Andreoni and Nicola Puccini, Prof. Maria Allegrini and Prof. Francesco Fuso, Francesco Tantussi and collaborators. I acknowledge Prof. Martin Holthaus and André Eckardt for the enlightening discussions we had, especially during their visit in Pisa in 2007. I'm very thankful also to Prof Steven Rolston and all his group at the University of Maryland who hosted me in their lab for four months in the USA.

But life is not only job and I want to thank my flatmates who bore my schedule and terrible habits: the pedantic Massimo, the panzerotto queen Marina, the angelic Angela, the polisher Francesca, the shepherd Giada, the night-eater Pasquale and the smoker Peppe. When there was something to celebrate or to forget, my friends in Pisa, Padova (EISST) and Treviso were always ready for a drunk evening or a healthy trip together.

The last but the most important component is all my family who supported me in every moment. And especially, my grandfather Luigi who has taught me the patience and the importance of life with his almost centenary experience.

Contents

Introduction

Since the early days of quantum mechanics "toy models" have been used to explain and teach the counterintuitive phenomena of the quantum world. The possibility to solve analytically a number of simple problems showed how complex processes were related to basics ideas. The "particle in the box" or the potential barrier are only two examples. Till the end of the last century, however, it was almost impossible to realize these simple toy models because of the temperature and energy scale of the macroscopic devices used for the experiments. The single quantum object under investigation was not sufficiently decoupled from the external world and defects and decoherence affected the direct observation of the quantum process.

The experimental realization of quantum degenerate states in ultracold atoms gases in the 1990's has opened the possibility to have few body systems isolated from external perturbations and at temperatures close to absolute zero. Under these conditions the Heisenberg indetermination principle becomes the only limit. Different tools have been developed for the study of dynamic behavior (i.e. for simulation of vortices in superfluidity) and of spatially periodic systems (i.e. for the simulation of crystals). These techniques allow physicists to manipulate a small number of quantum particles and to use them in a huge variety of experiments where it is possible to measure and characterize fundamental phenomena. For example, astounding examples were achieved in the last ten years by using optical lattices in the study of tunneling. The possibility of easily changing the parameters (depth, lattice constant etc.) of a defect-free potential permits one to observe, for example, Bloch oscillations and the quantum phase transition into a Mott-insulator regime.

An interesting subject that has not been studied extensively in experiments so far is that of strongly driven quantum systems, where a time-dependent (in particular periodic) perturbation is introduced in the system in order to probe it or to change its fundamental properties. The theoretical approach for these phenomena includes the external driving inside one of the parameter of the unperturbed system similarly to what is done in solid state

physics for the renormalizazion of the mass of an electron in a crystal. The parameter becomes variable and the problem can be treated in a easier way.

In this thesis I will present the results obtained concerning the possibility to adiabatically modify the quantum process of tunneling using an external periodical forcing on the optical potential. By periodically moving the lattice backwards and forwards, the fundamental tunneling properties of the atoms inside the lattice can be adiabatically changed and the system can be carried into novel regimes impossible to reach with static techniques. In particular, for our system the renormalization approach needs to be expanded to a macroscopic coherent ensemble of atoms and it becomes natural to refer to it as a *dressed matter wave* as suggested in [28]. I will show how this idea can be realized and the matter waves can be adiabatically dressed without losing the quantum coherence of the ensemble also during a quantum phase transition. These results are a step toward a clear possibility to investigate simple process in the driven regime to and use the experimental realization as the quantum simulation of a system that is too complex to solve analytically or numerically.

Because of the extreme low temperatures needed for the realization of the experiments proposed, the principal tool of our investigation is an ultracold ensemble of bosonic atoms. In **chapter one** I introduce the theory of Bose Einstein condensation, with a brief summary of the theoretical background that underlies the laser and evaporative cooling of an atomic cloud. Finally the setup built in Pisa for the realization of the experiments is explained in detail.

In **chapter two** the mathematical treatment developed for periodical potentials in quantum mechanics is introduced. The experimental realization and the calibration of optical lattices are also extensively presented.

The first part of **chapter three** is dedicated to the theoretical approach of periodically driven systems in order to introduce the suppression of tunneling. The second part describes our experimental demonstration of this phenomenon for two different shapes for the driving force.

Chapter four contains an extensive theoretical and experimental analysis of the idea of adiabaticity in strongly driven one-dimensional quantum systems. I present numerical simulations of the problem and the different tests realized in order to find the ranges of the different parameters where driving can be applied maintaining the coherence of the system and without releasing energy. The final part of the chapter is dedicated to some examples of experimentally created regimes where the driving was adiabatically

applied to one-dimensional systems.

The results of Chapter 3 and 4 on the suppression of tunneling and the adiabaticity of the driving, suggest the application of this technique to the Mott-Insulator transition. Therefore in **chapter five** I introduce the properties of the Superfluid-Mott Insulator transition in the static regime and particular attention is paid to those features that will be useful for verify its achievement in the driven system. Moreover I present a novel procedure for the characterization of the compressibility of bosonic system close to the phase transition.

In **chapter six** I demonstrate the high degree of control we have achieved with the dressed matter waves by extending the adiabaticity problem to the two- and three-dimensional lattices. Particular care is dedicated to the parameter ranges and to their dependences on the dimensionality of the system. Finally the experimental realization and the characterization of the superfluid—Mott-insulator transition in the driven regime are shown.

Chapter 1

Bose Einstein Condensation in dilute alkali gases

Bose Einstein condensation is the starting point of our investigation being an example of a system whose temperature is close to absolute zero. In this chapter I will introduce the main ideas for the theoretical decription and the experimental realization of Bose Einstein condensation (BEC). After a review of basic concepts about the theory of degenerate bosonic gases, I will explain the techniques needed for the trapping and cooling of an atomic ensemble. The last part of the chapter contains a detailed overview of the apparatus I helped to rebuild in Pisa after the fire in April 2005, and of the experimental sequence which allows us to obtain Bose Einstein condensates.

1.1 The statistical approach

Phase transitions are among the most interesting macroscopic phenomena related to quantum mechanics. At the beginning of the 20th century A. Einstein ([31], [32]) and S.N. Bose ([6]) predicted that an ensemble of cold bosons at a certain temperature could undergo a phase transition purely related to statistical considerations on the indistinguishability of quantum particles in a symmetric eigenstate, the so called Bose-Einstein statistics.

For non-interacting bosons at a temperature T, the mean occupation number of a single state u is

$$n(\varepsilon_u) = \frac{1}{e^{(\varepsilon_u - \mu)/k_B T} - 1} \tag{1.1}$$

where ε_u is the energy of the level and μ the chemical potential. The total number of atoms is the sum $N_{tot} = \sum_u g_u n(\varepsilon)$ over the occupied states by

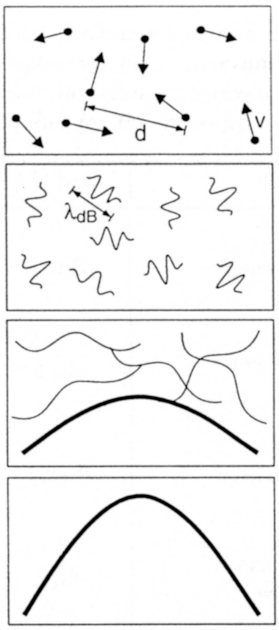

Figure 1.1: When the temperature of the gas is high enough, the quantum nature of the particles can be neglected and the system obeys to the Boltzmann statistics. As the temperature decrease, the De Broglie length increases ($\lambda_{dB} = \frac{h}{mv} \propto T^{1/2}$) and when it has the same order of magnitude of the inter atomic distance, the wave functions start to overlap. (From [54])

taking in consideration the degeneracy g_u of each energy level. This sum can be converted to an integral with the condition to separate the contribution from the state N_0 that is pathologically deleted by the integration.

$$N = N_0 + N_{u\neq 0} = N_0 + \int g(\varepsilon_u) n(\varepsilon_u) d\varepsilon_u \tag{1.2}$$

For an ideal system of non-interacting bosons with mass m without an external potential, equation 1.2 becomes

$$N = \frac{1}{e^{\mu/k_B T} - 1} + \frac{V}{\lambda_{dB}^3} \mathrm{g}_{3/2}(e^{\mu/k_B T}) \tag{1.3}$$

where V is the volume occupied, $\mathrm{g}_{3/2}(x)$ is the polylogarithm $\sum_{l=1}^{\infty} x^l/l^{3/2}$ and λ_{dB} is the de Broglie thermal length ($\sqrt{2\pi\hbar^2/mk_BT}$). The critical behavior is given by the divergence in N_0, corresponding to the situation when the number of atoms in the ground state becomes macroscopic. This is equivalent to imposing $N = N_{u\neq 0} = (V/\lambda_{dB}^3)\, \mathrm{g}_{3/2}(1) = 2.612(V/\lambda_{dB}^3)$ at the critical temperature T_c, which gives the condition:

$$k_B T_c = \frac{2\pi\hbar^2}{m} \left(\frac{N/V}{\mathrm{g}_{3/2}(1)} \right)^{2/3}. \tag{1.4}$$

A useful parameter is the so called *phase space density*

$$\rho = \frac{N}{V} \lambda^3 = \mathrm{g}_{3/2}(e^{\mu/k_B T}) \tag{1.5}$$

which can be evaluated from experimental measurements of V, N and T. As the de Broglie length represents the wavelength associated to the wave properties of the particles and ρ is the number of the atoms in a cubic volume of edge λ_{dB}, from a simply phenomenological point of view the condensation takes place when there is a *sufficient* number of atoms in the quantum interaction range.

However in the realistic case we have to consider the atoms trapped in a harmonic potential

$$\begin{aligned} V_{\text{ext}} &= \frac{m}{2}\left(\omega_x^2 x^2 + \omega_y^2 y^2 + \omega_z^2 z^2\right) \\ g(\varepsilon_u) &= \frac{\varepsilon_u^2}{2(\hbar^3 \omega_x \omega_y \omega_z)}, \end{aligned} \tag{1.6}$$

where ω_i are the frequencies in the three spatial directions, usually expressed as $\omega_{ho} = (\omega_x \omega_y \omega_z)^{1/3}$. In that case the critical value of the temperature is

$$k_B T_c = \hbar \omega_{ho} \left(\frac{2N}{\Gamma(3)\mathrm{g}_3(1)}\right)^{1/3} \simeq 0.94\, \hbar \omega_{ho} N^{1/3}, \tag{1.7}$$

where Γ is the gamma function and it is evident how the critical temperature for our experimental realization will depend on the characteristics of the trap used for the confinement.

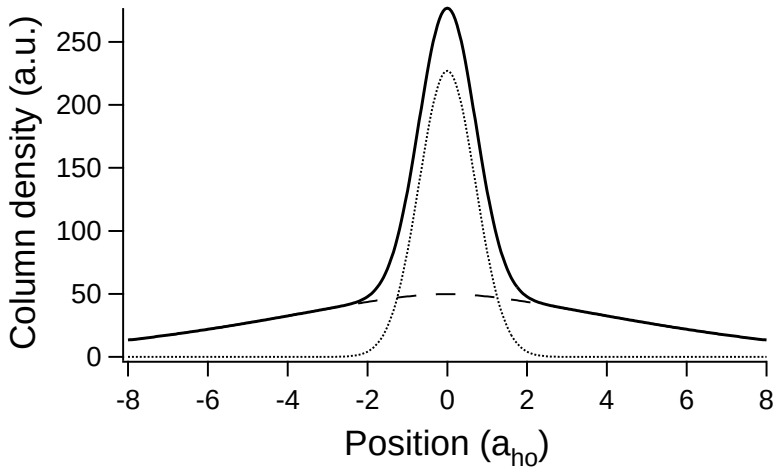

Figure 1.2: Column density as a function of position for a cloud with $T = 0.95T_c$. (dotted line - density of the condensate fraction; dashed line - density of the thermal fraction; continuous line - total density).

For temperatures below T_c the number of atoms in the ground state will increase approaching $T = 0$ and from equations 1.1 and 1.7 the fraction of

condensed atoms can be evaluated as:

$$\frac{N_0}{N} = 1 - \left(\frac{T}{T_c}\right)^3. \tag{1.8}$$

In the experiments this behavior is clearly visible in the different widths of the momentum distributions of the atoms in the condensate fraction and those in the thermal cloud. The condensate fraction is described by the wave function of the ground state of the harmonic trap while the thermal atoms follows the Boltzman distribution. If the confining trap is switched off when the temperature is between 0 and T_c, the distribution of the root-mean-squared velocities of the atoms is the combination of two different contributions (see figure 1.2). The atoms in the thermal cloud have a gaussian distribution with larger width, from which we can evaluate the temperature. The gaussian profile with the narrowest width comes on the contrary from the condensate fraction. More details on Bose-Einstein condensation can be found in [18] and [46].

1.2 The second quantization approach

The first evidence of the BEC phase transition was indirectly observed in Helium mixtures and in superconductors where the strong interations between particles hide the effects of condensation. Only in recent years, after the development of laser cooling techniques, it became possible to observe the condensation in ultra cold gases ([1], [21]).

Up to now we have considered the cases of ideal bosons and confined bosons, but always in the absence of interaction between the particles. In the case of weakly interacting atoms a different theoretical approach is needed. The starting point is a many body Hamiltonian

$$\begin{aligned}\hat{H} = &\int d\mathbf{r}\hat{\Psi}^\dagger(\mathbf{r})\left[-\frac{\hbar^2}{2m}\nabla^2 + V_{ext}(\mathbf{r})\right]\hat{\Psi}(\mathbf{r}) \\ &+ \frac{1}{2}\int d\mathbf{r}d\mathbf{r}'\hat{\Psi}^\dagger(\mathbf{r})\hat{\Psi}^\dagger(\mathbf{r}')V_{int}(\mathbf{r}-\mathbf{r}')\hat{\Psi}(\mathbf{r}')\hat{\Psi}(\mathbf{r}),\end{aligned} \tag{1.9}$$

where $V_{ext}(\mathbf{r})$ is the confining potential and $V_{int}(\mathbf{r}-\mathbf{r}')$ is the two-body interatomic potential. $\hat{\Psi}(\mathbf{r})$ and $\hat{\Psi}^\dagger(\mathbf{r})$ are the boson field operators which create and annihilate a particle at position $\mathbf{r}$, respectively.

Equation 1.9 can be simplified through the mean field approximations. The condensate part $\hat{\Psi}_0(\mathbf{r},t)$ is separated from the bosonic operators

$$\hat{\Psi}(\mathbf{r},t) = \hat{\Psi}_0(\mathbf{r},t) + \hat{\Psi}'(\mathbf{r},t). \tag{1.10}$$

When the temperature of the system is below T_c the number of atoms in the ground state becomes very large. Adding or subtracting a particle from the low energy level does not significantly affect its population. Therefore we can treat $\Psi_0(\mathbf{r},t)$ as complex function rather an operator. Thus equation (1.10) becomes:

$$\hat{\Psi}(\mathbf{r},t) = \Psi_0(\mathbf{r},t) + \hat{\Psi}'(\mathbf{r},t), \tag{1.11}$$

where $\Psi_0(\mathbf{r},t)$ represents the expectation value of the field operator on the ground state and

$$n_0(\mathbf{r},t) = |\Psi_0(\mathbf{r},t)|^2 \tag{1.12}$$

is the condensate density.

If only two-body elastic collisions are considered the only relevant contribution at low energy to the interaction potential can be written as

$$\begin{aligned} V_{int}(\mathbf{r}-\mathbf{r}') &= g\delta(\mathbf{r}-\mathbf{r}') \\ g &= \frac{4\pi\hbar^2 a_s}{m} \end{aligned} \tag{1.13}$$

where a_s is the scattering length for s-wave collisions. The equation of the condensate becomes the *Gross-Pitaevskii* equation ([41] and [73])

$$\imath\hbar\frac{\partial}{\partial t}\psi_0(\mathbf{r},t) = \left(-\frac{\hbar^2\nabla^2}{2m} + V_{ext}(\mathbf{r}) + g\,|\psi_0(\mathbf{r},t)|^2\right)\psi_0(\mathbf{r},t) \tag{1.14}$$

where $\psi_0(r)$ is real and normalized to the total number of atoms and the interaction potential. This equation has the form of a nonlinear Schrödinger equation where the nonlinear contribution comes from the term $g|\psi_0(\mathbf{r},t)|^2$ that is proportional to the particle density.

1.2.1 Thomas-Fermi approximation

The criterion for discriminating between the weak and strong interaction regimes consists in comparing the kinetic energy with the mean field energy. The latter can be estimated using the ground state function of the harmonic oscillator in the absence of interactions, obtaining:

$$E_{int} \propto N_0^2 \frac{|a_s|}{a_{ho}^3}\,, \tag{1.15}$$

where N_0 is the number of condensed atoms and $a_{ho} = \sqrt{\hbar/m\omega_{ho}}$ is the harmonic oscillator width. The kinetic energy is:

$$E_{kin} \approx N_0\hbar\omega_{ho} \propto \frac{N_0}{a_{ho}^2}\,. \tag{1.16}$$

Hence we obtain:

$$\frac{E_{int}}{E_{kin}} \propto N_0 \frac{|a_s|}{a_{ho}} \,. \tag{1.17}$$

In the limit $N_0|a_s|/a_{ho} \gg 1$ we can neglect the kinetic energy term (Thomas-Fermi approximation), obtaining the following equation for the ground state of the system:

$$\left(V_{ext}(\mathbf{r}) + g\psi_0^2(\mathbf{r})\right)\psi_0(\mathbf{r}) = \mu\psi_0(\mathbf{r}), \tag{1.18}$$

whose solution is:

$$n(\mathbf{r}) = |\psi_0|^2 = \frac{1}{g}\max[\mu - V_{ext}(\mathbf{r}), 0]. \tag{1.19}$$

For harmonic confinement we find:

$$n(\mathbf{r}) = \frac{\mu}{g}\left[1 - \left(\frac{x}{R_x}\right)^2 - \left(\frac{y}{R_y}\right)^2 - \left(\frac{z}{R_z}\right)^2\right], \tag{1.20}$$

where the Thomas-Fermi radii are:

$$R_i = \sqrt{\frac{2\mu}{m\omega_i^2}} \,. \tag{1.21}$$

These represent the size of the cloud inside the confining trap. From the normalization condition $N_0 = \int n(\mathbf{r})d\mathbf{r}$ the chemical potential is easily calculated as:

$$\mu = \frac{\hbar\omega_{ho}}{2}\left(\frac{15N_0a_s}{a_{ho}}\right)^{2/5} \,. \tag{1.22}$$

1.3 Laser cooling

The fundamental scientific progress that led to the achievement of the Bose-Einstein condensation is laser cooling ([9, 14, 72]), which I will briefly review in the following.

1.3.1 Doppler Cooling

Historically the first paradigm of laser cooling was Doppler cooling, which is based on a simple mechanism. A two-level atom absorbing a photon gets a momentum kick in the direction the photon was propagating in. The excited atom spontaneously emits a photon in a random direction, giving the atom a recoil in the opposite direction of the emitted photon. By considering the

absorption of several photons and the their following emissions, the averaged effect will be a momentum kick per cycle in the direction of the incoming photon. The force can be evaluated in a rigorous treatment by considering the radiation pressure of the light and by solving the optical Bloch equations [65]. For a small detuning ($\Delta \ll \omega_0$) a process of absorption and spontaneous random emission on one atom changes its momentum by:

$$\delta\mathbf{p} = \hbar\mathbf{k}(1 - \cos(\theta)) \tag{1.23}$$

where $\mathbf{k} = k\hat{\mathbf{z}}$ is the laser wavevector and θ is random. Therefore, after averaging over θ, the force exerted on the atom is:

$$\mathbf{F} = \hbar k \frac{\Gamma\Omega_R^2/4}{\Delta^2 + \Gamma^2/4 + \Omega_R^2/2}\hat{z} \tag{1.24}$$

where Γ is the natural linewidth of the excited atomic state, $\Omega_R = \wp E_0/\hbar$ the Rabi frequency of the atomic transition, $\wp$ the electric dipole moment of the atom and E_0 the amplitude of the light electric field. The detuning Δ of equation 1.24 has to be corrected by taking into consideration the Doppler effect present if the atom is moving with respect to the beam. An atom moving towards a red detuned laser beam will have its transition shifted closer to resonance by the Doppler effect. By substituting Δ with $\Delta - k_L v$ one finds the equation:

$$\langle \overrightarrow{F}_+ \rangle = \langle \overrightarrow{F}_0 \rangle - \gamma_d v\hat{\mathbf{z}}. \tag{1.25}$$

The average force will thus have one part that is the same as for the atom at rest, and the other one where the force is proportional to the atomic velocity $v = |\mathbf{v}|$. Using red detuned beams, the velocity sensitive force will act as a damping on the system, where the damping coefficient can be written as:

$$\gamma_d = -\hbar k_L^2 \Gamma\Delta \frac{\Omega_r^2}{(\Gamma^2/4 + \Delta^2)^2}. \tag{1.26}$$

An atom moving towards the beam will thus feel a retardation force. By using two counter-propagating beams, the force applied to an atom is

$$\langle \overrightarrow{F} \rangle = \langle \overrightarrow{F}_+ \rangle - \langle \overrightarrow{F}_- \rangle = -2\gamma_d v\hat{\mathbf{z}}. \tag{1.27}$$

The laser field works as a viscous medium for the atom. Such a system is known as an *optical molasses* ([11]). It can be evaluated ([85]) that the lowest temperature achievable in an optical molasses is:

$$k_B T_D = \frac{1}{2}\hbar\Gamma, \tag{1.28}$$

usually referred to as the *Doppler temperature*.

1.3.2 Magneto-Optical Trapping

The cooling in optical molasses is based on the dependence of the detuning seen by the atoms on their velocity but the atoms inside a three dimensional molasses are not spatially confined. In order to trap the atoms, a good strategy is to make this detuning dependent on the spatial position of the atoms. This can be realized by use of a magnetic gradient b'. In a one dimensional system this corresponds to having a magnetic field varying in space: $\mathbf{B} = b'z\hat{\mathbf{x}}$. Thus the Zeeman energy shift depends on the position of the atom:

$$\Delta E_Z = \mu_B g_F m_F b' z \tag{1.29}$$

where μ_B is the Bohr magneton, g_F is the Landé factor and m_F is the x component of the angular momentum. By shining circularly polarized light on the atoms, the energy shift (1.29) changes the detuning seen by the atoms.

$$\Delta \mp \gamma_d v_z \pm \mu_B g_F m_F b' z/\hbar. \tag{1.30}$$

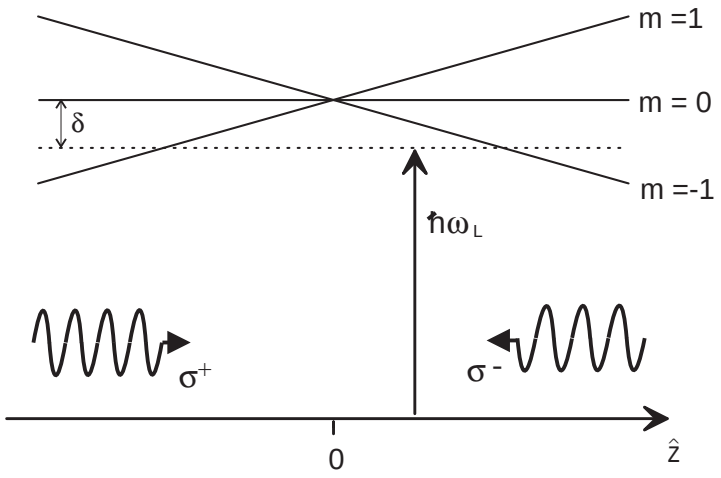

Figure 1.3: Principle of a one dimensional MOT for a $F = 0 \rightarrow F' = 1$ transition. The inhomogeneous magnetic field induces a space-dependent shift of the Zeeman sublevels, producing a space-dependent force on the atoms.

Actually the internal selections rules between Zeeman sublevels realize a force which depends on the distance from the center of the trap $\mathbf{r}$ and on the speed of the atoms:

$$\overrightarrow{F} = (-\gamma_d v + m\omega^2)\hat{\mathbf{z}} \tag{1.31}$$

where for $b' < 0$:

$$\omega^2 = \frac{\mu_B g_F m_F |b'|}{m\hbar k}\gamma_d. \tag{1.32}$$

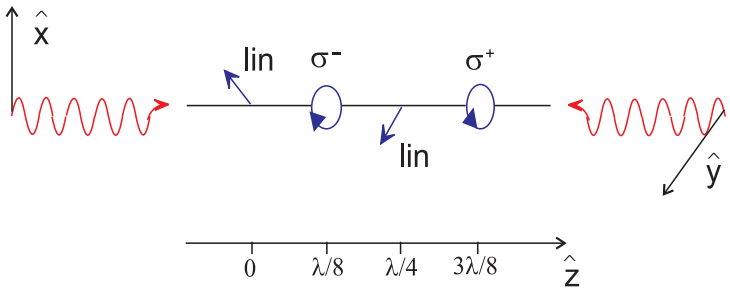

Figure 1.4: Polarization scheme for the 1D *lin* ⊥ *lin* configuration.

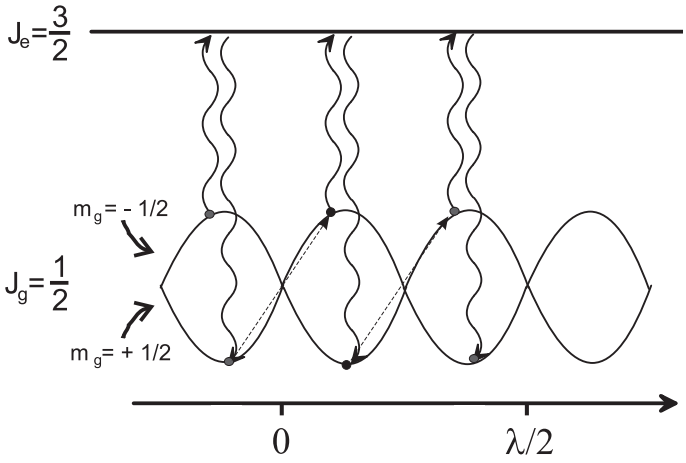

Figure 1.5: Light shifts as a function of the spatial position.

This trap is known a Magneto-Optical Trap (MOT)[75] and it represents the initilal stage for the cooling process.

1.3.3 Sub-Doppler Cooling

In the early years of laser-cooling atomic samples in optical molasses were observed which exhibited temperature well below the Doppler limit [59]. Hence the simple picture presented in the previous section does not provide a complete description of the cooling mechanism. A complete analysis has to take into account the internal structure of the atoms, and the presence of polarization gradients can explain the sub-Doppler temperatures observed ([19]).

An example of sub-Doppler cooling is the so called *Sisyphus cooling* [20]. In the overlapping region of two counterpropagating laser beams with orthogonal linear polarizations, the local polarization varies periodically according to the scheme of figure (1.4). Let us consider an atom with total angular momentum $J_g = 1/2$ for the ground state and $J_e = 3/2$ for the excited state. The two Zeeman sublevels $m_g = -1/2$ and $m_g = 1/2$ experience a light shift which varies as a function of the spatial position as sketched in figure (1.5).

It is possible to demonstrate that when the energy of one sublevel is at

the maximum there is a high probability of jumping to the other sublevel after a cycle of absorption—spontaneous-emission. For example, an atom initially in the $m_g = -1/2$ sublevel during its motion climbs the potential hill, losing kinetic energy. When the atom reaches the top of the hill, it leaves the sublevel and repeats the entire process. After each cycle the atom loses some of its energy, which leads to a cooling of the sample.

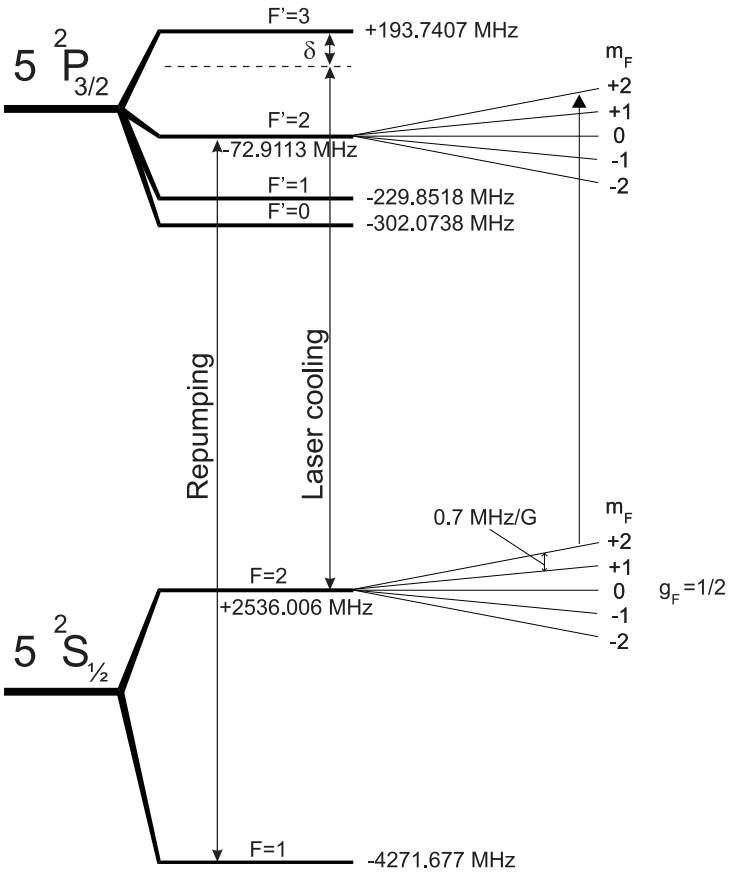

Figure 1.6: Scheme of the D2 line of ^{87}Rb.

1.3.4 Laser Cooling of Rubidium

The element we chose for our experiment is Rubidium-87, which is one of the alkali atoms of the periodic table. The cooling of this element is easy as the presence of only a single valence electron makes it a good approximation of a two level system. The energy transitions that can be used for the laser cooling of Rb atoms are from the state $5^2S_{1/2}$ to the $5^2P_{1/2}$ and to the $5^2P_{3/2}$

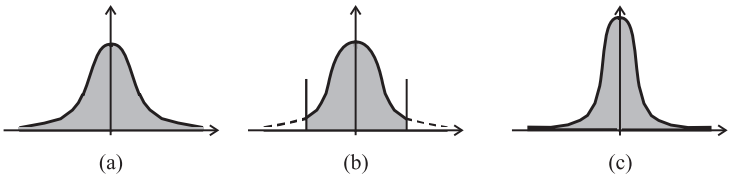

Figure 1.7: The evaporative cooling process: the tails of the thermal velocity distribution of the atoms are cut by expelling the atoms with higher energy. The system then re-thermalizes and the final temperature is lowered.

levels, usually called the D1 and D2 lines, centered at 795 nm and 780 nm respectively.

The optical transition we used was the D2 line, whose spectrum is shown in figure (1.6), where the hyperfine levels of the $5^2S_{1/2}$ and $5^2P_{3/2}$ states are called F and F' respectively. The ground state hyperfine level used in our experiment was $|F = 2\rangle$. The frequency of the light used for the optical molasses and the MOT was chosen to be near resonant to the transition $|F = 2\rangle \rightarrow |F' = 3\rangle$, the so-called *laser cooling* transition, and hence only the atoms in the $|F = 2\rangle$ level were trapped in the MOT. However, this laser cooling transition is not closed: the atoms can be off-resonantly excited to the $|F' = 2\rangle$ level, then decaying to $|F = 1\rangle$. This effect would cause a depletion of the number of atoms in the MOT. In order to avoid this loss, a light near resonant to the $|F = 1\rangle \rightarrow |F' = 2\rangle$ transition was added to the laser cooling light, hence re-pumping the atoms from the $|F = 1\rangle$ level to $|F = 2\rangle$. This light is called *re-pumper*.

1.4 Evaporative cooling

The highest phase space density ρ that can be achieved with laser cooling is around 10^{-6} and is not enough for reaching the Bose-Einstein condensation. The simple idea used for increasing ρ is *evaporative cooling*. In fact it is always possible to obtain a colder ensemble of atoms by selecting and removing the most energetic particles from the system. If the process is achieved in such a way that the cloud has enough time and density for the thermalization of the remaining atoms, this technique leads to a very high cooling efficiency and finally to the condensation.

The evaporation is applied by decrasing the depth of the confining potential, letting the hottest atoms leave the trap. In our apparatus we implemented a double evaporative cooling stage, first in a magnetic trap and then in an all-optical trap.

1.4.1 The magnetic trap

After the laser cooling stage, the atoms are loaded first into a magnetic field where the first stage of evaporation can be realized. This magnetic field consists of two components, the quadrupole and the bias field.

The quadrupole trap. As the potential seen by a particle of magnetic moment $\boldsymbol{\mu}_m$ in a magnetic field $\mathbf{B}$ is:

$$U = -\boldsymbol{\mu}_m \cdot \mathbf{B}, \tag{1.33}$$

which corresponds to an energy of $E = \mu_B g_F m_F B$. one of the simplest configurations which can provide confinement for a neutral particle is a quadrupolar magnetic field:

$$\mathbf{B_Q} = b'(-\hat{\mathbf{x}} - \hat{\mathbf{y}} + 2\hat{\mathbf{z}}). \tag{1.34}$$

The atoms are confined in a local minimum of the energy E. For $g_F m_F > 0$ (weak field seeking states) this requires a local magnetic field minimum. Strong field seeking states ($g_F m_F < 0$) cannot be trapped by static magnetic fields, because Maxwells equations do not allow a magnetic field maximum in free space. In its frame of reference an atom moving in the trap sees a magnetic field whose modulus and orientation change continuously. To avoid transitions to untrapped Zeeman states - *Majorana spin flips* - the condition $\frac{d\theta}{dt} < \boldsymbol{\mu}_m \cdot \mathbf{B}/\hbar = \omega_{Larmor}$, has to be satisfied ($\theta$ is the orientation of $\mathbf{B}$ and ω_{Larmor} is the Larmor frequency which is the frequency of rotation of the atomic magnetic moment around the direction of the magnetic field).

In the regions of zero magnetic field $\omega_{Larmor} = 0$ and the above condition cannot be satisfied. Moreover for a quadrupole trap the zero of the magnetic field corresponds to the minimum of the energy and the atomic cloud will be densest in that region. For this reason it is not possible to increase the phase-space density in such a trap without having large particle losses.

The TOP trap. Several techniques have been developed to solve the problem of the Majorana spin flips at the center of the magnetic trap. The one used in our lab is to add a bias field that moves the zero of the magnetic trap away from the center of the trap around the cloud (figure 1.8). The bias field is

$$\mathbf{B}_{\mathrm{TOP}} = B_0 \left[\hat{\mathbf{x}} sin(2\pi\Omega_{\mathrm{TOP}}) + \hat{\mathbf{z}} \cos(2\pi\Omega_{\mathrm{TOP}})\right] \tag{1.35}$$

where the rotation frequency Ω_{TOP} is chosen to be smaller than ω_{Larmor} in order to mantain the atomic magnetic moment alined with the total field. If

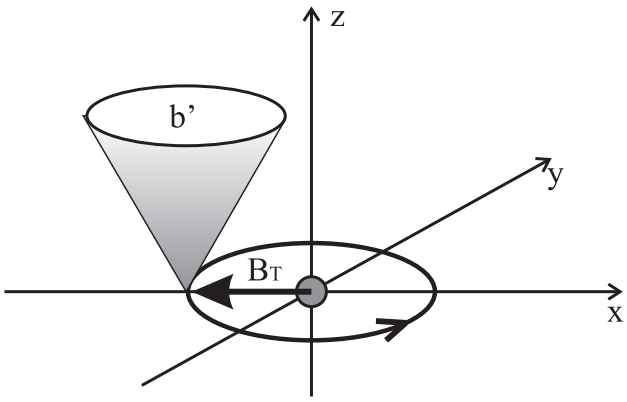

Figure 1.8: The TOP trap. A rotating magnetic bias field causes a continuous displacement of the $B = 0$ point in order to avoid spin flip losses at the center.

the atomic motion is are much slower than the movement of the zero magnetic field point, the time-dependent potential $U(x, y, z, t) = \mu|\mathbf{B_Q}(x, y, z) + \mathbf{B_{TOP}}(x, y, z, t)|$ can be averaged on a rotation period.

$$U(x, y, z) = \int_{t=2\pi/\Omega_{TOP}} U(x, y, z, t)dt \tag{1.36}$$

The shape of the integrated potential is, close to its minimum, parabolic, with its minimum $B_{min} \neq 0$, and with average frequency:

$$\omega_{ho} = (\omega_x\omega_y\omega_z)^{1/3} = \frac{b'}{\sqrt{B_{TOP}}}\sqrt{\frac{\mu}{m}}. \tag{1.37}$$

The orbiting motion of the local zero around the cloud can be used for the evaporation of the energetic atoms at the edges. For this reason this path is called the *circle of death*. As this radius is equal to $r_{cod} \propto (B_{TOP}/b')$, the parameter B_{TOP} and b' can be changed separately in order to set the desired trapping frequency and *circle of death* dimension.

1.4.2 The dipolar trap

The second evaporation stage is implemented in an all optical trap. which relies on the electric dipole interaction with a far-detuned beam. In that way it is possible to create nearly conservative potential wells where the influence from the spontaneous photon emissions is weaker than the dipole interaction ([10], [40]). In the presence of an oscillating electric field $\mathbf{E}$, the atom acquires an electric dipole moment $\mathbf{P}$ oscillating in time at the same frequency ω as the laser light. In complex notation

$$\begin{aligned} \mathbf{E}(\mathbf{r}, t) &= \hat{\mathbf{e}}\, E(\mathbf{r})e^{-i\omega t} + c.c. \\ \mathbf{P}(\mathbf{r}, t) &= \hat{\mathbf{e}}\, P(\mathbf{r})e^{-i\omega t} + c.c. \end{aligned} \tag{1.38}$$

where $\hat{\mathbf{e}}$ is the polarization vector. The two amplitudes E and P are related by the simple relation $P = \alpha E$ and α is the complex polarizability which contains information on the absorption rate ($\mathrm{Im}(\alpha)$) and confinement potential ($\mathrm{Re}(\alpha)$). The interaction potential is

$$U_{\mathrm{dip}} = -\frac{1}{2}\langle \mathbf{P} \cdot \mathbf{E} \rangle = -\frac{1}{2\epsilon_0 c}\mathrm{Re}(\alpha) I \tag{1.39}$$

where $\langle \cdot \rangle$ denotes a temporal average over the terms oscillating in ω, and I is the field intensity. From equation 1.39 one finds that the potential is proportional to the intensity of the laser light and to the real part of the polarizability. The resulting dipolar force is

$$\mathbf{F}_{\mathrm{dip}}(\mathbf{r}) = -\nabla U_{\mathrm{dip}}(\mathbf{r}) = \frac{1}{2\epsilon_0 c}\mathrm{Re}(\alpha)\nabla I(\mathbf{r}). \tag{1.40}$$

A straightforward evaluation of the polarizability can be obtained from the election equation of motion $\ddot{x} + \Gamma_\omega \dot{x} + \omega_0^2 x = -eE(t)/m$ ($\hbar\omega_0$ is the energy difference in the two levels system)

$$\alpha = \frac{e^2}{m_e}\frac{1}{\omega_0^2 - \omega^2 - i\omega\Gamma_\omega}. \tag{1.41}$$

where the classical damping rate $\Gamma_\omega = e^2\omega^2/(6\pi\epsilon m_e c^3)$ can be substituted by taking into consideration matrix elements between the ground state and the excited level[1]

$$\Gamma = \frac{\omega^2\omega_0}{3\pi\epsilon_0\hbar c^3}|\wp|^2. \tag{1.42}$$

Γ represents the line with of the optical transition at frequency ω_0. With the above expression, the dipolar potential in the relevant case of large detuning Δ ($\equiv \omega - \omega_0 \ll \omega_0$) is

$$U_{\mathrm{dip}} = -\frac{3\pi}{2\omega_0^3}\frac{\Gamma}{\Delta} I(\mathbf{r}), \tag{1.43}$$

where the sign of the detuning becomes determining for the determination of a minimum or a maximum of the potential.

In our experiment we use focused crossed gaussian beams with red detuning ($\Delta < 0$). Atoms are attracted to the regions of highest intensity, and the potential due to a single beam has a cylindrical symmetry

$$U_{\mathrm{dip}} = U_0\left[1 - e^{-2\left(\frac{r}{w_0}\right)^2} e^{-\left(\frac{l}{z_R}\right)^2}\right], \tag{1.44}$$

[1]This result can be generalized to a multi level system by taking into consideration the effect of the light on the level structure.

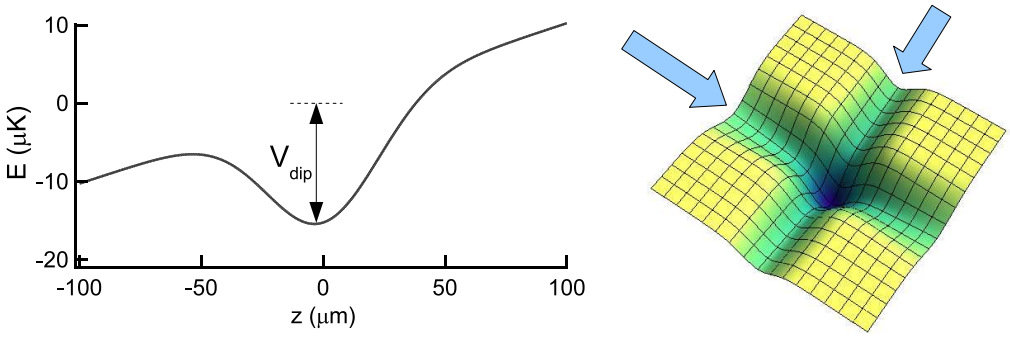

Figure 1.9: **left** Dipolar confinement along the gravity (z) direction created by a horizontal laser beam with $\lambda = 1030\,\mathrm{nm}$, $w_0 = 46\,\mu\mathrm{m}$ and of power $P = 1.1\,\mathrm{W}$. V_{dip} is the resulting trap depth. **right** Dipolar confinement on the XY plane created by two crossed laser beams.

where U_0 contains the laser detuning and the atomic frequencies, w_0 is the waist of the beam and z_R is the Rayleigh range $\pi w_0^2/\lambda$. A harmonic approximation can be applied, and the frequencies are $\omega_r = \sqrt{(4U_0/mw_0^2)}$ in the radial direction and $\omega_l = \sqrt{(2U_0/mz_R^2)} = \sqrt{(2U_0\lambda^2/(m\pi^2 w_0^4))} = \omega_r\sqrt{\lambda^2/(\pi^2 w_0^2)}$ in the axial direction. As the quantity $\sqrt{\lambda^2/(\pi^2 z_R^2)}$ for our parameters is always is very small, the axial confinement is negligible compared to the radial one and is too weak for holding the atoms. For this reason, in our setup two crossed beams are used (on the right of figure 1.4.2). As they have identical waists and are both on the horizontal plane of the experiment, in the vertical direction the atoms feel the confinement of both the laser beams and the vertical trap frequency ω_z is $\sqrt{2}\omega_r$ and $\omega_x = \omega_y = \omega_r$. The evaporative cooling in the dipolar trap is performed by ramping down in time the power of both the dipolar beams, so both the depth and the trap frequencies of the optical trap were reduced. The atoms with higher energy escape from the trap and gravity has in important role in moving the hot untrapped atoms far from the center of the potential (see left of Figure 1.9).

1.5 The Pisa Apparatus

Our new Bose-Einstein condensate apparatus, as shown schematically in Figure 1.10, is based on a two-cell system. Two cells are horizontally mounted on a central metallic structure that contains pumps and pressure sensors. The two parts of the vacuum system are connected by a narrow graphite tube

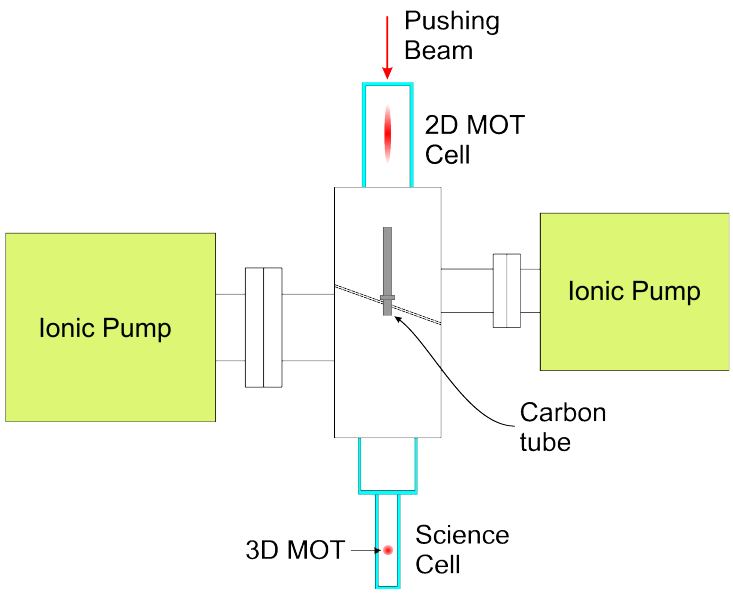

Figure 1.10: Scheme of the vacuum chamber. The magnetic field coils and the 2D and 3D MOT laser beams are not shown.

and support a pressure gradient, the pressure in the first cell being of the order of 10^{-9} mbar and that of the second cell around 10^{-11} mbar. The Rb atoms were provided by two pairs of dispensers: electric resistances whose surface was covered with Rb, which was emitted when an electric current flowed in them. The atoms are cooled and captured in a cigar shaped cloud in a two-dimensional MOT (Magneto-Optical Trap) and cooled by two back reflected beams. This 2D MOT system is very compact and characterized by large beam waists (12 mm) and short optical paths. These features led to high stability and a large and constant number of atoms captured, resulting in a continuous high flux from the first to the second cell. The 2D MOT is operated at 2.4Γ red detuning from the transition $|F = 2\rangle \rightarrow |F' = 3\rangle$ and a laser intensity of 22 I_{sat} (for Rubidium-87, the natural linewidth Γ of the $|F' = 3\rangle$ level is 6.065 MHz and $I_{sat} = 1.6\,\mathrm{mW/cm^2}$). The 2D MOT magnetic gradient was $b' = 11\,\mathrm{G/cm}$.

Atoms captured in the first cell are pushed into the second cell by a laser beam focused on the center of the cloud in the first cell. The 3D MOT in the second cell was created by splitting a $\sim 33\,\mathrm{mW}$ beam into six beams of waist $w_0 = 8\,\mathrm{mm}$ and the beams were directed to the cell as three mutually orthogonal counterpropagating pairs. A repumper laser was added to two of these three pairs. The 3D MOT beams were detuned by $\Delta = -2.5\,\Gamma$ from

the $|F = 2\rangle \rightarrow |F' = 3\rangle$ transition and the magnetic gradient for the MOT was $b' = 6.6\,\mathrm{G/cm}$. The flux of atoms from the 2D MOT led to a continuous loading of the 3D MOT. This loading process was counteracted by an atom loss process that was mainly due to collisions with background atoms. After $\sim 90\,\mathrm{s}$ of loading the MOT reached a stationary size, and up to $2 \cdot 10^9$ atoms were trapped. A portion of the light scattered by the atoms was collected by a lens and sent to an amplified photodiode, whose signal was proportional to the number of atoms in the MOT. This reference was used as starting trigger for the experiments in order to have initial clouds of roughly the same size for every experimental cycle. Loading times of $25 - 40\,\mathrm{s}$ were usually sufficient in order to trap enough atoms before starting sub-Doppler and evaporative cooling.

1.5.1 The magnetic field system

As explained in the previous section, the cooling and trapping of atoms requires different magnetic fields whose generation requires big power supplies and special switches for large currents. In this section we summarize the technical features of our system.

- **The quadrupole field**. This was created by six cylindrical pancake-shaped coils placed along the direction of gravity z, that was hence the strong axis with the largest field gradient. In order to create a spatial magnetic gradient, the three coils above the science cell were in anti-Helmholtz configuration with respect to the three coils below the science cell (see Fig.(1.11)). The coils were made of copper and were covered with an insulating sock. The wires used for the coils were hollow, and are continuously cooled by water flow. The resulting magnetic gradient had cylindrical symmetry so that its modulus in the z direction (the strong axis) was $2b'$, while in the x, y directions it was b'. Magnetic gradients up to $b' = 366\,\mathrm{G/cm}$ were created when the current was 226 A . This value was reached in 4 ms, while the time for switching off the field was of the order of μs.

- **The rotating bias field**. This field B_{TOP} was created by two pairs of coils: a pair of circular coils that were placed between the quadrupole coils, and a pair of square coils in the orthogonal direction (see Fig.(1.11)), both in Helmholtz configuration. The current flowing in each pair oscillated in time, and the pairs were mutually dephased by $\pi/2$: $I_{circular} = I_{TOP}\sin(\omega t)$, $I_{squared} = I_{TOP}\sin(\omega t + \pi/2)$, with $\omega/2\pi = 10\,\mathrm{KHz}$. The

maximum value of the field was $B_{TOP} = 38\,\mathrm{G}$. The cooling of the coils was ensured by their contact with the water-cooled quadrupole coils.

- **The compensation field**. These were three muthually orthogonal pairs of coils in the Helmholtz configuration. The current flowing in these coils was of the order of 100 mA. The magnetic field created by these coils was used to compensate the external fields, such as the earth's magnetic field and the magnetic field created by the ion pumps.
- **The displacement field**. A single coil placed above and parallel to the quadrupole coils creates a magnetic field that was varied during the experiment in order to be able to vertically move the position of the cloud along the z-axis and hence to minimize the losses when the trap was changed, e.g., when passing from the TOP to the dipolar trap.

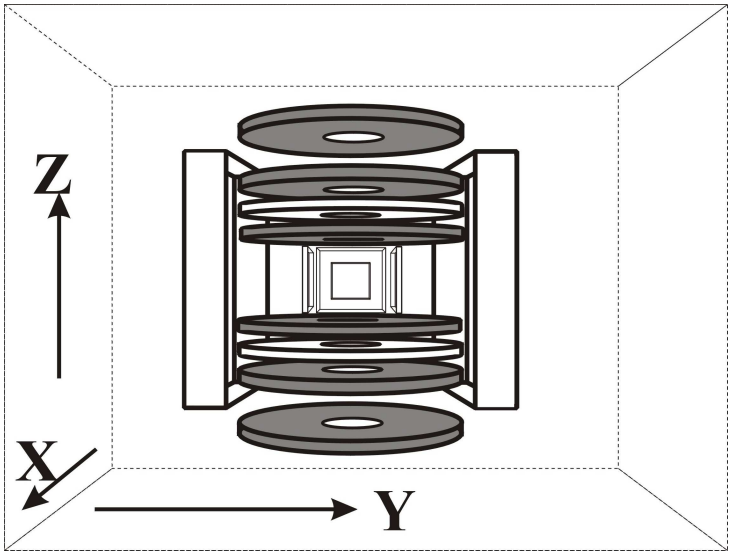

Figure 1.11: *Magnetic system.* Schematic diagram of the pancake coils for quadrupolar (shaded) and TOP fields (white). The external cage contains the compensation coils. The displacement coil is not drawn.

1.5.2 Laser system

The realization of a Bose-Enstein Condensate and its use for experiments imply the use of several laser sources for cooling, manipulating and detecting the ultra cold cloud. The lasers used for our realization can be divided in two groups:

- **Cooling and Imaging** The laser system for the cooling transition is a chain composed of a master laser (50 mW diode laser with Doppler free spectroscopy stabilization), a slave laser (100 mW laser diode with frequency control) and a tapered amplifier (up to 1 W). All the lasers are temperature stabilized with 0.01 K precision. The light from the tapered amplifier is split in two beams, sent through two AOMs (acousto-optical modulators) and injected into two single-mode, polarization maintaining optical fibers, one for each MOT. The AOMs placed before the fibers allow us to control the frequency and the power of the light that reaches the atoms in the cell during different steps of the laser cooling scheme. Another laser system in the configuration master-slave is used to produce repumping light, which is also injected into an optical fiber. The laser light needed for optical pumping and imaging purposes is obtained from the zero-th order of the AOMs providing the cooling light and injected together into a single optical fiber. In the present configuration the laser power available at the outputs of the fibers was 160 mW for the 2D MOT, 33 mW for the 3D MOT, and 9 mW and 3 mW for imaging and optical pumping, respectively.

- **Dipole Trap** The laser used for the dipole trap is a ELS Versadisk Yb:YAG which emits up to 5.4 W of cw power at 1030 nm. The beam is split in two separated beams which are sent to two different acousto-optic modulators driven at the same frequency but with two different diffraction orders to avoid interference effects between the two beams). The beam are focused down to a waist of 75 μm and we collect the light passing trough the cell with two photodiodes. As our experiments requires a high stability of the laser during long times (tens of seconds) as well as very short times (milliseconds, to avoid excitation of the atoms), these signals are compared to a computer reference, and two homemade PID controllers correct intensity fluctuations through electronic feedback on the two AOMs. The analog signal from the computer to the PID is also used for creating ramps or periodical variation of the laser power up to 6 kHz. Fourier analysis of the monitored power showed that the laser is well stabilized for all frequencies below 6-7 kHz, a range wide enough to allow dipole trap loading and evaporation. In this range, the noise of a stabilized constant power is of the order of $10^{-4} - 10^{-5}$ of the cw signal, comparable with the noise level of the computer reference signal. The maximum trap frequency is $\sim$250 Hz corresponding to a depth of 5 μK.

1.6 The experimental procedure

The Bose Einstein condensate is the principal tool of our investigation and its creation is itself a hard task. In order to obtain it, after loading $\sim 10^9$ atoms into the 3D MOT a sequence of optical and evaporation cooling takes place. The temporal sequence is controlled by a computer with a precision of 10 μs and composed of different phases during which experimental parameters such optical frequencies and magnetic fields are changed. After every cycle the parameters are reset to the 3D MOT default ones. The BEC sequence is composed of the following steps:

1. **Compressed-MOT**: the magnetic gradient is decreased from 7.3 G/cm to 2.6 G/cm in 200 ms while the detuning of lasers is increased from -2.5 to -4.8 Γ. In this phase the cloud is reduced in volume for optimizing the loading into the TOP trap.

2. **Molasses**: the magnetic gradient is switched off and the lasers are further detuned to -5.0Γ. In this phase (6 ms) sub-Doppler cooling takes place, after which the atoms reach a temperature of $\sim$15 μK. During the molasses the capacitors of the quadrupole field power supplies are charged in order to in order to be able to switch on the TOP trap in a very short time.

3. **Optical Pumping**: this phase consists of pumping the atoms into the $|F = 2, m_F = 2\rangle$ state. The selection rule $\Delta m_F = +1$ is realized with circularly polarized $\sigma^{(+)}$ light and the rotating magnetic field is pointing in the same direction as the light wavevector.

4. **Circle of Death evaporation**: at the end of the optical pumping stage the atoms are loaded into the TOP trap. This is done by increasing the magnetic gradient in 1 ms to $b' = 73\,\mathrm{G/cm}$, while the rotating bias field is turned on at its maximum value (38 G), in order to maximize the circle of death. After the loading, the trap frequencies are first increased to 400 Hz in order to enhance the collision rate for an efficient evaporative cooling. The evaporative cooling is then realized by reducing the circle of death. At the end of the process the cloud containes $\sim 6 \cdot 10^5$ atoms at a temperature $T = 2.5\,\mu$K. and the phase space density is $\sim$0.1

5. **Dipolar trap**: the loading from the TOP trap to the two beams forming the dipolar trap is optimized in order to have an efficient mode matching between the frequencies and to have enough trap depth in

order not to lose atoms. After loading the atoms, the evaporation in the dipolar trap is done in 3 s by decreasing the power with three linear ramps down to the value at which condensation takes place. The better evaporation efficiency of a dipole trap compared to the TOP one is related to the more homogenous evaporation that takes place in all the three dimensions instead of circle of death (along a plane circle). Our typical condensates are realized in a trap with frequencies ω_x, ω_y and ω_z equal to 68, 68 and 96 Hz, respectively

6. **Experiments**: holding the condensate in the dipolar trap with the final frequencies or in other configurations, the different experiments are performed by switching on an optical lattice lattice or modulating the power of the dipolar trap beams.

7. **Imaging**: at the end of the experiments the atoms are released from the trap and allowed to expand in free space, in order to decrease the density of the cloud and increase its size. After a certain time (called *time of flight*) of $\sim 10 - 20\,\text{ms}$ a resonant light pulse of $20\,\mu\text{s}$ duration illuminates the atoms and then is collected by a CCD camera, in which the shadow of the atomic cloud is imaged. The CCD camera is from DTA, featuring a Kodak Chip (KAF 1400) with pixel size $6.8 \times 6.8\,\mu\text{m}$, whose quantum efficiency is 40% at 780 nm. In front of the CCD camera an objective (Rodenstock Aporodagon) of focal length $f = 75\,\text{mm}$ and f-number $f/\# = 4.5$ is placed. The objective is optimized for 1:2 reduction, but it is used reversed in order to have a magnification of ~ 2. The system is focused by minimizing the apparent size of small atomic clouds imaged on the CCD and the calibration of the image size is done by performing an experiment of free fall of the condensate under gravity, see Fig. 1.4.2.

The distinctive threshold for the formation of the condensate is well recognizable by looking at the profile of the absorption pictures. Just below the critical temperature T_C a clear bimodal distribution is visible where the narrower peak contains the condensate while the wider one is the thermal part of the cloud.

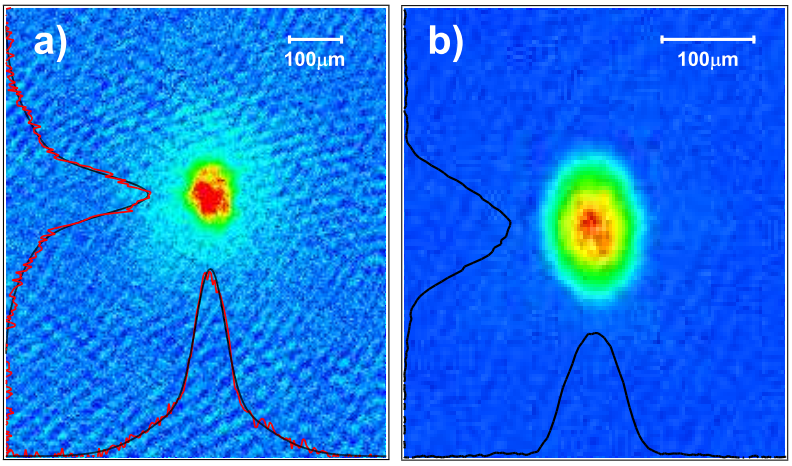

Figure 1.12: Image of a cloud (**a**) just below the threshold for condensation (the bimodal distribution is evident) and (**b**) a almost pure condensate.

Chapter 2

BEC in optical lattices

This Chapter introduces the fundamental tool of our investigations on the properties of a Bose-Einstein condensate: the optical lattice. Periodic potentials have been studied for long time in different areas of condensed matter physics and here I review the two most useful theoretical approaches in order to facilitate the understanding of the future chapters. I will show how a periodic potential can be experimentally created and calibrated and how BECs can be adiabatically loaded into it.

2.1 The standing wave

A standing wave can be obtained by two counter-propagating linearly polarized traveling waves with the same frequency ω_L. The generated electric field $\mathbf{E}$ is

$$\begin{aligned}\mathbf{E}(\mathbf{r},t) &= E_0 \sin(k_L x + \omega_L t)\hat{\mathbf{e}} + E_0 \sin(k_L x - \omega_L t)\hat{\mathbf{e}} \\ &= 2E_0 \sin(\omega_L t)\sin(k_L x)\hat{\mathbf{e}}\end{aligned} \tag{2.1}$$

where E_0 is the amplitude and k_L is the wavevector. When the detuning from the atomic transition is large enough, it is possible to neglect the spontaneous emission and an atom placed in the standing wave feels a periodically varying dipole force (see the paragaph 1.4.2 about the dipolar trap). The resulting potential calculated as for the dipolar trap in Sec. 1.4.2 and depending on the square of $\mathbf{E}$, will be written as

$$V(x) = \frac{V_0}{2}\cos(2k_L x). \tag{2.2}$$

where V_0 is the depth of the optical Lattice

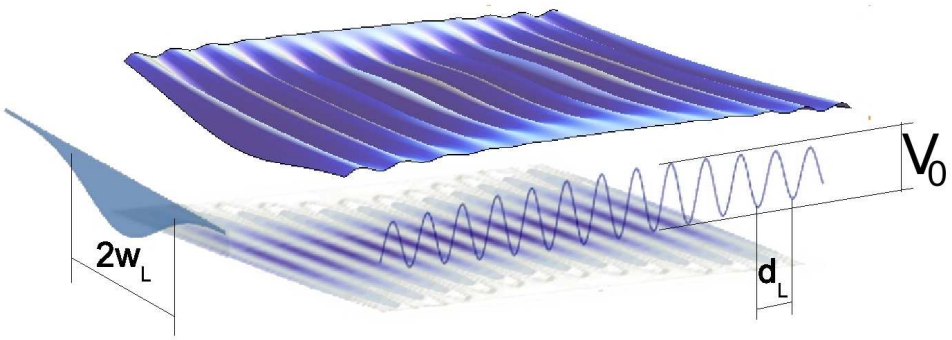

Figure 2.1: The periodic potential created by two counter-propagating laser beam. $d_L = \lambda/2$ is the lattice constant and V_0 the depth. The finite size of the laser beam induces a gaussian profile in the direction perpendicular to the lattice and a consequent dipolar confinement. The lattice constant d_L (0.421μm) and the laser waist w_L (100μm) are not on the same scale.

This periodic potential has a lattice spacing of $d_L = \pi/k_L$ and for a laser beam with detuning Δ and intensity I, the amplitude V_0 is

$$V_0 = \zeta\hbar\frac{I}{I_s}\frac{\Gamma_s^2}{\Delta} \tag{2.3}$$

where I_s is saturation intensity and ζ is a correction which depends on the level structure of the atom [40]. In a quantum mechanical approach these results derive from the different the interaction between an atom and the photons of the lattice beams creating the lattice. For this reason the usual quantities related to the lattice are defined starting from the recoil momentum $p_{\rm rec} = \hbar k_L$ acquired by an atom after the absorption or the emission of a photon. V_0 is expressed in units of $E_{\rm rec}$ that is the recoil energy exchanged by an atom and a photon

$$E_{\rm rec} = \frac{\hbar^2 {k_L}^2}{2m} \tag{2.4}$$

and other important units used are $mv_{\rm rec} = p_{\rm rec}$, and $\nu_{\rm rec} = E_{\rm rec}/h$.

2.2 Atoms in a periodic potential

The phenomena related to a periodic potential have been extensively studied in the physics of electrons in crystals. Many experimental realizations shown in this thesis were invented and analyzed in the early age of solid state physics

but their realizations were made difficult by the imperfections of the crystal and by the strong interactions present in an crystal lattice.

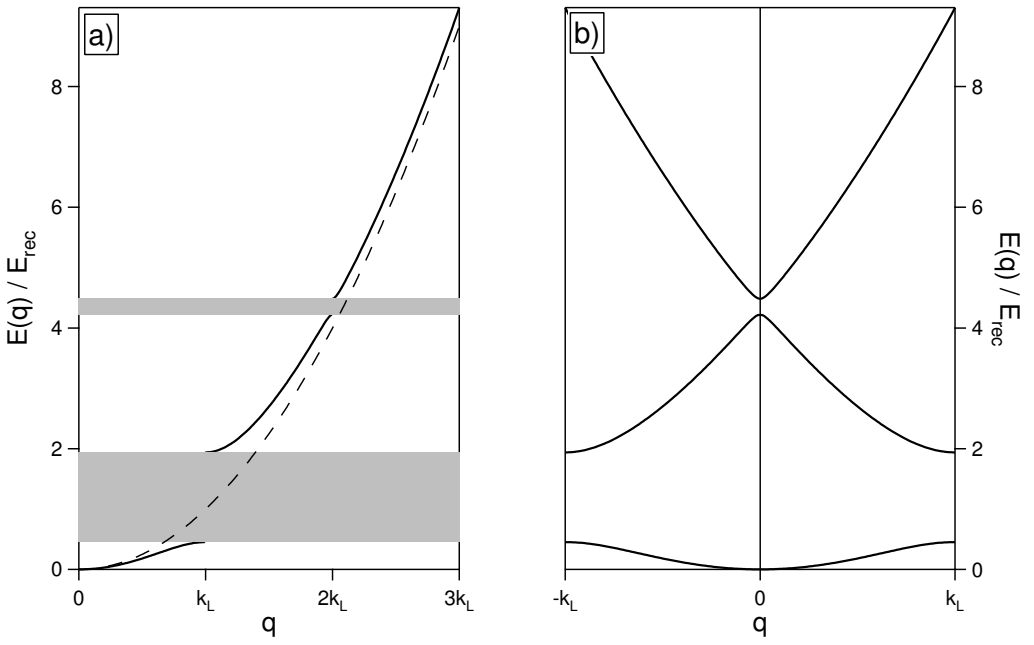

Figure 2.2: a) The dispersion law for the free particle (dashed line) is plotted together with the energy-vs-momentum curve in the presence of the periodic potential (continuous line): the shaded regions correspond to energy gaps; b) The energy spectrum is folded into the first Brillouin zone.

2.2.1 The bands

The most successful theory on periodic potentials in quantum mechanics is the Bloch theory of bands. In the presence of a spatial periodicity in the Hamiltonian

$$H = \frac{\nabla^2}{2m} + V(x) = \frac{\nabla^2}{2m} + V(x+L), \tag{2.5}$$

it can easily be demonstrated that the eigenstates have the form

$$|\psi_{n,q}(x)\rangle = \sum_q e^{iqx} |u_{n,q}(x)\rangle \tag{2.6}$$

where $|u_{n,q}(x)\rangle$ is periodic in space. For these eigenstates the energy spectrum has gaps in the energy dispersion relation at regular intervals of k_L. This

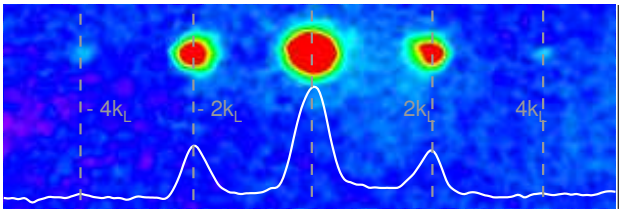

Figure 2.3: Typical *t.o.f.* picture of a BEC released from a lattice of depth 17 E_{rec} and integrated profile.

curve can be folded into the so called *first Brillouin zone* which is limited to the interval $q \in [-k_L; k_L]$ in quasi momentum space.

For our purposes it is fundamental to notice how the same phenomenon can be seen by using an atom-optics approach. Taking the Fourier transform of 2.6 we have

$$\begin{aligned} |u_{n,q}(x)\rangle &= \sum_j u_{n,q}(j) e^{i2jk_L} \\ &= \sum_j c_{n,q} |2jk_L\rangle \end{aligned} \tag{2.7}$$

and so the eigenstates can be written as

$$|\psi_{n,q}\rangle = \sum_j c_{n,j}(q) |q + 2jk_L\rangle. \tag{2.8}$$

$|\psi_{n,q}\rangle$ which can be interpreted as a superposition of plane waves produced after an m-th-order diffraction process. In the experimental realization this means that the state of the BEC in the optical lattice can be viewed as a superposition of velocity classes with discrete momenta $|q + 2jk_L\rangle$. A BEC suddenly released from the lattice (see figure 2.3) will appear in *time of flight* pictures as composed of different clouds located in space at positions $j \cdot (2t_{t.o.f.})/m$, each containing atoms that experienced j of cycles of absorption and emission of the lattice photons.

2.2.2 The two levels solution

The gaps resulting from Bloch theory can be also observed in a simple toy model closer to the atom optics approach. Let's consider a two level system composed of a ground state $|g\rangle$ and an excited level $|e\rangle$ in the presence of the lattice radiation. In the rotating wave approximation the hamiltonian is written as

$$H = \begin{pmatrix} -\hbar\Delta & \hbar\Omega_R \sin(k_L x)/2 \\ \hbar\Omega_R \sin(k_L x)/2 & 0 \end{pmatrix}, \tag{2.9}$$

where x is the mean value of the position (which is used as parameter) and Ω_R is the Rabi frequency $= \wp E_0/\hbar$. In the limit of large detuning, the upper state is not populated and can be adiabatically eliminated. The ground state eigenenergy will be the quantity

$$E_g = \hbar \frac{\Omega_R^2}{4\Delta} \sin^2(k_L x). \tag{2.10}$$

which is equivalent to saying that the atoms experience a conservative potential

$$\frac{V_0}{2} \cos(2k_L x), \tag{2.11}$$

where

$$V_0 = \hbar \frac{\Omega_R^2}{4\Delta} = 2\hbar\Omega_r^{(2)}. \tag{2.12}$$

The Hamiltonian $H(x) = \frac{p^2}{2m} + \frac{V_0}{2}\cos(2k_L x)$ can be solved exactly, and its eigenstates are expressed as sum of Matthieu functions. At the edge of the Brilloin zone on the base of the atomic plane waves $|+k_L\rangle$ and $|-k_L\rangle$ one finds

$$H = \begin{pmatrix} E_{\text{rec}} & V_0/4 \\ V_0/4 & E_{\text{rec}} \end{pmatrix}. \tag{2.13}$$

whose solutions are

$$\begin{aligned} E_0(k_L) &= E_{\text{rec}} - \tfrac{V_0}{4}; \quad |\psi_{0,k_L}\rangle = \tfrac{1}{\sqrt{2}}(|+k_L\rangle - |-k_L\rangle) \\ E_1(k_L) &= E_{\text{rec}} + \tfrac{V_0}{4}; \quad |\psi_{1,k_L}\rangle = \tfrac{1}{\sqrt{2}}(|+k_L\rangle + |-k_L\rangle). \end{aligned} \tag{2.14}$$

The previous calculations allow us to observe one of the key features of the energy spectrum of this problem. The Hamiltonian (2.13) has two eigenvalues $E_1(k_L)$ and $E_2(k_L)$ that are not degenerate, but have a difference in energy $\Delta E_0 = E_1(k_L) - E_0(k_L) = V_0/2$. This is equivalent to an *energy gap* in the dispersion law as observed in Bloch theory. We will see in a Section (2.5) how this approach is useful also as a calibration tool.

2.2.3 Tight binding Model and Wannier States

Another way to study a periodic system is to consider the localized wavefunction $|\phi_n\rangle$ of an atom in a single site and the perturbations coming from the neighbouring sites ([2] and [55]). This approximation deals with the case in which the overlap of atomic wavefunctions is enough to require corrections to the isolated atoms pictures, but not so much as to render the single site description irrelevant. We can assume that:

$$\begin{aligned} H_{n,n} &= \langle\phi_n|H|\phi_n\rangle = E_0 \\ H_{n,n\pm l} &= \langle\phi_n|H|\phi_{n\pm l}\rangle = J_l^{TB}, \end{aligned} \tag{2.15}$$

Therefore, the matrix representation of the Hamiltonian is:

$$H = \begin{pmatrix} \ddots & \ddots & & & & & \\ \ddots & E_0 & J_1^{TB} & J_2^{TB} & \ddots & J_l^{TB} & \\ & J_1^{TB} & E_0 & J_1^{TB} & J_2^{TB} & \ddots & \\ & J_2^{TB} & J_1^{TB} & E_0 & J_1^{TB} & J_2^{TB} & \\ & \ddots & J_2^{TB} & J_1^{TB} & E_0 & J_1^{TB} & \\ & J_l^{TB} & \ddots & J_2^{TB} & J_1^{TB} & E_0 & \ddots \\ & & & & & \ddots & \ddots \end{pmatrix}. \tag{2.16}$$

If the contributions from next-nearest sites are negligible, we are allowed to impose $H_{n,n\pm l} = 0$ for $l \neq 0, \pm 1$ (tight binding approximation) and H maintains again a diagonal structure.

$$H = \begin{pmatrix} \ddots & \ddots & & & & & \\ \ddots & E_0 & J_1^{TB} & 0 & 0 & 0 & \\ & J_1^{TB} & E_0 & J_1^{TB} & 0 & 0 & \\ & 0 & J_1^{TB} & E_0 & J_1^{TB} & 0 & \\ & 0 & 0 & J_1^{TB} & E_0 & J_1^{TB} & \\ & 0 & 0 & 0 & J_1^{TB} & E_0 & \ddots \\ & & & & & \ddots & \ddots \end{pmatrix}. \tag{2.17}$$

At this point the generic wave function can be written as a superposition of the localized wavefunctions (the *Wannier* functions):

$$\Psi(x) = \sum_n c_n \phi_n. \tag{2.18}$$

where ϕ_n are mutually orthogonal unlike single site wavefunctions. The time evolution for the coefficients c_n is given by:

$$\dot{c}_n = E_0 c_n + J_1^{TB}(c_{n+1} + c_{n-1}), \tag{2.19}$$

while the eigenstates can be calculated solving the set of equations:

$$E c_n = E_0 c_n + J_1^{TB}(c_{n+1} + c_{n-1}). \tag{2.20}$$

We note that the localized functions ϕ_n do not satisfy the Bloch theorem. We can avoid this problem by considering the following superposition of localized wave functions:

$$\Psi_q(x) = \frac{1}{\sqrt{N}} \sum_n e^{\imath q n d} \phi_n, \tag{2.21}$$

where N is the number of occupied sites. It is possible to show that the above expression satisfies the relation (2.8).

The energy dispersion for the fundamental band is thus given by:

$$E(q) = \langle \Psi_q(x)|H|\Psi_q(x)\rangle. \tag{2.22}$$

In the particular case that the matrix elements of H are given by (2.15), the above dispersion relation becomes:

$$E(q) = E_0 + 2J_1^{TB}\cos(qd) \tag{2.23}$$

The localized functions $|\phi_n\rangle$ in the case of a single isolated site are equivalent to the the eigenstates of a harmonic potential. Therefore the widths of the energy levels of the Wannier function are given by the perturbation added by the other sites, and thus the connection between the band width and the dispersion relation 2.23 becomes evident. Apart from its practical usefulness, the tight-binding approximation provides an instructive way of viewing Bloch bands, permitting a complementary point of view between the localized levels on one hand, and the free particle plane-wave levels on the other hand.

2.3 Setup for the optical lattices

The lasers used for the creation of our optical lattices are two MOPA (master oscillator power amplifier) (Toptica) which emit up to 750 mW at 842 nm. By splitting one of the principal laser beams, three beams were injected into three optical fibers (one for each spatial direction of the three-dimensional lattice) in order to purify the laser mode and to improve directional stability. The focusing lens and the cubes for the polarization cleaning are mounted directly on the output coupler (OzOptics) of the fiber. Three independent homemade PID controllers stabilize the intensities of the lattice beams. The weak reflections from the first surface of the vacuum chamber are sent to fast photodiodes whose signal is compared with the computer references. This stabilization is necessary to avoid spurious heating of the atoms and to calibrate the lattice depth. For our setup the calibration precision is around 5% and S/N ratio 10^4. In the configuration with counter-propagating laser beams the the lattice constant is 425 nm. With a 110 μm lattice waist at the position of the condensate and 70 mW power for each beam, an optical lattice depth of around 25 E_{rec} is produced. The standing wave was created by retro-reflecting the beam on itself or alternatively by crossing the light from two different fibers. Moreover the spectral mode of the laser was continuously controlled by using two Fabry-Perot interferometers. A single

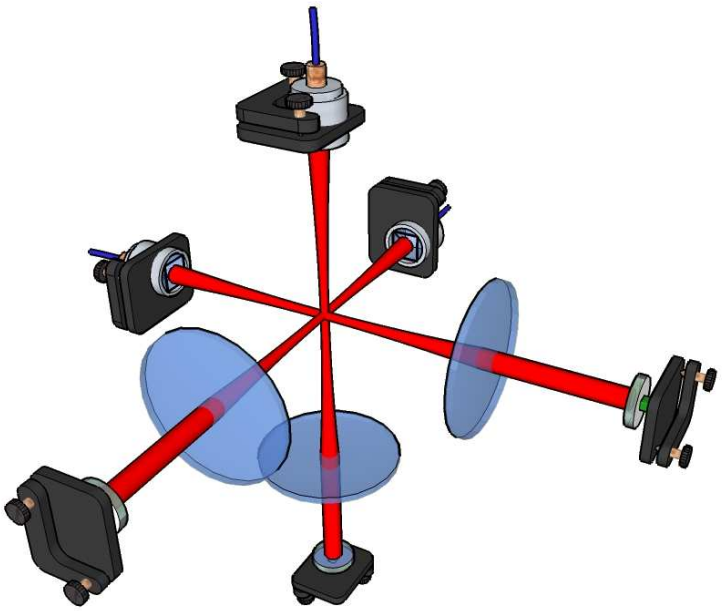

Figure 2.4: Schematic view of the set -up of the optical lattice for the configuration with three retro-reflected beams.

frequency mode of the laser is in fact required in order to avoid the creation of uncontrolled multiple lattices at the same time.

2.4 Basic adiabaticity

Since the beginning of quantum mechanics ([5]), the adiabatic transfer of a eigenstate of a solvable Schrödinger equation to a perturbed one has been extensively studied. In this paragraph the adiabatic theorem is summarized for a better understanding of the adiabaticity of the loading of the condensate into an optical lattice (paragraph 2.4.2) and the following experiments with a periodically driven potential (paragraph 4.1).

2.4.1 The adiabatic theorem

Theoretically, adiabaticity can be treated by solving a time-depedent Schrödinger equation

$$i\hbar\partial_t|\psi(t)\rangle = [H_0 + V(P(t))]\,|\psi(t)\rangle \tag{2.24}$$

which contains a term $V(P(t))$ varying in time. For a slow change of the parameter, the strategy is to "freeze" the parameter and to solve the time-

independent equation

$$E_n^P|\psi_n(P)\rangle = [H_0 + V(P)]\,|\psi_n(P)\rangle \tag{2.25}$$

The evolution of the initial wavefunction will be expressed as a superposition of the instantaneous eigenstates

$$|\psi(t)\rangle = \sum_n c_n(t) e^{\left(-\frac{i}{\hbar}\int_o^t dt' E^{P(t')}\right)} |\psi_n(P)\rangle \tag{2.26}$$

where $c_n(0)$ takes into account the decomposition of the system at $t = 0$. By considering the system initially in a particular state $|\psi(t=0)\rangle = |\psi_0(P(t=0))\rangle$ and so $c_0(t=0) = 1$, the transition to a state with $k \neq 0$ after a time T can be evaluated as

$$c_k(T) \simeq i\hbar \frac{e^{\frac{i}{\hbar}(E_k - E_0)T}}{|E_k - E_0|^2} \langle\psi_k(P)|\frac{\partial H}{\partial t}|\psi_0(P)\rangle. \tag{2.27}$$

From this equation it is easy to obtain the adiabatic condition:

$$\left|\left(\frac{\partial H}{\partial t}\right)_{k0}\right| \ll \frac{|E_k - E_0|^2}{\hbar}. \tag{2.28}$$

2.4.2 Adiabaticity in the bands

The loading of the atoms into a periodic potential is the first application of the adiabatic theorem useful for a better understanding of the experiments shown in the next chapters. By considering the BEC initially as a plane wave $|p\rangle$, we consider what happens if the lattice is switched on suddenly at $t = 0$ at a lattice depth V_0. The plane waves are not eigenstates of the Hamiltonian of the lattice, therefore, the state of the atoms in the basis of the Bloch states $|\psi_{n,q}\rangle$ is:

$$|\psi\rangle_{t=0} = \sum_n |\psi_{n,q}\rangle\langle\psi_{n,q}|q\rangle \tag{2.29}$$

where q is the momentum of the atoms in the first Brillouin zone, and n is the band index. The probability for the atoms to be in the $|\psi_{n,q}\rangle$ Bloch state is $\langle\psi_{n,q}|p\rangle$.

However, in most of our experiments, we wanted the atoms to populate only the ground state. This can be achieved by loading the lattice in a time τ_{on} such that the atomic wavefunction follows the instantaneous adiabatic state. When this is the case the initial free particle state $|p\rangle$ is connected to

one single Bloch state $|\psi_{n,q}\rangle$ whose band index n and quasimomentum q are such that:

$$|p| = (n-1)k_L + |q|. \tag{2.30}$$

The adiabatic condition 2.28 can be expressed as:

$$\left|\langle\psi_{n',q}|\frac{d}{dt}|\psi_{n,q}\rangle\right| \ll \frac{|E_{n'} - E_n|}{\hbar}. \tag{2.31}$$

Therefore the loading of the optical lattice is adiabatic if the condition (2.31) holds for any Bloch state with $n' \neq n$. However, the most restrictive condition is for the band that is closest in energy, that is for $n' = n \pm 1$. Let us suppose that we are interested in loading the condensate in the $|\psi_{1,0}\rangle$ state of the fundamental band. Therefore, the loading will be adiabatic if the condition (2.31) holds for $n' = 2$, i.e., for the Bloch state of quasimomentum $q = 0$ in the first excited band. In the limit of a shallow lattice, the gap between the fundamental and the first excited state can be approximated with its value in the free particle case: $|E_{n'} - E_n| \simeq 4E_{\rm rec}$. Therefore the condition (2.31) can be written [71]:

$$\frac{d}{dt}\frac{V_0}{E_{\rm rec}} \ll 32\sqrt{2}\frac{E_{\rm rec}}{\hbar}. \tag{2.32}$$

For a linear ramp of the lattice depth in τ_{on}, the condition (2.32) reduces to the following condition for τ_{on}:

$$\tau_{on} \gg \tau_{ad} = \frac{1}{32\sqrt{2}\omega_{\rm rec}}\frac{V_0}{E_{\rm rec}} \tag{2.33}$$

where $\omega_{\rm rec} = E_{\rm rec}/\hbar$.

The adiabaticity condition (2.33) is valid even in the opposite situation when the lattice is switched off in a time τ_{off}. In fact, if $\tau_{off} \ll \tau_{ad}$ the wavefunction of the atoms will be formed by the plane wave decomposition, i.e., the Fourier transform, of the wavefunction of the atoms in the lattice. On the other hand, if $\tau_{off} \gg \tau_{ad}$ the wavefunction of the atoms follows the adiabatic state instantaneously, and hence if the wavefunction of the atoms in the lattice was a single Bloch state, the wavefunction of the atoms when the lattice is switched off is a single plane wave.

Depending on the loading time τ_{on} and on the time τ_{off}, the behavior of the system changes [24]. The regimes realized in our experiments are listed in the following.

- τ_{on}, $\tau_{off} \ll \tau_{ad}$. In this case the initial state of the atoms is a superposition of many Bloch states, as in Eq.(2.29). Then, if the system is

allowed to evolve in time inside the lattice, each of these Bloch states evolves with a different phase, and after a time t the state of the atoms is:

$$|\psi\rangle_t = \sum_n e^{-iE_n(q)t/\hbar}|\psi_{n,q}\rangle\langle\psi_{n,q}|q\rangle. \tag{2.34}$$

After a fast switching off of the lattice, the atomic wavefunction is the Fourier transform of Eq.(2.34). Thus the probability for the atoms to be in the state $|p+2jk_L\rangle$ is:

$$P_{p+2jk_L} = \left|\sum_n e^{-iE_n(q)t/\hbar}\langle p+2jk_L|\psi_{n,q}\rangle\langle\psi_{n,q}|q\rangle\right|^2. \tag{2.35}$$

Measurements in this regime can be used to measure the lattice depth by exploiting the Kapitza-Dirac effect ([38] ,[68]).

- τ_{on}, $\tau_{off} \gg \tau_{ad}$. In this case the atomic wavefunction at the end of the experiment is equal to the atomic wavefunction before the lattice was switched on. Measurements in this regime were used in the experiment to test the adiabaticity of loading.

- $\tau_{on} \gg \tau_{ad}$, $\tau_{off} \ll \tau_{ad}$. The wavefunction of the atoms in the lattice is a single Bloch state $|\psi_{n,q}\rangle$, because of the adiabatic loading. On the other hand, the atomic state observed after switching off the lattice is the Fourier transform of $|\psi_{n,q}\rangle$. The probability to have an atom with momentum $2k_L$ is:

$$P_{p+2jk_L} = |\langle p+2jk_L|\psi_{n,q}\rangle|^2. \tag{2.36}$$

2.4.3 Adiabatic loading into a lattice

The adiabatic condition 2.32 for loading into the periodic potential can be quantified for typical parameters of our experiments such as $d_L = 421\,\text{nm}$, $V_0 = 5E_{\text{rec}}$. The condition (2.33) becomes: $\tau_{on} \gg 5\,\mu\text{s}$. It must be noted that the condition (2.33) was found for $q = 0$, i.e., for the value of quasimomentum for which the gap between the fundamental and the first excited band is maximum. In fact, the adiabaticity condition for loading the atoms into the fundamental band becomes more restrictive when $q \neq 0$. In particular, for $|q| = k_L$ the time τ_{ad} diverges and the adiabatic loading is impossible. This is true for every point in the band structure for which the bands are degenerate in the free particle case.

As the gap between the ground state and the first excite state increases with the lattice depth, the time for an adiabatic loading decreases in deeper

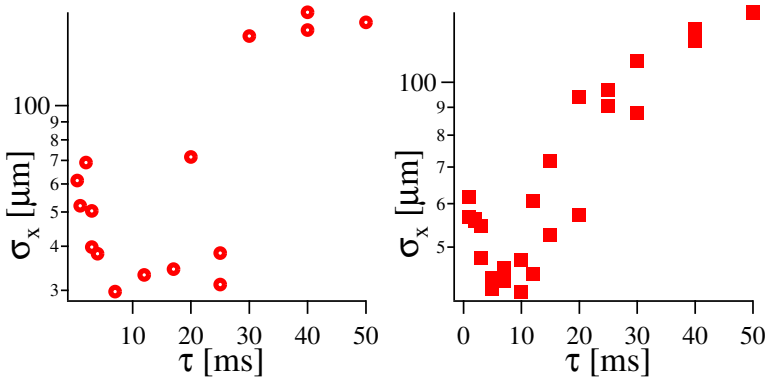

Figure 2.5: Width of the cloud in *time of flight* detection for different values of the characteristic time τ_{ramp} of the exponential ramp of lattice depth in one (on the left) and two (on the right) lattice beams. After the ramp of 250 ms in 1D (200 ms in 2D) to the maximum value of $V_0 = 40$ (25 $E_{\rm rec}$), the lattice depth was ramped down to 5 $E_{\rm rec}$ for the thermalization of the ensemble.

lattices. This is equivalent to saying that $\partial V_0(t)/\partial t$ is proportional to $V_0(t)$ (for details see [37]). For this reason in our experiment the ramp of the lattice depth had an exponential slope

$$V(t) = V_0 \frac{e^{t/\tau_{ramp}} - 1}{e^{L/\tau_{ramp}} - 1}, \tag{2.37}$$

whose length L and characteristic time τ_{ramp} were optimized with the following procedure:

- **a)** ramp up the lattice depth to V_0;
- **b)** holding for a time ∼30 ms;
- **c)** decreased the lattice depth V_0 to a 5 $E_{\rm rec}$ in 15 ms (value verified in other measurements) to allow the atoms to thermalize
- **d)** *time of flight* detection of the cloud.

As a larger width of the cloud corresponds to more energy in the ensemble, the time τ_{ramp} for which the cloud is narrowest corresponds to the optimum value. Figure 2.5 shows the scans performed with one or two perpendicular lattice beams by changing the characteristic time τ.

The existence of an optimum time is evident in both the scans. It could be surprising that the value is clearly higher than the predicted lower limit.

The contributions of the interactions between atoms to the chemical potential ([66]) are not negligible as a large number of atoms in each site leads to low energy excitations which release the energy of the system without excite it to the upper band. Moreover even if from condition 2.28 a longer ramp should be a better choice, a limit for long ramp is evident and due to the lifetime of the condensate in the lattice. This lifetime is limited by the technical stability for the parameters as lattice depth and phase fluctuation of the laser light and the lengths used in the scan (250 ms and 200 ms) are close to the maximum lifetime.

A small contribution is given also by a small dipolar confinement effect added by the lattice beams (see 2.1). For our parameters[1] at a lattice depth of 25 E_{rec} the additional trap frequency can be estimated to be $\sim$ 20 Hz (when only the dipolar trap frequency is 70 Hz). Hence a too fast switching on could introduce also sudden movement and deformations of the initial trap potential. For this reason the alignment of the lattice beam with the dipolar trap has been extremely critical especially in the configuration with three beams.

2.5 Calibration of the lattice

The lattice depth is the first important quantity to measure and calibrate in our measurements. The different methods we used for the experiments of this thesis were the following.

- **Rabi Oscillation**: The cold atoms are loaded into a lattice moving at a velocity equal to v_{rec}, at the edge of the first Brillouin zone where they are in a superposition of the ground band and of the first exited band. The depth of the lattice is suddenly switched on up to a final value of V_0 that implies a band gap of $V_0/2$ in the shallow lattice. While the numbers of atoms inside the two levels remain constant, the phase of the wave functions of the atoms inside the two populations accumulate a difference of $(V_0/2\hbar)t$ due to Hamiltonian time evolution. In the rest frame of the laboratory, one observes oscillations between the relative populations of the two momentum classes, 0 (the N_0/N_{tot} population) and $2\hbar k_{\mathrm{rec}}$ (the N_1/N_{tot} population). From the frequency Ω of these oscillation we can derive V_0 as:

$$V_0 = 2\hbar\Omega. \tag{2.38}$$

[1] 100 μm for the waist and 80 mW of power

In Fig.(2.6) the measurement of the ratio N_{-1}/N_{tot}, where N_{tot} is the total number of atoms in the sample, is reported as a function of the time the condensate spent in the lattice.

Using the notation of the two-level approach (paragraph 2.2.2), this calibration corresponds to considering the eigenfunction

$$|\psi(t) = \frac{1}{\sqrt{2}} e^{iE_{\rm rec}t/\hbar}(e^{-iV_0t/\hbar}|\psi_{0,k_L}\rangle + e^{+iV_0t/\hbar}|\psi_{1,k_L}\rangle) \tag{2.39}$$

and measuring the probability at time t that the atomic momentum has at the initial value k_L.

$$|\langle +k_L|\psi(t)\rangle|^2 = \sin^2\left(\frac{V_0}{4\hbar}t\right) = \frac{1}{2}\left(1 - \cos\left(\frac{V_0}{2\hbar}t\right)\right). \tag{2.40}$$

This last calculation is equivalent to considering the two velocity classes in the moving frame of the lattice, where the lattice light acts as a perturbation. For this reason the population oscillations are referred to as *Rabi Oscillations*.

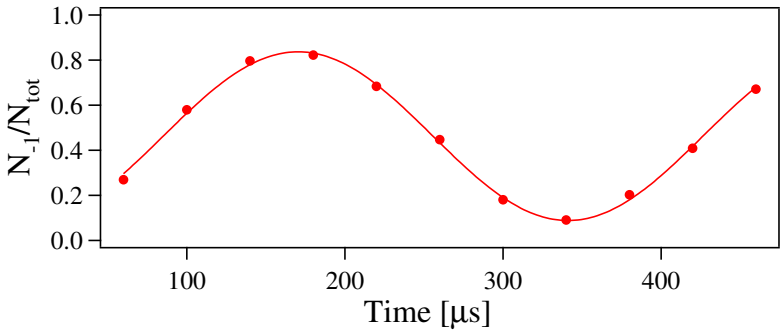

Figure 2.6: Rabi oscillations of the number of atoms in the velocity classes $-2v_{\rm rec}$ as a function of time for a lattice of depth 1.6 $E_{\rm rec}$.

- **Landau Zener tunneling**: By introducing a constantly increasing frequency shift between the two counter-propagating laser beams, it is possible to simulate the effect of a force F ([68] and reference within) and to measure the probability of tunneling from the ground state to the upper band in a single crossing at the edge of Brilloiun zone. The rate for the single passage can be estimated from the Landau-Zener formula ([58] and [87]). This formula gives the non-adiabatic transition

probability between two levels (in our case, the two bands) and depends exponentially on the lattice parameters:

$$\frac{N_{tun}}{N_{ini}} = r = e^{-\frac{md_L(\Delta E)^2}{16\hbar^2 F}} \tag{2.41}$$

where N_{tun} are the atoms that have undergone the transition to the higher band and N_{ini} the total number of atom which are accelerated and m is the mass, d the lattice and ΔE the band gap. The exponential decay allows us to calibrate the depth with high precision as the error of the frequency shift introduced by the function generator is negligible

- **Side Peak Population**: Assume that a BEC is loaded into an optical lattice and has an initial wavefunction that is a Bloch state $|\psi_{0,0}\rangle$. If all the lattice sites are occupied with uniform filling, the atomic Bloch state can be approximated as a sum of gaussian functions of equal width σ centered at each lattice site:

$$|\Psi_{0,0}(x)\rangle \propto \sum_{n\in lattice} \exp\left(-\frac{(x-x_n)^2}{2\sigma^2}\right), \tag{2.42}$$

where x_n is the position of the n-th site. As in the multiple slit diffraction pattern in geometric optics, the Fourier transform of the expression (2.42) is [70]:

$$\begin{aligned}\Psi_{0,0}(p_x) &\propto \exp\left(-\frac{p^2\sigma^2}{2\hbar^2}\right)\frac{\sin\left[(2k_L+1)pd_L/2\hbar\right]}{\sin\left(pd_L/2\hbar\right)} \\ &= \exp\left[-\frac{\pi^2}{2}\left(\frac{p}{p_B}\frac{\sigma}{d_L}\right)^2\right]\frac{\sin\left[(2k_L+1)\pi\frac{p}{p_B}\right]}{\sin\left[\pi\frac{p}{p_B}\right]}\end{aligned} \tag{2.43}$$

where $p_B = 2\hbar k_L$. The interference pattern that is observed in a time of flight measurement after the lattice is switched off abruptly (like in Figure 2.3) is, therefore, a structure of peaks of the form $\sin(x)/x$ spaced by $\delta x = t_{tof} \times p_B/m$, and whose amplitude is given by a gaussian envelope centered at $p = 0$. The amplitude of the first side peaks ($p = \pm p_B$) with respect to the amplitude of the central one is:

$$P_{\pm 1} = \exp\left(\frac{-4\pi^2\sigma^2}{d_L^2}\right). \tag{2.44}$$

The value of sigma depends on the potential depth [70] and can be estimated variationally. It is possible to show [80, 16] that σ satisfies

the following relation:

$$\exp\left[-\left(\frac{\sigma}{\sigma_h}\right)^2\sqrt{\frac{E_{\rm rec}}{V_0}}\right]=\left(\frac{\sigma}{\sigma_h}\right)^{-4}, \tag{2.45}$$

with:

$$\sigma_h=\frac{d_L}{\pi}\left(\frac{V_0}{E_{\rm rec}}\right)^{-1/4}. \tag{2.46}$$

By use of the relation (2.44) and Eq.(2.45) the lattice depth V_0 can be written as:

$$\frac{V_0}{E_{\rm rec}}=\frac{P_{\pm1}^{-1/4}}{(\ln P_{\pm1}^{1/4})^2}. \tag{2.47}$$

where $P_\pm$ are the ratios between the number of atoms in the first order diffracted velocity classes and the number of atoms in the central peak.

Chapter 3

Dynamical control of matter-wave tunneling

A powerful model for the theoretical treatment of cold atoms confined in an periodic optical potential is the Bose Hubbard model (B.H.). In this chapter I will introduce it and in particular its modifications in the presence of an external periodical force. After a theoretical review, I will show how it is possible to measure the dynamical microscopic effects looking at their macroscopic manifestations in the behavior of a BEC ([60]). I will argue that from these observations the concept of *dressed matter wave* naturally suggests itself.

3.1 The Bose Hubbard Model

3.1.1 The 1D model

A simple model for a system of atoms in a one-dimensional optical lattice is to consider thermal fluctuations and interaction energies in a single site to be smaller than the gap between the ground state and the first excited level. This tight-binding-like approximation proposed in [50] starts from the many body Hamiltonian (Eq. 1.9 with the periodic potential $V_0/2\cos(2k_Lx)$ added)

$$\begin{aligned} H = &\int d^3r\hat{\Psi}^\dagger(\mathbf{r})\left(-\frac{\hbar^2}{2m}\nabla^2+\frac{V_0}{2}\cos(2k_Lx)\right)\hat{\Psi}(\mathbf{r})+ \\ &+\frac{1}{2}\frac{4\pi a_s\hbar^2}{m}\int d^3r\hat{\Psi}^\dagger(\mathbf{r})\hat{\Psi}^\dagger(\mathbf{r})\hat{\Psi}(\mathbf{r})\hat{\Psi}(\mathbf{r}), \end{aligned} \tag{3.1}$$

where $\hat{\Psi}(\mathbf{r})$ is again the Bose field operator in a three dimensional space of coordinate $\mathbf{r} = (x, y, z)$, and the 1D optical lattice is along the x direction. The 3D Hamiltonian (3.1) is separable in three 1D Hamiltonians. In the y, z directions the Bose-field operator can be approximated by a single particle wavefunction $\Phi(y, z)$. In the x direction, the Bose field operator can be expanded in terms of the boson creation and annihilation operators $a_l^\dagger$, a_l at a single lattice site:

$$\hat{\Psi}^{(\dagger)}(x) = \sum_l a_l^{(\dagger)} \phi_l(x - x_l), \tag{3.2}$$

where the amplitude of each term is given by the corresponding Wannier function. The expansion (3.2) can be now substituted into the Hamiltonian (3.1). If only the hopping between neighboring sites is considered[1], then the Hamiltonian along the x axis is:

$$H = -J \sum_{\langle l,j \rangle} a_l^\dagger a_j + \frac{U}{2} \sum_l n_l(n_l - 1) \tag{3.3}$$

where:

- the sum $\langle l, j \rangle$ is over nearest neighboring sites;
- $n_l = a_l^\dagger a_l$ is the number operator that counts the number of atoms at the n-th site;
- $J = \int dx \phi(x - x_l) \left(-\frac{\hbar^2}{2m} \nabla^2 + \frac{V_0}{2} \cos(2k_L x) \right) \phi(x - x_j)$ is the hopping matrix element that considers the tunneling from one lattice site to the first neighboring one. J here defined is equivalent to J_1^{TB} of the tight-binding model of section 2.2.3;
- $U = \frac{1}{2} \frac{4\pi a_s \hbar^2}{m} \int dx \, |\phi(x)|^4$ is the interaction energy of two atoms occupying the same lattice site.

The dynamics of cold atoms in deep lattices is expressed in the Bose-Hubbard model by using only the two parameters U (the on-site energy that disfavors the presence of more than one particle per site) and J (the kinetic energy

[1] A systematic extension of the Hamiltonian with higher powers of the annihilation and creation operators (EBH [64]) can consider the contribution of neighbouring sites of higher order

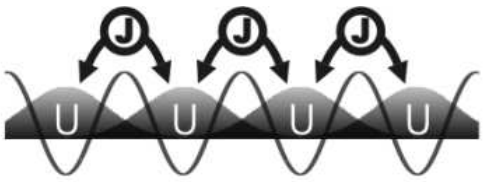

Figure 3.1: Schematic view of one dimensional Bose Hubbard Model. U is the on-site energy due to interactions, J is related to the tunneling events.

that favors tunneling and the delocalization of the particles). By using simple approximations on the wavefunction, the dependence of U and J on the lattice depth V_0, for the system with only one dimension, are [88]:

$$\begin{aligned} J &= \frac{4}{\sqrt{\pi}} E_{\mathrm{rec}} \left(\frac{V_0}{E_{\mathrm{rec}}}\right) \exp\left(-2\sqrt{\frac{V_0}{E_{\mathrm{rec}}}}\right) \\ U &= \sqrt{\frac{8}{\pi}} k a_s E_{\mathrm{rec}} \left(\frac{V_0}{E_{\mathrm{rec}}}\right)^{1/4} \end{aligned} \tag{3.4}$$

In the experimental realization it is necessary to consider the two directions along which the lattice is not present. The energy contribution to the system can be evaluated by writing $\Phi(y,z)$ as wavefunction of a wavepacket confined in the weak harmonic potential that in our case is due to the dipolar trap confinement of the cloud. The parameter U_{tot} in the one-dimensional system will be $\frac{1}{2}\frac{4\pi a_s \hbar^2}{m} \int dxdydz \left|\phi(x)\right|^4 \left|\Phi(y,z)\right|^4$ that becomes:

$$U_{\mathrm{tot}}^{1D} = \sqrt{\frac{8}{\pi}} k a_s E_{\mathrm{rec}} \left(\frac{V_0}{E_{\mathrm{rec}}}\right)^{1/4} \frac{\hbar\sqrt{\omega_y \omega_z}}{E_{\mathrm{rec}}}. \tag{3.5}$$

3.1.2 Extension to 2D or 3D

It's trivial at this point to extend the model to a system with two or three lattice directions. From the separability of the Hamiltonian one easily finds for the 2D case:

- $J_{\mathrm{tot}}^{2D} = J_x + J_y$ for the hopping term;

- U_{tot}^{2D} contains two contributions from the lattice and only one from the trap.

$$U_{\text{tot}}^{2D} = \sqrt{\frac{8}{\pi}} k a_s E_{\text{rec}} \left(\frac{V_0}{E_{\text{rec}}}\right)^{2/4} \sqrt{\frac{\hbar\omega_z}{E_{\text{rec}}}}. \tag{3.6}$$

And for the configuration with three lattices

- $J_{\text{tot}}^{3D} = J_x + J_y + J_z$;
- U_{tot}^{3D} contains only three contributions from the lattice

$$U_{\text{tot}}^{3D} = \sqrt{\frac{8}{\pi}} k a_s E_{\text{rec}} \left(\frac{V_0}{E_{\text{rec}}}\right)^{3/4}. \tag{3.7}$$

Even in its simplicity, the Bose Hubbard Model is a powerful tool and it has been fundamental in predicting the superfluid—Mott-insulator transition we are going to demonstrate in chapter 5 and 6 and the equations 3.6 and 3.7 will be very useful for the characterization of the system.

3.2 BEC in driven optical potentials

We now want to introduce a periodic driving (often referred to as *shaking* in this thesis) in the system of atoms inside the optical lattice. Technically it is applied as a backwards and forwards motion of the periodic potential (paragraph 3.2.1), which in the presence of the lattice is equivalent to a periodic force applied to the atoms (paragraph 3.2.2).

3.2.1 The Floquet states

A sinusoidal motion of the lattice can be introduced in the Hamiltonian [42, 30] as :

$$\hat{H}_{FM}(t) = K \cos(\omega t) \sum_j j \hat{n}_j \tag{3.8}$$

where K is the modulation amplitude and ω its frequency. The full Hamiltonian $\hat{H}_T(t)$ then reads:

$$\hat{H}_T(t) = \hat{H}_{BH} + \hat{H}_{FM}(t) = \hat{H}(t+T) \tag{3.9}$$

where $T = 2\pi/\omega$. The full Hamiltonian is now periodic in time with period T and a good strategy for this theoretical problem is to use a semiclassical

approach by the so-called Floquet theory [78]. The Schrödinger equation written as

$$i\hbar\frac{\partial}{\partial t}|\psi_n(t)\rangle = \hat{H}_T|\psi_n(t)\rangle \tag{3.10}$$

has solutions of the form:

$$|\psi_n(t)\rangle = |u_n(t)\rangle \exp\left[-i\frac{\epsilon_n t}{\hbar}\right] \tag{3.11}$$

where the so-called *Floquet mode* $|u_n(t)\rangle = |u_n(t+T)\rangle$ is again periodic in time with period T. The energy ϵ_n is called a *quasienergy* because of the formal analogy with the quasimomentum in the Bloch problem in a spatially periodic Hamiltonian. By substituting the Floquet solution (3.11) into the Schrödinger equation (3.10) one arrives at the following relation for the Floquet mode [76]:

$$\left(\hat{H}_T(t) - i\hbar\frac{\partial}{\partial t}\right)|u_n(t)\rangle = \epsilon_n|u_n(t)\rangle. \tag{3.12}$$

Eq.(3.12) can be interpreted as an eigenvalue problem by defining the Hamiltonian $\hat{\mathcal{H}} = \hat{H}_T - i\hbar\partial/\partial t$ in an extended Hilbert space $\mathcal{R}\otimes\mathcal{T}$, where $\mathcal{T}$ is the space of the time periodic functions of period T and $\mathcal{R}$ is the Hilbert space of square integrable functions on the configuration space. It is important to note that if $|u_n(t)\rangle$ is a solution of Eq.(3.12) with eigenvalue ϵ_n, then $|u_{n,m}(t)\rangle = |u_n(t)\rangle\exp(im\omega t)$ is also a solution of Eq.(3.12) with eigenvalue $\epsilon_n + m\hbar\omega$, where $m = \pm1, \pm2, ...$ The quasienergy spectrum has a Brillouin-zone-like structure, where the width of one zone is $\hbar\omega$.

By using the Houston functions [45] (a different procedure leading to the same result was used by Ref. [25]) it can be demonstrated that the presence of a driving force corresponds to a renormalization of the Bose Hubbard Hamiltonian

$$H = -J_{\text{eff}}\sum_{\langle l,j\rangle} a_l^\dagger a_j + \frac{U}{2}\sum_l n_l(n_l-1) \tag{3.13}$$

where the parameter J is substituted by J_{eff} depending on the amplitude, the frequency and the shape of the forcing. This solution allows us also to consider the case of an additional static force (theory in [56] and [27] and experimental realization in [79] and [48]).

3.2.2 The band model

For our purposes, it's clearer to show the simple model that can be considered when the amplitude of the shaking is weak compared to the energy scale of

the undriven lattice, i.e., if $K \ll J, U$. In this case the effect of the shaking is reduced to a change in time of the quasimomentum $q(t)$ inside the the energy bands of the unshaken lattice $E_n(k)$. Hence the relation:

$$\dot{q_k}(t) = F(t) \tag{3.14}$$

can be integrated and the evolution of the quasimomentum q in time is:

$$q_k(t) = q_0 + \frac{1}{\hbar}\int_{t_0}^{t} d\tau F(\tau) \tag{3.15}$$

The fundamental energy band $E_0(q_k(t))$ as seen in the tight-binding model can hence be written substituting the quasimomentum of Eq.(3.15) in

$$\begin{aligned} E(k) \to E_0(q_k(t)) &= E_0 + \sum_{l=1}^{\infty} 2\langle \phi_0 \left| H_0 \right| \phi_l \rangle \cos(l q_k(t) d_L) = \\ &= E_0 + \sum_{l=1}^{\infty} 2J_l \cos(l q_k(t) d_L) \end{aligned} \tag{3.16}$$

where $\langle \phi_0 \left| H_0 \right| \phi_l \rangle$ is the undriven Hamiltonian evaluated on two Wannier states located l sites apart. Even if the Bose Hubbard Model takes into consideration only the nearest-neighbour tunneling $J_1 = \langle \phi_0 \left| H_0 \right| \phi_1 \rangle$ (compare with equation 3.4 and 2.15), for shallow lattices the contribution of the tunneling rate to the next-nearest neighbouring sites J_2 is not small and can be analytically quantified (see figure 3.2). Neglecting all the terms $J_n, n \geq 2$ the relative error is on the order of 10% for a lattice depth V_0 of 3 E_{rec} and reduces to 1% for 10 E_{rec}. The small contribution for lattice with $V_0 = 10$ E_{rec} explains the good agreement between the Bose Hubbard Model and its experimental realization.

The modified shape of the band can therefore be calculated by integrating Eq.(3.16) in time over a period of the shaking $T = 2\pi/\omega$. (It's important to notice that the shape of the forcing wave is not used up to now).

$$\epsilon(k) = \frac{1}{T}\int_{0}^{T} dt E(q_k(t)). \tag{3.17}$$

- **Sinusoidal force**
  We first consider the case of sinusoidal shaking (remember that K has the dimension of an energy):

$$F_{sin}(t) = \frac{K}{d_L}\cos(\omega t) \tag{3.18}$$

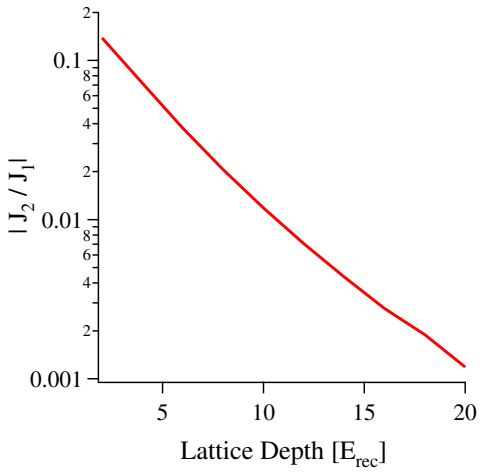

Figure 3.2: Ratio between second and first neighbouring tunneling hopping matrix terms as a function of lattice depth V_0.

By substituting 3.18 in 3.15 the integration gives:

$$\frac{1}{T}\int_0^T dt\, \cos(lq_k(t)d_L) = \mathcal{J}_0\left(\frac{lK}{\hbar\omega}\right)\cos(lkd_L). \tag{3.19}$$

Hence the final dispersion relation is

$$\epsilon(k) = E_0 + \sum_{l=1}^{\infty} 2J_l\mathcal{J}_0\left(\frac{lK}{\hbar\omega}\right)\cos(lkd_L) \tag{3.20}$$

where $\mathcal{J}_0$ is the zero-th order Bessel function. When $K_0 = \frac{K}{\hbar\omega}$ (l=1) is equal to the first zero of $\mathcal{J}_0$, the contribution of tunneling between first neighboring sites in the spectrum is zero. The fundamental band of the shaken lattice hence corresponds to the fundamental band of the unshaken lattice but with the tunneling J (reflecting the band width) substituted by its effective value $J_{\text{eff}}(K_0) = J\mathcal{J}_0(K_0)$. The same result can be obtained by using an analytical solution of the Floquet problem and one can find that the modified band is obtained by substituting the hopping term J with the renormalized one.

- **Squarewave force**
  In the case of the square wave forcing the force is

$$F(t) = \begin{cases} \frac{K}{d_L}, & 0 \le t \le T/2 \\ -\frac{K}{d_L}, & T/2 \le t \le T \end{cases} \tag{3.21}$$

repeated periodically for all t. This gives a quasimomentum:

$$q_k(t) = \begin{cases} k + \frac{K}{d_L}\frac{(t-T/4)}{\hbar}, & 0 \le t \le T/2 \\ \\ k + \frac{K}{d_L}\frac{(3T/4-t)}{\hbar}, & T/2 \le t \le T \end{cases} \tag{3.22}$$

As before, using 3.16 and 3.17

$$\frac{1}{T}\int_0^T dt\, \cos(lq_k(t)d_L) = \text{sinc}\left(\frac{l\pi K}{2\hbar\omega}\right)\cos(lkd_L) \tag{3.23}$$

and so

$$\epsilon(k) = E_0 + \sum_{l=1}^{\infty} 2J_l \text{sinc}\left(\frac{l\pi K}{2\hbar\omega}\right)\cos(lkd_L). \tag{3.24}$$

In this case an exact dynamical localization takes place. Independently of the lattice depth or the form of wave packet, when $K/\hbar\omega = 2n$ (with n integer =1,2...) the sinc function is identically zero and all the terms of the sum, for every order l of neighbouring sites, are zero. This behavior corresponds to a complete collapse of the band.

The calculations done in this paragraph show how the tunneling term J and consequently the band shape can be engineered by changing the shape of the driving force. It could, e.g., be possible to realize systems where the odd terms J_n are suppressed or only the even ones, ore even use multiple frequency driving ([56]) to originate an enhanced control on the different tunneling energies.

3.3 From dressed atoms to dressed matter-waves

The results presented in the previous paragraph are very general, because the same theoretical approach can be used to describe any experiment in which a physical system is subjected to a strong time-periodic driving potential. An example in the literature is an experiment reported in 1970 by Haroche *et al.* [43], where the Zeeman hyperfine spectrum of ^{87}Rb and ^{1}H was measured in the presence of a static magnetic field B and an orthogonal radio-frequency field $B_1\cos(\omega t)$. A variation of the peak positions in the atomic spectrum was observed when the oscillating field was present. The experimental data were fitted very well by substituting the Landé g-factor with an "effective" one $\bar{g}_F$: $\bar{g}_F = g_F\mathcal{J}_0(g_F\mu_B B/\omega)$ [13].

Although this effect was interpreted by the authors within the *dressed-atom* approach, the experiment can be perfectly described within the Floquet theory by use of the same procedure introduced above [45]. The results shown in this thesis represent a confirmation of Floquet theory, and at the same time, are an example of its application to an ensemble of atoms. This is the case of a *dressed matter-wave* where the shaking becomes a *dressing* that can take the system into a regime where the time-periodical perturbation behaves like a time-independent parameter (J_{eff}). This feature allows us to *simulate* regimes impossible to reach by changing the lattice depth, the atomic species etc. At the same time the realization of such a system allows us to study the Floquet states for large numbers of atoms and lattice sites, which is extremely complicated from the computational point of view.

3.4 Experimental setup for shaking

The set up for the experiment in shaken lattices has been done in two different ways:

- **Two counter-propagating beams**: in this configuration two beams are focused on the atoms from two opposite directions. The two beams come from different fibers and pass trough two separate acousto-optic modulators (AOM). Each AOM is driven by a function generator (Agilent 3325A) whose frequency can be modulated both with internal preset functions or by using a triggered external channel. The power of the two beams is separately stabilized by our homemade PIDs and in order to avoid electronic jitter between the two generators they are phased locked. This configuration allows us to apply continuous forces[2].

  The amplitude of the shaking for the two counter-propagating beams can be easily evaluated from the modulation amplitude $\Delta\nu_{max}$ of the frequency offset between the two lattice beams. For the sinusoidal case we have:

  $$\Delta\nu(t) = \Delta\nu_{max}\sin(\omega t) \rightarrow K_{sin} = m\omega\Delta\nu_{max}d_L^2 \tag{3.25}$$

  The argument of the zeroth order Bessel function $\mathcal{J}_0$ is

  $$K_{0,sin} = \frac{K_{sin}}{\hbar\omega} = \frac{\pi^2\Delta\nu_{max}}{2\omega_{\text{rec}}}. \tag{3.26}$$

[2]The initial velocity for Rabi oscillation (paragraph 2.5), the increasing frequency shift for calibration with Landau Zenner formula and experiments on Bloch oscillations presented in 4.19 used this configuration.

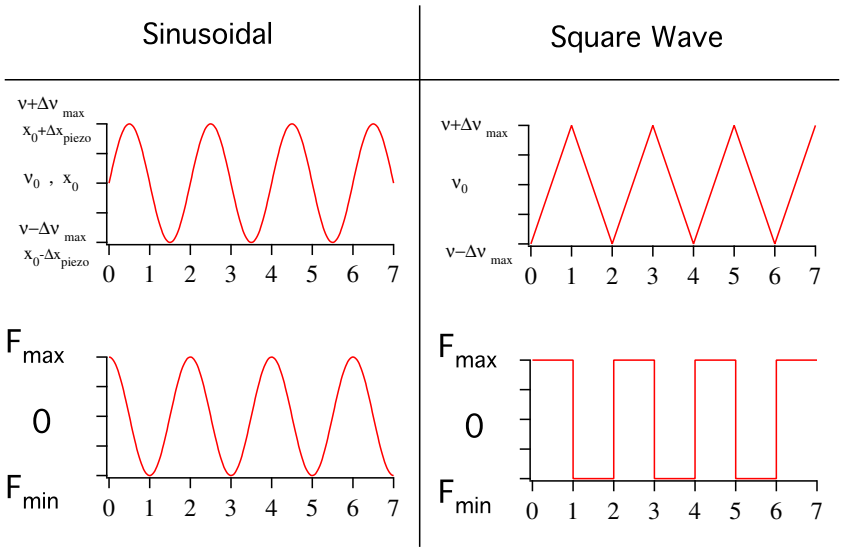

Figure 3.3: Time dependences of $\Delta\nu$ (by using frequency modulation) or Δx (by using a piezo-electric actuator) and the force F for the two different driving waves considered in paragraph 3.4.

which is independent of the frequency of the shaking. In order to realize a square wave dependence of the force, a triangular wave of the modulation frequency is used and we have

$$K_{sqr} = m\beta d_L^2 \tag{3.27}$$

where β is the slope of the triangular wave.

- **Retro-reflected beam**: a beam is focused on the atoms. After the passage through the cell the beam is re-collimated, back-reflected on itself with a mirror mounted on a piezoelectric actuator and refocused on the atoms using the same lens used for the collimation in the first passage. The piezo-electric actuators are driven by a function generator (Stanford DS345). The voltage applied to the actuator (as observed with an oscilloscope) is proportional to the expansion of the device and independent of frequency. This feature allows a real-time control of the shaking strength.

  For the retro-reflected configuration K can be evaluated directly from the spatial displacement Δx_{max} of the standing wave.

$$K_{0,sin} = \frac{\pi^2}{2}\frac{\Delta x_{max}}{d_L}\frac{\omega}{\omega_{\rm rec}}. \tag{3.28}$$

The movement Δx_{piezo} induced by the piezo actuator on the mirror shifts the phase of the retro-reflected beam by $2\pi\Delta x_{piezo}/d_L$. When the shift of the phase is $\pi/2$, the pattern on the atoms is shifted by one lattice constant and so:

$$2\Delta x_{piezo} = \frac{\Delta x_{max}}{2} \rightarrow K_0 = \frac{\pi^2}{2}\frac{4\Delta x_{piezo}}{d_L}\frac{\omega}{\omega_{\rm rec}}. \tag{3.29}$$

The piezo-electric devices used for the shaking were previously tested with an interferometric technique for different amplitudes and frequencies of the driving voltage with particular attention to possible mechanical resonances or thermal relaxations.

In the next paragraphs and chapters we will refer to the shaking strength only as K_0, as the difference between $K_{0,sin}$ and $K_{0,sqr}$ is only technical.

3.5 Dynamical control of Matter-Wave Tunneling

Signatures of tunneling suppression in time periodic driven systems have been observed in a number of experiments [53, 63, 49], and recently dynamical localization and coherent suppression of tunneling have been demonstrated using light propagating in coupled waveguide arrays [62, 22]. Prior to our work, however, an exact experimental realization of the Bose-Hubbard Hamiltonian with a time-periodic potential (3.9) had not been reported.

3.5.1 Sinusoidal Suppression

In situ observation

The experiment we performed was based on the idea of measuring the single atom tunneling rate by observing the behavior of the whole cloud inside the

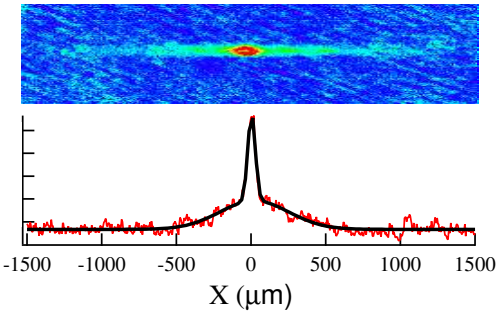

Figure 3.4: Typical *in situ* image of a cloud after expansion in a shaken optical lattice. The profile was fitted by a double gaussian. The time of expansion was 150 ms, the lattice V_0= 6 $E_{\rm rec}$, the shaking frequency $\omega/2\pi$= 1 kHz and $K_0 = 1.5$.

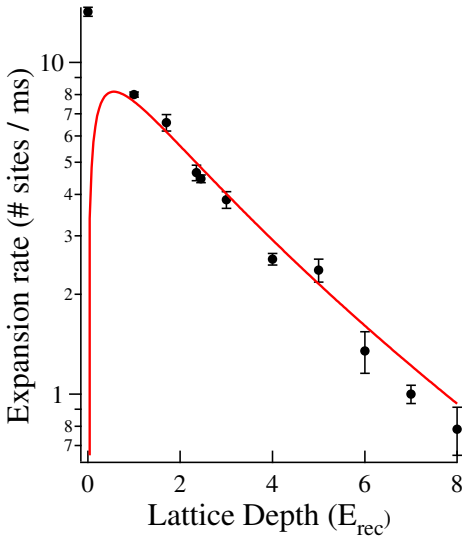

Figure 3.5: Expansion rate r as a function of the lattice depth. The expansion is measured in units of lattice constant d_L. The line is obtained from the theoretical prediction of equation 3.4: $r = Jd_L/\hbar$.

strongly driven periodic potential. After the creation of the BEC inside the dipolar trap, we left the atoms free to expand in one horizontal direction. This technique was performed by switching off one of the dipolar trap beams. The atoms inside the remaining beam were confined inside a quasi cylindrical potential as the radial frequency was around 100 Hz and the longitudinal one only 3 Hz, and hence negligible on the time scale of the experiments ($\sim$ 100ms)

The expansion rate r of the cloud is directly connected to the tunneling of the atoms inside the lattice. By measuring the width σ inside the dipolar trap beam after increasing expansion times a perfect correspondence between J of formula 3.4 and the expansion velocity of the cloud was observed (figure 3.5).

In order to measure the effect of the the sinusoidal shaking, the cloud was left to expand in the lattice for different combinations of frequency and amplitude of the shaking and lattice depth[3]. Figure 3.6 shows a few example of cloud after the expansion there are few examples clouds after the expansion.

The physical quantity that was observed in all the in situ measurements was the width of the condensate σ (see figure 3.4). When the lattice was not shaken, σ was measured by a single gaussian fit profile but when the lattice was shaken the central peak in the atom distribution was surrounded by a broader pedestal composed by atoms excited to upper bands. In order to avoid contributions to the fit from the pedestal, the cloud in the shaken

[3]The importance of the frequency and of the loading ramp of the shaking will be studied in more detail in the next chapter

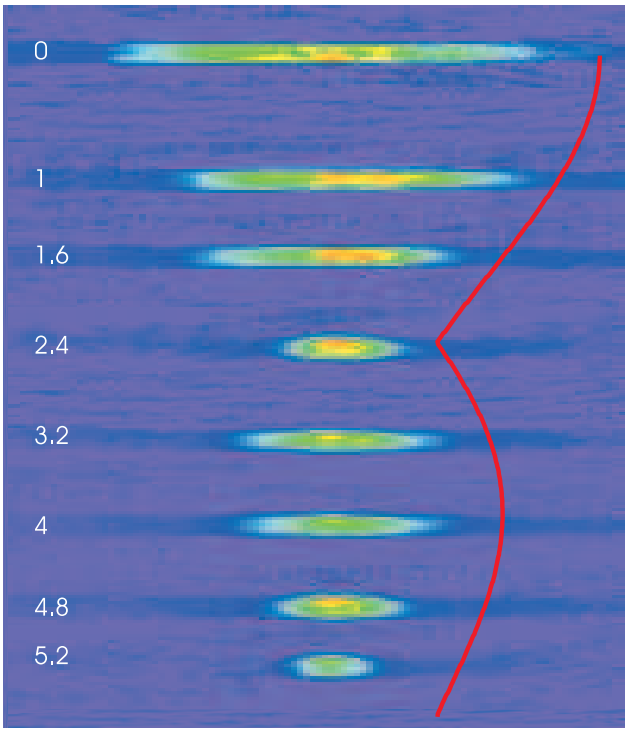

Figure 3.6: Example of cloud expansions for different values of K_0. The lattice depth is 9 $E_{\rm rec}$. The line follows the theoretical prediction of $J_{\rm eff}$.

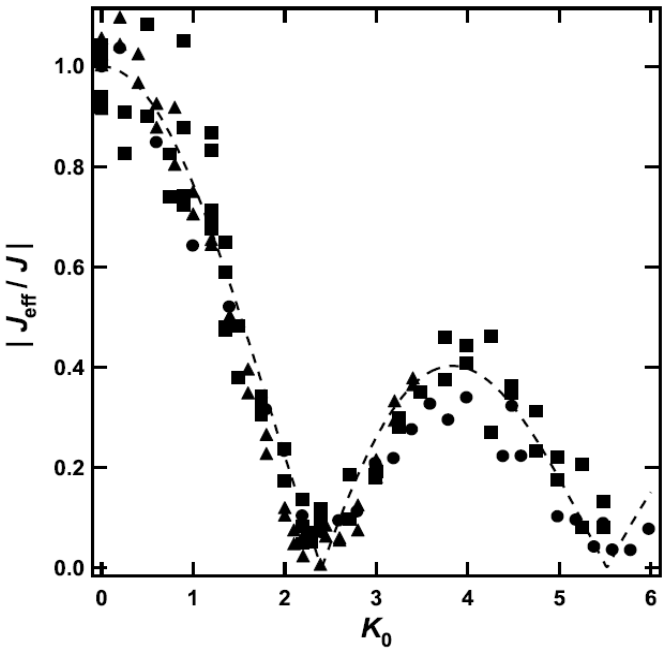

Figure 3.7: Measurement of the ratio $|J_{\rm eff}/J|$ for different values of K_0. The different shapes of the points correspond to different lattice depths and different frequencies of modulation at which the measurement was performed; •: V_0 = 6 $E_{\rm rec}$, $\omega/2\pi$= 0.5 kHz; ■: V_0 = 6 $E_{\rm rec}$, $\omega/2\pi$= 1 kHz; ▲: V_0= 4 $E_{\rm rec}$, $\omega/2\pi$= 1 kHz. The dashed line is the theoretical prediction.

regime was fitted with a double gaussians fit. As we will see in the next chapter, the parameters for an adiabatic driving of the system are very critical in the determination of how many atoms remain in the condensate fraction.

The ratio $|J_{\rm eff}/J|$ thus measured[4] is plotted in figure 3.7 and the agreement of the measurements with the theory is very good for all the combinations frequency-depth. This demonstrates that the theoretical approach of renormalization of the Hamiltonian succeeds in the prediction the hopping term $J_{\rm eff}$. The next step will be an extensive study of the coherence of the process.

Time of Flight measurements

The dynamical suppression of tunneling can be also studied in *time of flight* images (see profiles in Figure 3.8). The quantity obtained from the interference pattern is the visibility, which is defined as

$$\mathcal{V} = \frac{n_0 - n_{\pm p_{\rm rec}}}{n_0 + n_{\pm p_{\rm rec}}} \tag{3.30}$$

where $n_{\pm p_{\rm rec}}$ is the averaged values of the condensate density in a region of width equal to about 1/4 of the peak separation centered about the halfway point between the central peak and the side ones (see left profile in Figure 3.8) and n_0 is the density in the central peak. The visibility is a powerful tool for understanding how the phase between the different lattice sites is evolving

[4]Note that this measurement is only sensitive to the absolute value of $J_{\rm eff}$; later on we shall see how this sign of $J_{\rm eff}$ can be made visible.

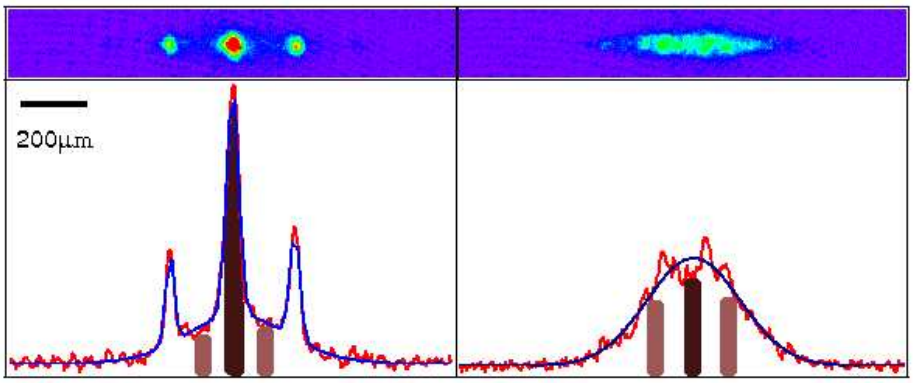

Figure 3.8: Two examples of interference patterns for $K_0 = 1$ (on the left) and $K_0 = 2.4$ (on the right) after 20 ms of holding time. The shaded areas on the pattern are used for the evaluation of the visibility.

for different values of J_{eff}. For a perfectly phase-coherent condensate, $\mathcal{V} = 1$, whereas for a strongly dephased condensate, $\mathcal{V} = 0$.

The phase evolution of the condensate has been measured by switching on the driving of the lattice without letting the cloud expands (both dipolar trap beams are maintained). After an increasing waiting time inside the shaken lattice, both the dipole trap and the lattice beam were switched off and the atoms detected after *t.o.f.* expansion. The temporal decay of the interference pattern visibility has been fitted with an exponential curve and the characteristic dephasing time τ_{depth} has been measured for different values of K_0. The results are plotted in figure 3.9.

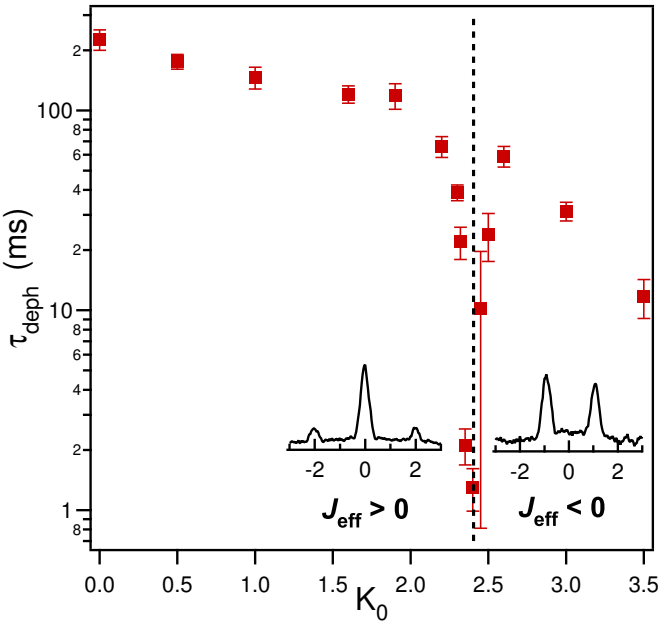

Figure 3.9: Measurement of the dephasing time τ_{depth} as a function of K_0. A clear dip is present at $K_0 = 2.4$, whose position is highlighted by the dashed line. The measurement was taken in a lattice with $V_0 = 9\ E_{\text{rec}}$ and with a shaking frequency $\omega/2\pi = 3$ kHz. *inset* Typical interference pattern in the regions where J_{eff} is positive and negative.

For value of the driving strength for which $J_{\text{eff}} = \mathcal{J}_0(K/\hbar\omega)J \neq 0$, the phase between neighbouring sites is preserved because the tunneling events between sites maintain the long-range coherence of the condensate. Approaching the zero of the Bessel function, the time of tunneling $(\hbar/J_{\text{eff}})$ becomes comparable with the time of the experiment. As the phases of the different lattice site evolve at a higher frequency due to inter-atomic colli-

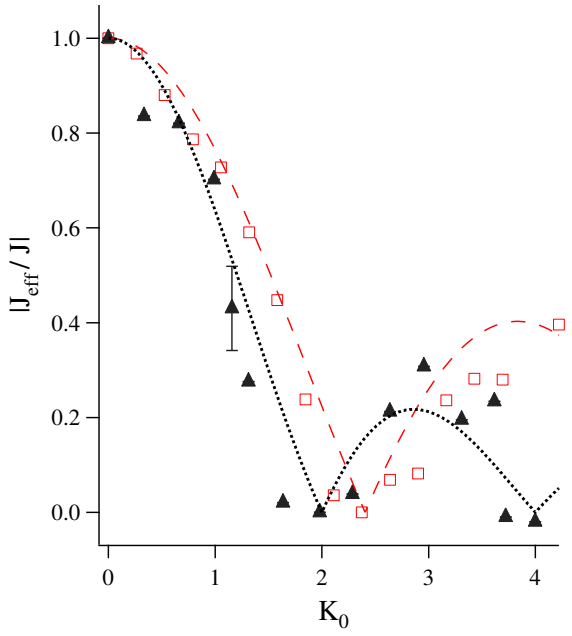

Figure 3.10: Measurement of the ratio —J_{eff}/J— for different values of K_0 for sinusoidal and square wave forcing. □: sinusoidal forcing $V_0 = 6\,E_{\text{rec}}$, $\omega/2\pi$= 1 kHz; ▲: square wave forcing, $V_0 = 6\ E_{\text{rec}}$, $\omega/2\pi = 1.5$ kHz. The dotted line is the |sinc| function, the dashed line is the $|\mathcal{J}_0|$.

sions and quantum fluctuations, an increasing dephasing between the phases of the sites takes place. In that case the interference pattern doesn't present peaks. The dephasing time far from the critical point K_0 is two orders of magnitude larger than the one measured at $K_{0,sin} = 2.4$.

In the range of values where J_{eff} is negative the interference pattern presents two peaks at $q = \pm p_{\text{rec}}$ (see insets of figure 3.9) as predicted from the dependence of the band shape from the sign of J. When the shaking is switched on at a value between 2.4 and 5.9, the atoms, in fact, occupy the new ground state at the edge of the Brillouin zone. In that region the dephasing time is shorter and the inverted interference pattern appeared only 4-5 ms after the switching on of the driving. In Chapter 4 we will see the possible explanations of this phenomena.

3.5.2 Exact dynamical localization

As seen in 3.3 the effective tunneling term depends also on the shape of the driving. The difference between the two types of driving can be studied with the two techniques explained in the previous paragraph [5].

The results presented in Figure 3.10 and 3.11 show a perfect agreement

[5] In order to have a sudden passage from a positive to a negative force, for this measurement we used only the two counter-propagating beams configuration avoiding deformations of the driving wave due to mechanical inertia of the piezo-electric device.

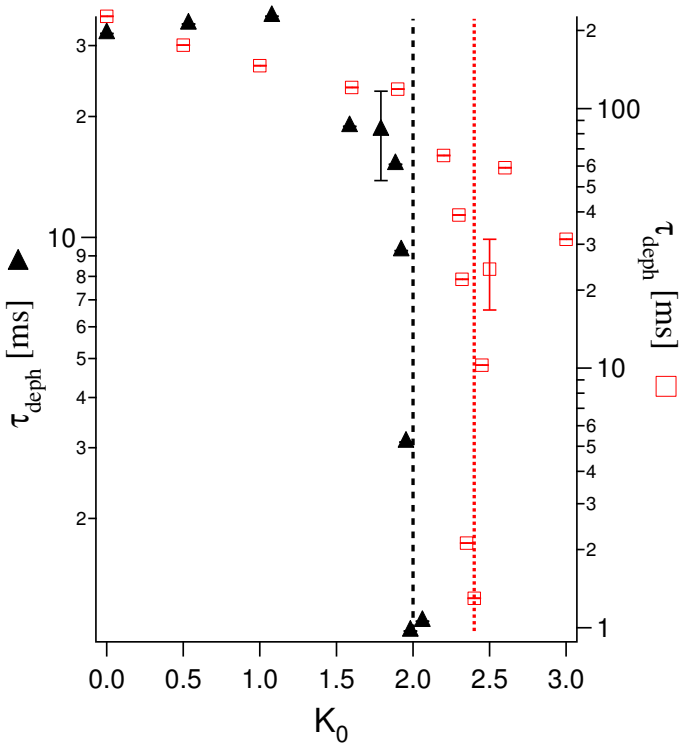

Figure 3.11: Measurement of the dephasing time τ_{depth} as a function of K_0. A clear dip is present at $K_0 = 2.4$ for the sinusoidal forcing (□: $V_0 = 9\,E_{\rm rec}$, $\omega/2\pi$= 3 kHz) and at $K_0 = 2$ for the square wave forcing (▲: $V_0 = 9\,E_{\rm rec}$, $\omega/2\pi$= 1.5 kHz).

with the theoretical prediction for the dependence $|J_{\rm eff}/J| = |\mathrm{sinc}(K_0)|$ in the case of square-wave forcing. In fact the most evident suppression of the expansion of the cloud takes place at the zero of the sinc function for the square wave forcing (K_0=2) and at the first zero of the zeroth-order Bessel function ($K_0 = 2.40$) for the sinusoidal square. As seen for figure 3.9 the value of K_0 where $J_{\rm eff}$ is zero is more precisely determined by looking at the lifetime of the interference pattern after *time of flight* expansion.

A more detailed measurement of the cloud expansion at the two different zeros ($K_0 = 2.4$ for the sinusoidal driving and $K_0 = 2$ for the square wave forcing) could quantify the contributions of next neighbour hopping terms. The capability to measure this effects resides in the lifetime of the condensate inside the lattice. The hopping term $J_2/\hbar$, in fact, is only some Hz also for shallow lattice and the time needed for a visible expansion is beyond experimental possibilities.

For the experiments presented in Chapter 4 and Chapter 6 the calibration of the driving strength was done by observing the interference patterns of a cloud released from a shaken lattice after a holding time. The very narrow dips shown 3.9 and 3.11 are a very stable and precise calibration references for K_0 especially when the piezo electric devices were used.

Chapter 4

Coherence and adiabaticity of dressed matter waves

The adiabaticity and the preservation of coherence are the two tasks required in order to transfer a Bose Einstein condensate into a driven regime without releasing energy into the system or introducing an uncontrolled dephasing. In this chapter I will explain the problem of the adiabatic following of the system under a time variation of the driving amplitude. In particular I will use numerical simulations done by A. Eckardt and M. Holthaus ([28, 29, 30]). Different tests were applied in order to find the range of parameters needed, and examples of adiabatic and coherent driving are shown for a one dimensional system.

4.1 Introduction to the problem

The adiabaticity of the periodic forcing of a system of atoms inside a periodic potential is related to the possibility of carrying the system from the undriven ground state characterized by the Bose-Hubbard parameters U and J to the driven one with parameters U and J_{eff} without releasing energy into the ensemble. In Chapter 2 we introduced the standard adiabatic theorem and we applied it to the loading of the atoms into the optical lattice. In that case, the duration of the ramp of the lattice depth could not be shorter than a certain value in order to avoid the excitation of the atoms from the ground state to the first (or higher) excited band. As in that case the problem was the mismatch between the free particle eigenstates and the Bloch eigenfunctions, for a driven system the shaking cannot be suddenly switched on because the Bloch bands are not eigenstates of the final Hamiltonian 3.9.

In comparison with the adiabatic theorem previously studied, in our sys-

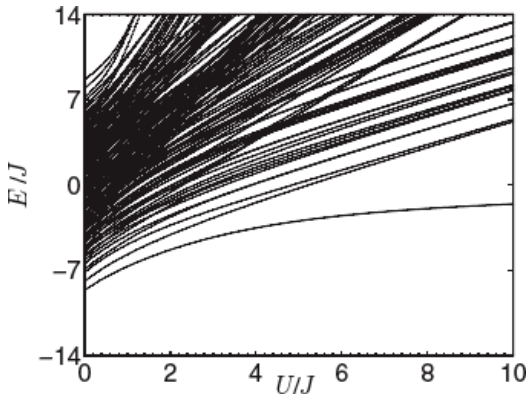

Figure 4.1: Spectrum of the energies E within the first Brillouin zone for a system of $N = 5$ atoms in $M = 5$ wells. From Ref. [30].

tem there are two time scales to take in consideration rather than just one. On one hand there is the slow time dependence on the parameter K_0, and on the other hand there is the time-periodicity of the Hamiltonian. The basic idea is to freeze the slow parameter leaving the fast one (the shaking) unaffected:

$$H^{K_0}(t) = H^{K_0}(t+T) \tag{4.1}$$

where T is the period of the shaking.

4.1.1 Adiacaticity in the Floquet spectrum

The first step for the understanding of the driven system is the analysis of a simple toy model. In the case of N atoms in M sites each state is a superposition of all the Fock states of i-atoms in the j state.

$$|\{n_j\}\rangle = |n_1\rangle \otimes |n_2\rangle \otimes, ..., |n_M\rangle, \qquad \sum_{j=1}^{M} n_j = N \tag{4.2}$$

Each state can be expressed as a superposition of all the possible combinations of the atoms in the sites and the energy spectrum of the undriven system can be numerically evaluated for a small system. For example the spectrum in figure 4.1 is obtained by using five atoms in five sites of a 1D lattice and by evaluating the energy of the different levels at an increasing value of U/J. The ground state of the system is the lowest level and the increasing distance from the upper levels is a first sign of the Mott-insulator that we will observe in the next chapter for the three-dimensional system.

The numerical calcuations for the driven system have to be done by taking into consideration the Floquet theory presented in paragraph 3.2.1. Within the Floquet theory in fact the eigenstates of the Hamiltonian are extended in a Hilbert space defined as an extension $\mathcal{R}\otimes\mathcal{T}$ of $\mathcal{R}$. The Schrödinger equation

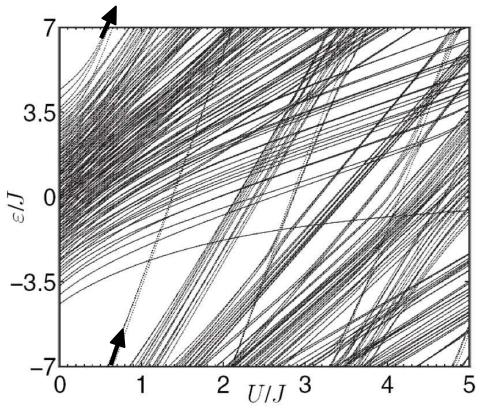

Figure 4.2: Spectrum of the quasienergies ϵ_n within the first Brillouin zone for a system of $N = 5$ atoms in $M = 5$ wells in a lattice shaken with $K_0 = 1.5$. The arrows help to follow the first folding of the highest energy level. From Ref. [30].

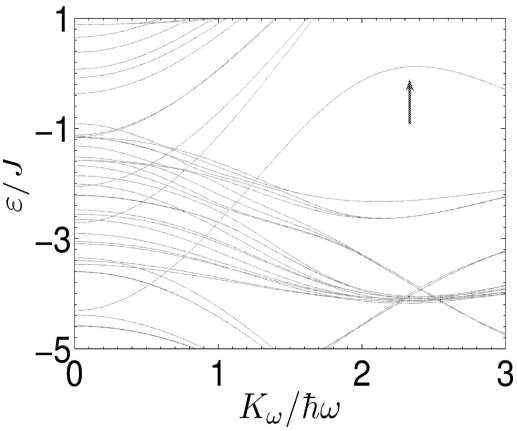

Figure 4.3: Spectrum of the quasienergies ϵ_n within the first Brillouin zone for a system of $N = 5$ atoms in $M = 5$ wells in a lattice shaken with $\hbar\omega = 16J$. The arrow in the spectrum marks the quasienergy of the Floquet state evolving adiabatically from the ground state of the undriven Bose Hubbard system. From Ref. [28].

is transfered to $\mathcal{R} \otimes \mathcal{T}$, solved and then projected again on $\mathcal{R}$. The resulting quasienergies $\epsilon_{n,m}$ are defined in a Brillouin-like spectrum of width $\hbar\omega$ as shown in Figure 4.2 .In a periodically driven potential, the Floquet states take a role that is analogous to the one played by usual energy eigenstates.

By comparing figure 4.2 with figure 4.1 it is evident how the driven spectrum is the result of the photons of energy $\hbar\omega$ coupling the different energy levels. High-energy levels at small values of U/J_{eff} leave the *Brillouin zone* and are folded back into it, reappearing at the bottom (see arrows in Fig. 4.2), crossing the other levels and of course also the ground state. This folding of the spectrum introduces a large number of avoided crossings. For the experiments we want to perform, the initial value U/J will be fixed and the amplitude of the driving will be ramped from 0 to a final value. The energy spectrum for this purpose is shown in figure 4.3 as a function of K_0. The presence of avoided crossings is still evident, and we will discuss in the next paragraph how the passage of one of these can be analyzed.

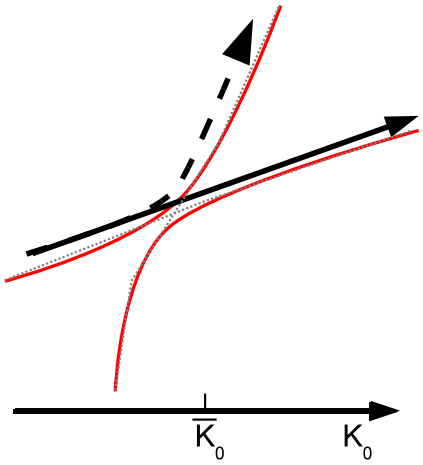

Figure 4.4: Different trajectories that the system can experience when passing through an avoided energy crossing. The dotted lines are the two states in $\mathcal{R}$ and the continuos ones are the resulting levels with the avoided crossing The solid arrow corresponds to the diabatic trajectory ($r = 1$), the dashed one to the adiabatic trajectory ($r = 0$).

4.1.2 The avoided crossing

The problem of an adiabatic transfer in a driven state is strictly connected to the capability to cross the avoided crossings. If this system is initially prepared in its ground state at $K_0 = 0$ and then K_0 is increased to some value $K_0^{(max)}$, during its trajectory the energy level experiences many energy avoided crossings with other levels. For each of these crossings the tunneling rate r through the energy gap can be evaluated by using Landau-Zener theory. This tunneling rate has an exponential form

$$r = e^{-const\frac{\Delta^2}{vel}} \tag{4.3}$$

that depends on the square of the gap size Δ and inversely on $vel = dK_0/dt$.

Three regimes can be considered for a generic crossing at $\overline{K}_0$(see Fig.(4.4)):

- adiabatic following: the system follows an adiabatic trajectory (dashed arrow), i.e., no tunneling occurs ($r = 0$). The system follows the upper energy level by changing its state in $\mathcal{R}$ space;

- crossing regime: tunneling rate is $0 < r < 1$ and the state of the system becomes a coherent superposition of the two crossing states in $\mathcal{R}$. In this particular case the evolution of the system could be not reversible. The two states in the two different levels evolve separately and i.e. if the parameter K_0 is changed back to its initial value the initial state could not be recovered.

- diabatic passage: the system passes the gap (continuous arrow), i.e. total tunneling occurs ($r = 0$). This is the case when the system

maintains its state in $\mathcal{R}$ following the ground level of the undriven spectrum till the regime with U and J_{eff}. This is the situation we want to realize experimentally.

To find the range of parameters that differentiates these three regimes is the key for controlling the system. Notice that in the following of this thesis a **diabatic passage** through every avoided crossing will be denoted as an **adiabatic following** of the system from the static regime to the driven one.

4.2 The experimental procedure

Both the adiabaticity and the coherence of the external driving can be verified by using the absorption image of the atoms after time of flight. Even if the release of energy into the ensemble can be quantified by a larger width of the cloud also in *in situ* images, the width of the momentum distribution after *time of flight* expansion is a more direct measurement of the energy of the cloud. For a pure condensate, by using a time of flight of $\sim 23\,\text{ms}$, the width of the cloud is around 35 μm ($\sim$ 10 pixels), to be compared with the *in situ* value of 10 μm ($\sim$ 3 pixels) which is close to the diffraction limit of our detection system. Moreover *time of flight* images contains information about the phase. The interference pattern is, in fact, the result of a determined phase between lattice site. A loss of visibility of the interference pattern is a clear sign that there are different time evolutions in each site or excitations of the system to upper levels. For this reason the use of *time of flight* pictures allows to check not only the energy but also possible loss of coherence of the condensate.

The procedure we used to quantify the adiabaticity of the driving is shown in Figure 4.5:

- the lattice depth is ramped to the final value V_0 with an exponential ramp of characteristic time τ
- the driving amplitude is ramped up in a time $t_{ramp}^{shaking}$ to the value K_0^{test}, while the lattice depth is maintained constant
- the driving amplitude is maintained at K_0^{test} for $\Delta t^{shaking}$;
- the driving amplitude is ramped down to zero in $t_{ramp}^{shaking}$;
- the lattice is adiabatically ramped down to a shallow lattice ($4E_{\text{rec}}$) in 15 ms;

- the atoms are held in the shallow lattice for 10 ms on order to have a good thermalization if the the energy was not uniformly release inside the whole cloud;
- the lattice is abruptly switched off.

For all the experiments done in the one-dimensional systems, the dipolar trap was maintained at the value used for the achievement of pure condensates ($\omega_x = \omega_y$= 68 Hz and ω_z= 96 Hz).

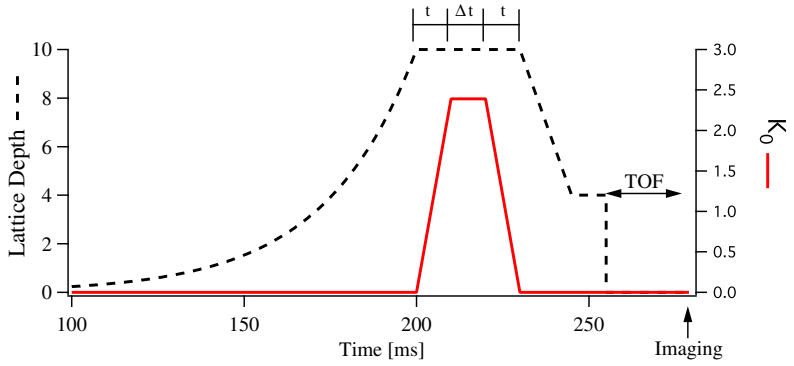

Figure 4.5: After the loading of the condensate in the optical lattice of depth V_0, the driving is linearly ramped to the final value in $t_{ramp}^{shaking}$, held for $\Delta t^{shaking}$ and ramped linearly down in $t_{ramp}^{shaking}$. Then the lattice is ramped down in 15 ms at 4 $E_{\rm rec}$ and held at that value for 10ms for the thermalization of the ensemble.

In order not to mix different atomic responses, the parameters of the exponential ramp were optimized without driving as explained in 2.4.3. For the one dimensional system, we found that $L = 200\,\text{ms}$ with τ_{ramp} of 7 ms was the optimal parameters.

The integrated profile of a typical cloud after *t.o.f.* was characterized by a bimodal distribution (Figure 4.6). The condensate part of the atoms are in the narrow cloud. The wider background contains the atoms lost from the condensate as they aquire energy or a different phase. Since we released the atoms from the optical lattice, side peaks are present and allow us to measure the depth of the lattice (as seen in Chapter 2) and evaluate U (Eq. 3.4). For the characterization of the cloud we fit the central peak with a single gaussian evaluating the FHWM σ of the distribution as done in [82]. This fit permits, in fact, to be less sensitive to the shape of the profile. In order to compare this fit method and the visibility introduced in paragraph 3.5.1, we measured the lifetime of an interference pattern and the characteristic time

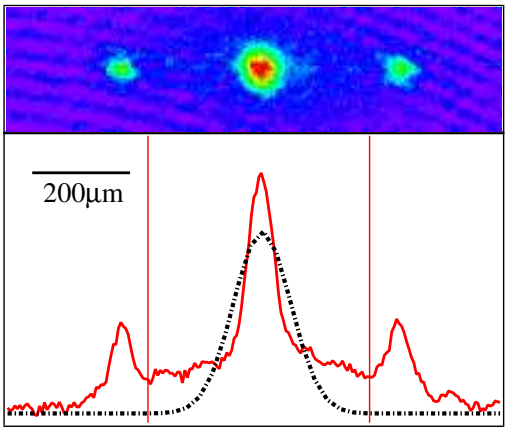

Figure 4.6: Typical *time of flight* picture with corresponding integrated profile (*thick line*). The fit (*dashed line*) is done within the thin vertical line, fixing the base at 0.

of the enlargement of the width of a condensate held for a variable time inside a deep lattice. These two times were equal and this result confirms how the width of the simple single gaussian fit is a good quantity for characterized the interference pattern.

4.3 The ramp time for the driving

The time needed to ramp the amplitude of the driving from zero to the final value K_0^{test} determines the quantity *vel* introduced in equation 4.3 and so it is a critical parameter to set. We notice that in comparison with the adiabaticity studied for the loading in the stationary lattice, a long ramp causes the state to follow the adiabatic trajectory that carries the system to higher energies and far from the ground state characterized by U and J_{eff}. As for the depth of the lattice, a too short ramp excites the system to higher bands and a sudden switching simply projects the state on a superposition of the eigenstates of the driven state.

We initially performed our test procedure with $\omega/2\pi = 3\,\text{kHz}$ and $K_0^{test} = 2.3$ corresponding to $J_{\text{eff}}/J \sim 0.06$. In Figure 4.7 the ratio between the undriven cloud width (σ_0) and the driven one (σ) for different lattice depths and ramping times $t_{ramp}^{shaking}$ is shown. A ratio of $\sigma_0/\sigma = 1$ (black region) corresponds to a perfect adiabaticity of the shaking, while smaller values (grey scale and white regions) indicate that the system was excited during the ramp.

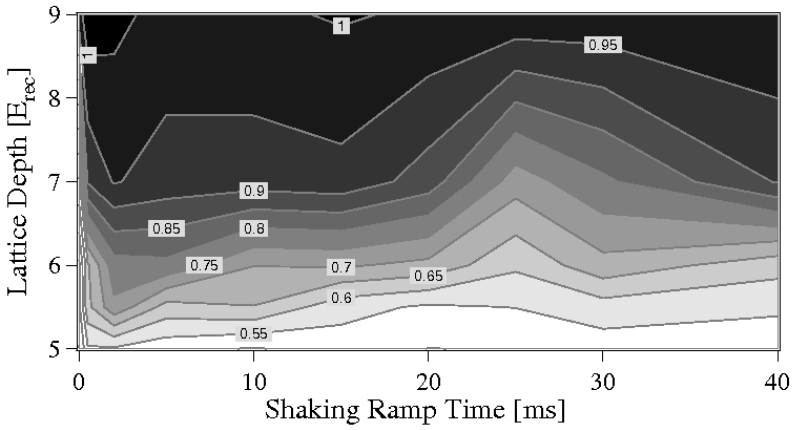

Figure 4.7: Contour plot of the ratio σ_0/σ varying lattice depth and ramp time $t_{ramp}^{shaking}$. The driving frequency is 3 kHz with $K_0^{test} = 2.3$.

It is evident that at a fixed depth the ideal range of $t_{ramp}^{shaking}$ is between 2 and 20 ms and that a better adiabaticity can be obtained for deeper lattices. For larger lattice depths, in fact, the distance between levels in the energy spectrum increases (see figure 4.1) and the consequence on the spectrum of figure 4.2 is a smaller density of avoided crossings. These observations also explain the good results for the coherence of the shaken system of figure 3.9 obtained with a lattice depth of $9E_{\rm rec}$ and sudden switch on, condition corresponding to the left corner on the top of figure 4.7.

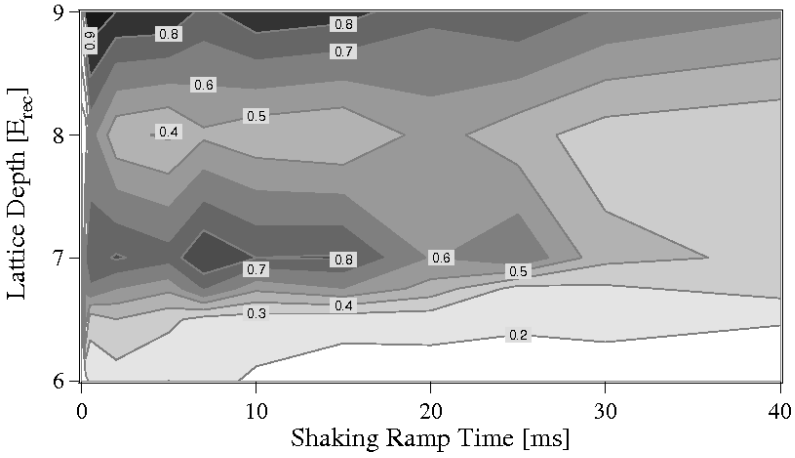

Figure 4.8: Contour plot of the ratio σ_0/σ varying lattice depth and ramp time $t_{ramp}^{shaking}$. The driving frequency is 6 kHz with $K_0^{test} = 2.3$.

We performed the same test at 6 kHz. For this frequency the range of ramp times where the driving control is most adiabatic is again between 2 and 20 ms. In this case it is evident that the problem is not simply linear and in fact, at a lattice depth of 8 E_{rec} there is a region where adiabaticity is more critical. Moreover the absolute value of σ_0/σ is always smaller than the one observed with a driving frequency of 3 kHz. In the next paragraph we will study the details related to the frequency choice.

4.4 The optimal frequency

The frequency of the driving is an important parameter. The expected upper limit for the frequency is related to the presence of a higher energy band in the undriven system (the theoretical calculations take in account only the fundamental band). For a lattice depth of V_0, at the center of the Brillouin zone the band gap between the ground state band and the first excited one is approximately 4 E_{rec}. At the edge of the Brillouin zone this gap is instead $V_0/2$. For the lattice depth 5.75 E_{rec} used for data in Figure 4.9, these gaps corresponds to frequencies of 12.8 and 9.0 kHz.

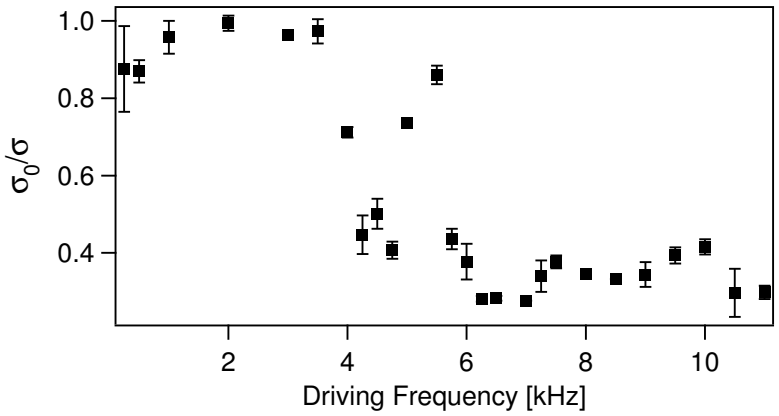

Figure 4.9: Ratio σ_0/σ for driving at 5.75 E_{rec} with $K_0^{test} = 2.3$. Ramp time is 10 ms, $\Delta t^{shaking} = 2$ ms.

In Figure 4.9 we performed our procedure using a ramp time of 10 ms and a waiting time $\Delta t^{shaking}$ of 2 ms, scanning the driving frequency from 250 Hz to 11 kHz. Even if in the data the presence of an upper limit is evident, the complexity of the spectrum suggests that the simple considerations on the limiting frequencies are not enough in order to determine the requested condition for adiabaticity. Our considerations about the Landau

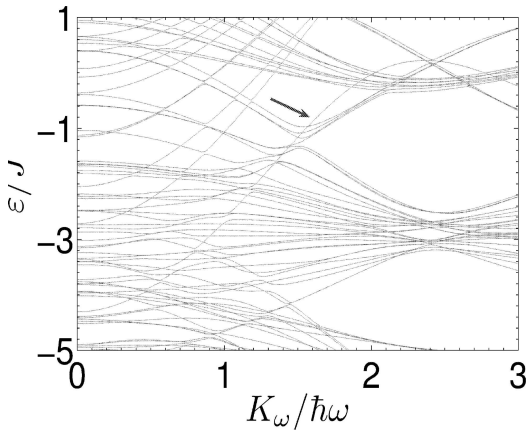

Figure 4.10: Spectrum of the quasienergies ϵ_n within the first Brillouin zone for a system of $N = 5$ atoms in $M = 5$ wells in a lattice shaken with $\hbar\omega = 12J$. The arrow in the spectrum mark the quasienergy of the Floquet state evolving adiabatically from the ground state of the undriven Bose Hubbard system. From Ref. [28].

Zener tunneling events in the Floquet spectrum were based on the continuos variation of the parameter K_0 and the possibility to determine its derivative. This requires an infinitely small variation of K_0 for each driving cycle. This condition cannot be applied in the experiments because in that case as the consequent ramp should be so slow that the system would follow the adiabatic trajectory. Moreover the experimental realization has to be done in a finite time. In the realistic case of a finite number n of shaking cycles, the ramp of the driving can be considered as a step-by-step path in the energy spectrum where each step (= driving cycle) introduces an increase K_0^{max}/n of K_0; the position and the density of the avoided crossing become critical for preserving the adiabaticity of the driving ramp. However the Figure 4.9 shows that for frequencies lower than 4 kHz and in a small interval around 5 kHz the abiabaticity of the driving is preserved.

On the contrary the limit for small driving frequencies is related to the folding of the energy spectrum. If a small frequency ω is used, the Brillouin-like zone becomes narrower and the density of avoided crossings in the quasi-energy spectrum increases. If the conditions $\hbar\omega/J$ and $\hbar\omega/U \gg 1$ are satisfied, they guarantee that these avoided crossings are sufficiently small. If this condition is not met, a multitude of large avoided crossings appears in the spectrum[1]. For a better understanding, it is useful to examine the energy spectrum on Figure 4.2 as a function of the amplitude K_0 for two different values of the driving frequency. Figure 4.10 shows part of the energy spectra obtained from simulations with $\hbar\omega = 12J$ and it has to be compared with simulations in figure 4.3 obtained with $\hbar\omega = 16J$. It is evident how the density and the size of the avoided crossings dramatically increases for

[1]The request on the value $\hbar\omega/J$ can be also interpreted as the number of driving cycles that the system needs in order to be dressed during the time of a tunneling event ($T \ll 1/J$).

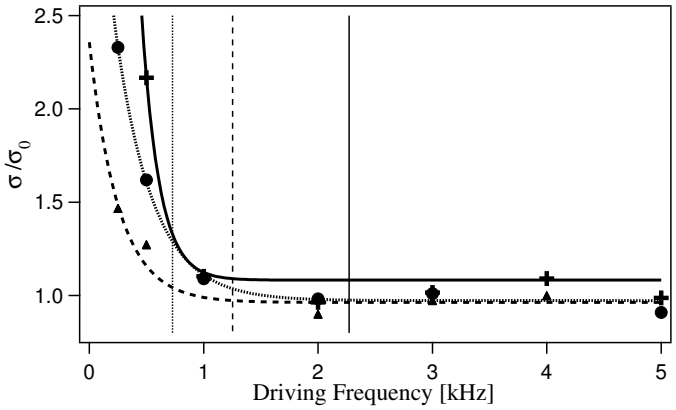

Figure 4.11: Ratio σ/σ_0 with $K_0^{test} = 2.3$ and 10 cycles of driving for each frequency. The depths are 4 (+), 6 (▲) and 8 E_{rec} (•). Exponential fit of the experimental data are represented by the dashed and continuous lines. The vertical lines are the limit $\omega/2\pi = J/h$ respectively at 2.27, 1.25 and 0.7 kHz.

a lower frequency. Incomplete Landau-Zener transitions lead to significant population in multiple Floquet states and an adiabatic return to the initial state is impossible. Numerical simulations of Ref. [28] suggest the condition $\hbar\omega/J > 6$, which corresponds to $\omega/2\pi > 1.3\,\mathrm{kHz}$ for the 5.75 E_{rec} lattice depth used in 4.9. This limit for low frequency is not evident in figure 4.9 but by performing the procedure with a constant number of cycles, therefore fixing the holding time, the limit is more evident (figure 4.11) even if it's less restrictive than the expected one and also nearly independent of the lattice depth. This result underlines how the behavior of a larger driven system has peculiar characteristics not predictable from the simulation with small number of atoms.

4.5 Limits for the starting depth

As seen in the previous paragraph, the problem of adiabaticity is quite complex and the choice of the different parameters (ramp time, frequency and depth) is critical. As we already saw searching for the optimal shaking frequency, the lattice depth is critical. In the energy spectrum of the undriven system (figure 4.1) the distance between levels is proportional to the lattice depth. Thus in a deep lattice it is more energetically consuming to excite the an atom to a neighbouring site already occupied. The increased distance between two levels induces a different position and distribution of the avoided

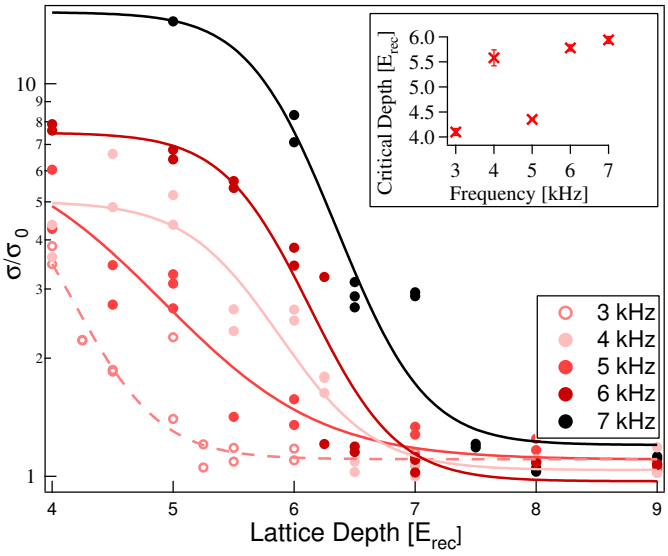

Figure 4.12: Ratio σ/σ_0 with $K_0^{test} = 2.3$ with ramp time $t_{ramp}^{shaking}$ of 10 ms and $\Delta t^{shaking}$ 2 ms. *Inset*: limit of lattice depth as a function of driving frequency.

crossings in the energy spectrum and in general a deeper lattice should be a better choice. It's interesting in this case to study which is the behavior of the system when the frequency of the driving is fixed and we scan the lattice depth. In Figure 4.12 the ratios σ/σ_0 for five different values of the frequency are plotted.

At lower lattice depths, the system considerably increases its energy. As already observed in figure 4.7, there is no clear dependence on the shaking frequency. Evaluating the critical depth by using a sigmoidal fit, the limits of the depth as a function of the frequency (insert of Figure 4.12) are in good agreement with Figure 4.9 and confirm the connection between critical depth and optimal frequency.

4.6 Intermediate Conclusions

The results of the previous paragraphs can be summarized as follows:

- **ideal ramp time** $t_{ramp}^{shaking}$: between 2 and 20 ms
- **frequency and depth**: between 1 and 3 kHz but starting from a lattice depth higher than $\sim 6\ E_{\rm rec}$

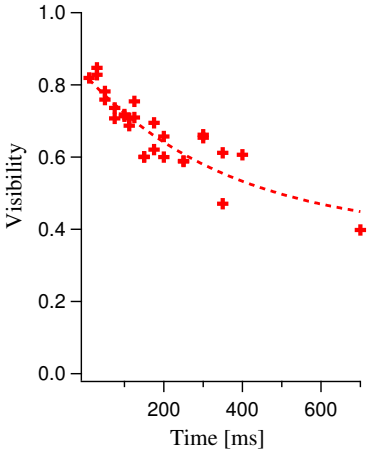

Figure 4.13: Visibility of the interference pattern for a lattice driven at $15\,E_{\rm rec}$, 3 kHz and $K_0^{test} = 2.3$ as a function of holding time $\Delta t^{shaking}$. The ramping up and down of the driving is done in 10 ms. The resulting life time is 370 ms.

As an example of good adiabatic driving of the lattice, we measured the lifetime of the interference pattern observed at the end of the procedure of Section 4.5 for a lattice of 15 $E_{\rm rec}$, driven at 3 kHz and $K_0^{test} = 2.3$. The astounding result is that in this configuration with an J decreased to 0.06 times the original one ($\mathcal{J}_0(2.3) = 0.0555$), the lifetime in the driven regime reaches the value of 370 ms.

4.7 Applying the adiabaticity

The results of the previous paragraphs open the possibility of adiabatically carrying the condensate into a driven regimes and to use the single Floquet states to represent them. In the following paragraphs I'll show some applications and perspectives of this result.

4.7.1 Single Floquet State occupation

An interesting theoretical observation about Floquet states regards the momentum distribution of the wavepacket. As we saw in Section 3.3 on the shaken lattices, the Hamiltonian is obtained from Bose-Hubbard model by replacing the matrix element J with the corresponding $J_{\rm eff}$ but the Fourier transform of the single particle density matrix is the same in both cases. Hence, even though the position of the lattice is periodically shifted, the position of the interference peaks observed in the laboratory frame does not move. By looking at the system after an integer number of driving cycles ($T = 2n\pi/\omega$), as we did in previous tests, the interference pattern is symmetric with respect to the center. On the other hand on a time scale shorter than

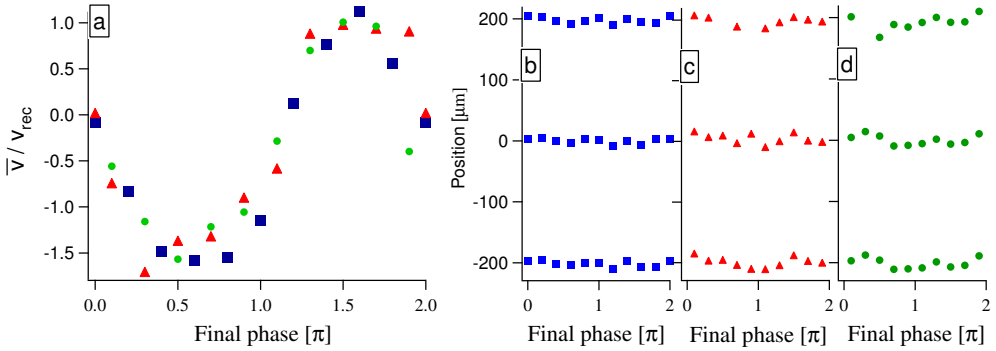

Figure 4.14: **a**. Mean velocity calculated from the interference pattern of a lattice driven at 9 $E_{\rm rec}$, 1 kHz and $K_0^{test} = 1.85$ as a function of the final phase of the driving. The ramping up is done in 10 ms and holding time is 10 ms. Different symbols correspond to different initial phases: ■ 0, ▲ $\pi/2$ and ● $-\pi/2$. **b**, **c** and **d**. Peak positions for the three different initial phases as a function of final phase.

the cycle period one expects that in *time of flight* images, the center of the envelope of the different peaks oscillates due to the time evolution introduced by the energy term of equation 3.8. The result may be tested by varying the phase of that time evolution and we performed the measurement for an optical lattice of depth 9 $E_{\rm rec}$ driven at 1 kHz and $K_0 = 1.85$ ($J_{\rm eff}/J$=0.31). The sampling time was 100 μs and we used three different initial phases of the driving as the realized Floquet states should not discriminate between *sinusoidal* or *co-sinusoidal* periodic perturbations.

The envelope oscillation has been quantified by measuring the periodic modulation of the height of the two side peaks expressed as a mean velocity of the cloud measured in unit of $v_{\rm rec}$ (graph **a** in figure 4.14). If $f(x)$ is the velocity spectrum obtained from the vertically integrated picture (see figure 4.14), $\bar{v}/v_{\rm rec}$ is $\frac{constant}{v_{\rm rec}} \times \int x f(x) dx$ where *constant* contains the conversion between the distance and $v_{\rm rec}$ derived by the *t.o.f.* measurement.

Graphs **b**, **c** and **d** show the stationarity of the positions of the peaks of the interference pattern. A slight residual time dependence of the peaks positions might be due to effects beyond the high frequency approximation of Floquet theory.

4.7.2 U_{eff}/U vs $|J_{\text{eff}}|/J$

We saw in Chapter 2 how the lattice depth (and U by using Eq. 3.4) can be evaluated (Eq. 2.47) from the relative populations of the side peaks of the interference pattern of figure 4.6. The possibility of loading the condensate into a lattice with a determined U and adiabatically suppressing the tunneling J with the driving allows us to perform a different kind of measurement. In fact if J_{eff} is small enough (and consequently the tunneling time is larger) quantum fluctuations cause the local phases on each sites evolve separately and the long range coherence of the condensate is lost. In this case the profile of the cloud after the *t.o.f.* expansion can be considered as the incoherent sum of the fundamental states of the harmonic potential of the single states and the value of U can be extracted from the width of the condensate.

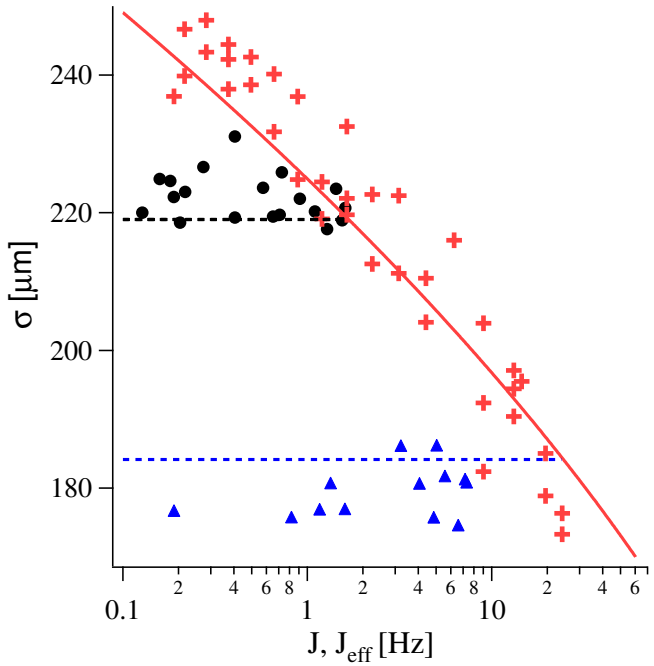

Figure 4.15: Width of the dephased cloud after 23.3ms of *t.o.f.* for a lattice driven at 3 kHz with 15 E_{rec} (▲) and 30 E_{rec} (•) as a function of J_{eff}. The shaking is ramped up in 20 ms with a holding time of 5 ms. The + are obtained scanning the lattice depth without shaking. The continuos line corresponds to the predicted width for the clouds released from an undriven lattice of variable depth. The dashed lines indicate the widths predicted for the lattice depth 15 and 30 E_{rec} in the undriven system.

Using equations 2.46 with 3.5, the following connection between the exten-

sion of the wavepacket at a single site and the on-site energy U is obviously,

$$U = \sqrt{8}\,\pi^{1/4} a_s E_{\rm rec}/\sigma_h. \tag{4.4}$$

This connection allows us to verify that U is not modified by the lattice shaking. The extension of the cloud was determined when we ramped up K_0 to the final value in 20 ms and, after a waiting time of 5 ms, switched off the lattice and the driving together. We performed a scan of the optical lattice depth V_0 between 15 and 30 $E_{\rm rec}$, and we scanned the lattice depth also without shaking. Figure 4.15 shows the width of the cloud released from a driven lattice for two different starting depths and from the undriven lattice. The horizontal axes reports the tunneling energy $J_{\rm eff}$ and J respectively. The continuous line corresponds to the predicted width for the clouds released from an undriven lattice of variable depth. The dashed lines are the widths predicted for the lattice depths 15 and 30 $E_{\rm rec}$. For increasing lattice depth whence decreasing J, the size of the cloud increases. For a driven lattice, on the other hand, the width remains constant in a range of $J_{\rm eff}$ of almost 3 orders of magnitude down to 0.1 Hz, corresponding to an equivalent lattice depth of 50 $E_{\rm rec}$. This observation confirms that the renormalization of Floquet theory regards only the parameter J and there is no modification of U. This allows us to define an effective potential $V_{\rm eff}$ whose B.H. parameters are U and $J_{\rm eff}$.

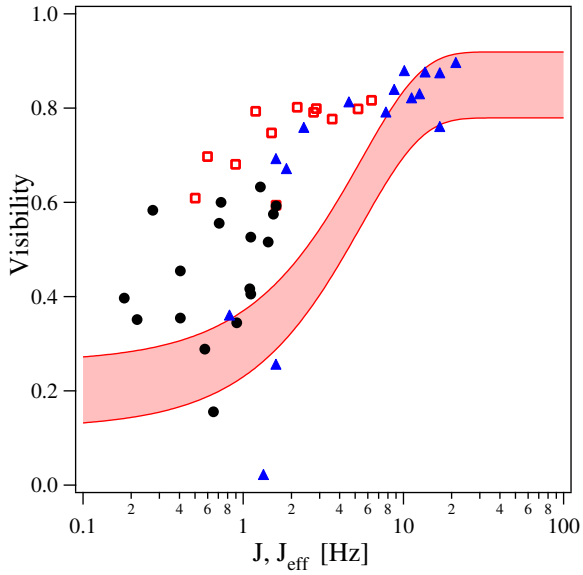

Figure 4.16: Visibility of the interference pattern for a lattice driven at 3 kHz with 15 $E_{\rm rec}$ (▲), 20 $E_{\rm rec}$ (□) and 30 $E_{\rm rec}$ (●) as a function of $J_{\rm eff}$ or J. The shaking ramping up is done in 20 ms with a holding time of 5 ms. The shaded area is a fit of the visibility obtained with different lattice depths without shaking and its thickness takes into account the statistical error of the data.

The adiabatic suppression of tunneling can also be used for the observation of number squeezed states ([69]) in shallow lattices. The reduction of the

tunneling rate between adjacent wells can also be viewed as a reduction of the number fluctuations at each lattice site. Quantum mechanically, this implies that the phase variance has to increase following the Heisemberg indetermination principle, and this behavior should be observed as a loss of coherence in the interference pattern. We measured and compared the visibility of the undriven and driven regimes. In figure 4.16 the data obtained for 15, 20 and 30 E_{rec} lattice depths are shown.

4.7.3 1D Mott Insulator

These results suggested the possibility to realize a Mott insulator phase of a one dimensional array of lattice sites with large number of atoms for each site. For a condensate confined in a one dimensional lattice, the Mott insulator regime can be reached for value of U/J which depends on the number n of atoms per site ([84]):

$$U/J_{crit}^{1D}(n) = 2(2n + 1 + 2\sqrt{(}n(n+1))) \tag{4.5}$$

For a small condensate with an extension of ∼100 sites and 10.000 atoms, the critical U/J_{crit}^{1D} is ∼400. If we consider to obtain a 1D Mott insulator by using a starting lattice depth of 30 E_{rec}, from equations 3.4 we have that U is 10 Hz. The value of J that we can reach in a driven regime is indefinitely small. Starting from 30 E_{rec} this means that the driving amplitude we need for reaching the critical value of U/J_{eff} is $K_0 = 2.38$ corresponding to a factor 60 of suppression of the tunneling (the equivalent lattice depth is 61 E_{rec}). The duration of an adiabatic ramp in this regime is critical as the time scale of tunneling approaching $K_0 = 2.39$ reaches several seconds, which is too long for the lifetime of a condensate in a deep optical lattice. Moreover the realization of this regime is technically complex as the strong dependence of J_{eff} on K_0 close to the zero of the Bessel function implies that the amplitude of the driving has to be very stable in time.

4.7.4 The passage to negative J_{eff}

In previous paragraphs we saw how the system can be transfered into a regime characterized by a smaller tunneling rate. This represents an important result even if the suppression of tunneling can be induced also using a larger lattice depth. An interesting regime that can be achieved only by adding a periodic driving is when the hopping term J_{eff} becomes negative. In this case the change of sign of J_{eff} induces a ground state band with inverted curvature, which means that the state with the lowest energy is characterized by atoms

with momenta $\pm p_{\rm rec}$ at the edge of the *Brillouin zone*. We studied these regimes by linearly ramping up and down K_0 in the region of negative $J_{\rm eff}$. Figure 4.17 shows such a cycle of the driving parameter K_0 as a function of time. After loading a BEC into the lattice ($V_0 = 18\,E_{\rm rec}$), K_0 was linearly increased from 0 to a final value $K_0^{max} = 2.7$ in 113 ms and back to 0 in the same time. The driving frequency was chosen as 6 kHz, so the full cycle contained 1356 driving periods. The resulting interference pattern created by atoms originating from different lattice wells consisted of well defined peaks when the condensate was phase coherent over the entire lattice, whereas when phase coherence was lost because of fluctuations, a broader and featureless pattern was observed.

Figure 4.17 clearly shows that in regions where the effective tunneling parameter $J_{\rm eff}$ is large and hence $U/J_{\rm eff} \ll 1$, the condensate remains phase coherent for several tens of milliseconds in spite of the strong driving. The appearance of a stable, well-defined interference pattern in the presence of strong driving proves that the BEC occupies a single Floquet state of the driven system and adiabatically follows that state as the driving parameter K_0 is varied. We have again confirmed that while $J_{\rm eff}$ changes as K_0 is varied, the effective interaction parameter $U_{\rm eff}$ remains constant (see the inset of fig. 4.17, where $U_{\rm eff}$ was normalized to the interaction parameter U in the undriven lattice). For $K_0 < 2.4$ the condensate occupies a Floquet state with quasimomentum $q = 0$ at the center of the Brillouin zone as reflected by an interference pattern with a dominant peak at zero momentum and two smaller sidepeaks at $2p_{\rm rec}$. When $K_0 = 2.4$ and $J_{\rm eff} = 0$ neighboring wells of the lattice are almost completely isolated on the timescale of the experiment and hence phase coherence is lost due to increased quantum phase fluctuations in the number squeezed states owing to $U/|J_{\rm eff|} \gg 1$. For $K_0 > 2.4$ the interference pattern changes shape and two peaks at $\pm p_{\rm rec}$ appear, clear features of the ground state of the system characterized by a negative $J_{\rm eff}$. The experimental observation of an interference pattern almost perfectly restored when K_0 is reduced back to 0 at the end of the cycle confirms that the driving didn't release energy into the system and that the coherence of the ensemble is preserved[2]. This can be considered as a clear sign that the condensate always remained in the Floquet state of lowest mean energy.

The transition to the inverted band regime is not yet theoretically explained. As the time tunneling time between sites is $h/J_{\rm eff}$, the closer the system is to $J_{\rm eff} = 0$, the longer is the time needed for the system to adi-

[2]The residual noise present in the interference pattern at the end of the cycle is compatible with the observed lifetime of the condensate held for more than 226 ms in an undriven lattice with a depth of 15 $E_{\rm rec}$.

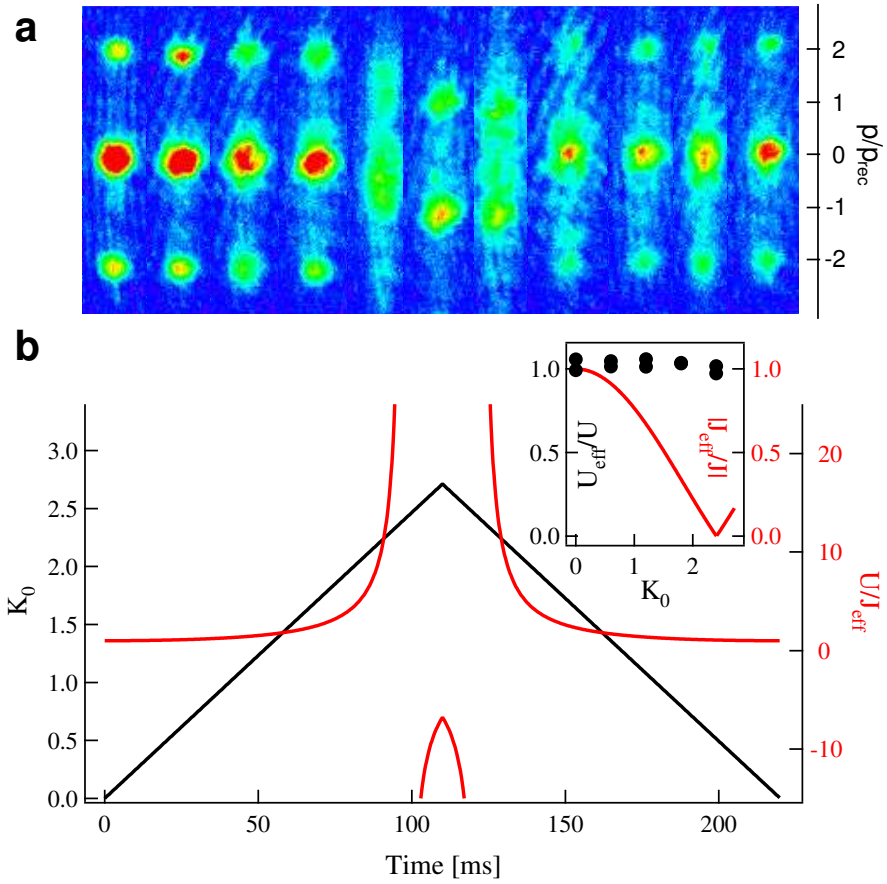

Figure 4.17: **a**. Interference patterns for a lattice driven at 6 kHz starting from 18 $E_{\rm rec}$ with a ramp of 113 ms from $K_0 = 0$ to $K_0 = 2.7$ and the same ramp back to $K_0 = 0$. **b**. Ramp of K_0 and corresponding value of $U/J_{\rm eff}$. **inset**. $|U/U_{\rm eff}|$, evaluated from the side peak populations for the interference patterns in **a** and $|J/J_{\rm eff}|$ versus K_0.

abatically follow the ground state. The presence of the point of the ramp where the tunneling time diverges forbids to have a strictly adiabatic process at the passage. It may be supposed that, when the band is flat at $J_{\rm eff} = 0$, quantum fluctuations and inter-particles interactions produced a delocalization of the momentum distribution inside the Brillouin zone, and, when the system enters in the regime with negative $J_{\rm eff}$, the ensemble follows the new ground state with momentum distribution peaked at $\pm p_{\rm rec}$. This is only a phenomenological picture and it is also not completely clear from the theoretical point of view if a contribution to this transition may come from

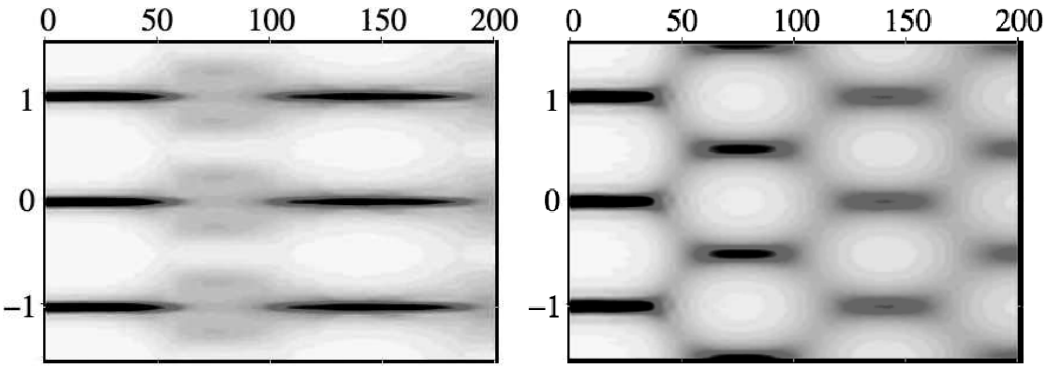

Figure 4.18: Momentum spectrum for $n/2$ (left) and n (right) atoms in n sites during a ramp of K_0 from 0 to 10. The horizontal axes are the number of driving cycles and the vertical axes are the momentum expressed as $p/2p_{\mathrm{rec}}$. From [26]

approximations applied in the treatment of our system with through Floquet theory.

Looking back to the experiments presented in paragraph 3.5, the time required to form the inverted pattern when the modulation was suddenly switched on has a clear connection with the observed *relaxation* in the inverted band regime of figure 4.17

Figure 4.18 shows the result of an interesting simulations preformed by A. Eckardt [26] in which K_0 is ramped from 0 to 10 in a system with $n/2$ (left figure) and n (right figure) atoms and n sites. It's evident that the phase coherence in the regions with negative J_{eff} is obtained only when the number of atoms is commensurable to the number of site, suggesting that the appareance of the two peaks structure is strictly bound to the creation of an insulator phase at $J_{\mathrm{eff}} = 0$ (impossible when the number of atoms is smaller than the number of sites). This numerical results have to be taken just as a hint for future theoretical checks. The real system is in fact composed of thousands of atoms per site and the contribution from the confinement trap is not negligible, while in the simulations of figure 4.18 the external harmonic potential is neglected.

4.7.5 Bloch Oscillations

Up to now we have studied the effect of the shaking by looking at the role of a small tunneling term on the cloud expansion or on the lifetime of the condensate coherence. We investigated in Chapter 3 how the Floquet theory,

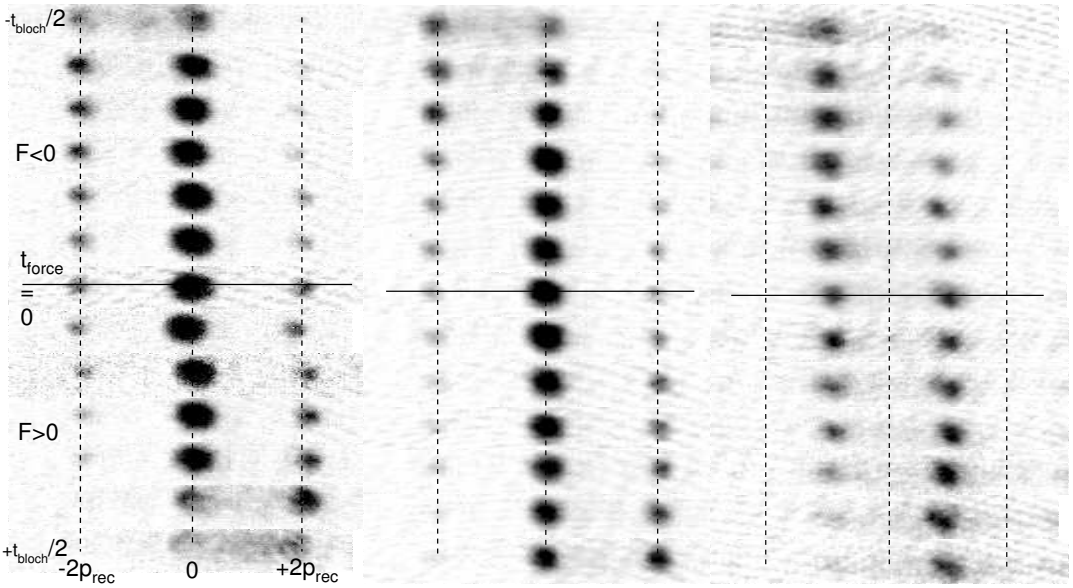

Figure 4.19: Interference patterns obtained by applying a force to the BEC in shaken lattices for different values of K_0 and optical depth: from left to right $K_0 = 0$, $V_0 = 6\ E_{\rm rec}$, $K_0 = 0$ and 4, $V_0 = 10\ E_{\rm rec}$ The shaking strength is ramped up to K_0 in 10 ms and the driving frequency is 3 kHz. The images are taken for $t/t_{bloch} = n/12$ with $n = -6...0...+6$ and negative times correspond to a force applied in the opposite direction.

predicts that a forced system is represented by a modified bands. We studied this feature by controlling the condensate dynamics in the driven regime. A fundamental phenomenon related to the dynamics inside a band are the Bloch oscillations whose features have been studied in solid state physics and also in the physics of ultra-cold gases ([67], [17]). When a force F is applied to the atoms for a time t_{force}, the envelope of the peaks of the interference pattern is shifted by:

$$\Delta x = \frac{(F t_{force})}{m} t_{t.o.f.}. \tag{4.6}$$

By definition, the time required to move with a force F the condensate envelope center at $v = 2v_{\rm rec}$[3] is called t_{bloch}.

Dressing the condensate in order to scan all the band with a sampling time $2\pi/\omega$, we require the condition $t_{\rm bloch} \gg T$ to satisfied. The data of Figure 4.19 was obtained with the shaking frequency 3 kHz ($T = 0.33$ ms) and $F = 0.075\, d_L/E_{\rm rec}$ corresponding to a $t_{\rm bloch}$ of 4.24 ms. Dynamical instabilities

[3]It corresponds to the side peak of the interference pattern when no force is applied.

([86] and [15]) due to the long time spent at the edge of the Brillouin zone (visible in the undriven regime) were suppressed in the driven ones by using a deeper lattice (10 E_{rec}). According to the negative value of J_{eff} for K_0 equal to 4, the Floquet state of lowest mean energy corresponds to a quasimomentum $q = \pm p_{\mathrm{rec}}$ at the edge of the Brillouin zone and they represent the initial condition for the Bloch oscillations. After the application of the force F for $t_{Bloch}/2$ the pattern is symmetric and centered on $q = +p_{\mathrm{rec}}$.

The tunneling parameter J as seen in Chapter 3 is responsible of the shape of the band and the observation of Bloch oscillations in driven lattices can be used in future experiments in order to explore the energy dependence whence to verify how J_{eff} acts on the bands.

4.8 Final considerations

The results shown in this chapter demonstrate that the idea of the *dressed matter waves* is not only a powerful tool for the analytical treatment of periodically perturbed systems, but can be a possible experimental technique for the adiabatic manipulation of the quantum ground state of an ensemble of cold atoms loaded into an optical lattice. This capability enormously enlarges the range of realizable systems to use for the studies of fundamental phenomena of quantum physics. Moreover, as proposed in [28], the possibility to mix different Wannier states of the same site by radiofrequency adds additional capability to the quantum state engineering. Another example of successful experimental ideas will be shown in chapter 6 where we will see how the dressed matter waves can be used to undergo a quantum phase transition. Before this step we need to understand the superfluid-insulator transition with particular attention to the features that characterize it and allow to probe its realization in ultracold gases.

Chapter 5

Trap modulation spectroscopy of the Mott insulator regime

The realization of the Mott insulator phase transition in an optical lattice was a very successful demonstration of quantum simulation with cold gases ([39]). In this Chapter I will explain the features of the *undriven regime* i.e., in a static lattice without moving and how it can be studied by using the Bose Hubbard Model. Moreover I will explore the compression of the insulator regime. After a brief introduction and a short review of past experiments on this subject, I present a novel measurement based on the modulation of the confining trap and I will show how this technique can be used for identifying the Mott insulator transition.

5.1 The Mott insulator in quantum gasses

The Bose Hubbard Model presented in 3.1 is a useful tool for explaining more complicated phenomena such as quantum phase transitions. The Bose Hubbard Hamiltonian, in fact, has two different kinds of ground state and the transition from one to the other depends on the balance between the parameters U and J. When the interactions are negligible, the hopping term J dominates the system (i.e. $J \gg U$) and the BEC is delocalized in the lattice. This ground state can be represented as a superposition of identical Bloch waves

$$|\Psi_{SF}\rangle_{U/J\approx 0} \propto \left(\sum_{i=1}^{M} a_i^\dagger\right)^N |0\rangle \tag{5.1}$$

where N is the number of atoms and M the number of lattice sites. A well defined macroscopic phase exists causing the presence of interference peaks

in the *time of flight* images. In agreement with the Heisemberg principle, the number of atoms at each site is, therefore, not defined and follows Poissonian statistics with $var(n_i) = \langle n_i \rangle$.

If, on the other hand, the interaction energy becomes important, the tunneling events are energetically unfavorable. In the limit $U \gg J$ the ground state wavefunction is simply the product of the Fock states of the atom numbers for each lattice site.

$$|\Psi_{MI}\rangle_{J\approx 0} \propto \prod_{i=1}^{M} \left(a_i^\dagger\right)^N |0\rangle \tag{5.2}$$

The exact knowledge of the number of atoms for each site is compensated by the maximized uncertainty of the phase of the single wavefunctions and hence the *time of flight* images of the atoms in this state are characterized by the absence of interference peaks and the profile appears as an incoherent sum of the on-site wavefunctions (as seen in paragraph 4.7.2). The continuous phase transition from one ground state to the other is driven by quantum fluctuations and the transition can be observed only at $T = 0$ as thermal fluctuations have to be negligible. The passage from one regime to the other is governed by the interaction energy and by the relative weight $U/(zJ)$ where z is the number of nearest-neighbour sites. Using the approximate formulas 3.4 for U and J, we have:

$$\frac{U}{zJ} = \frac{ka_s}{\sqrt{2}} \exp\left(2\sqrt{\frac{V_0}{E_{rec}}}\right). \tag{5.3}$$

Figure 5.1 shows the typical interference patterns for a condensate in the superfluid (figure on the **left**) and Mott insulator regime (**center**). The loss of visibility it is evident in the latter case. The coherence of the ensemble (**right**) can be restored decreasing back the lattice depth to a value for which the hopping term J becomes dominant. In the next chapter (paragraph 6.4.1) we will quantify the visibility of the pattern and will show its dependence on the parameter $U/(6J)$.

The critical depth for the transition from the superfluid to the Mott insulator has been numerically evaluated ([34], [52]) with several methods. The value in the case of unit occupation in two and three dimensional systems can be evaluated with mean-field theory (MFT) as $U/(zJ)_{crit} = 5.89$ (see in [83]) or the quantum montecarlo simulations (QMC) procuced $U/(6J)_{crit} = 4.9$ in 3D ([8]) and $U/(4J)_{crit} = 4.17$ in 2D. For the uniformly filled one dimensional system the value given by QMC is $U/(2J)_{crit} = 1.69$, as the value from mean field theory doesn't converge.

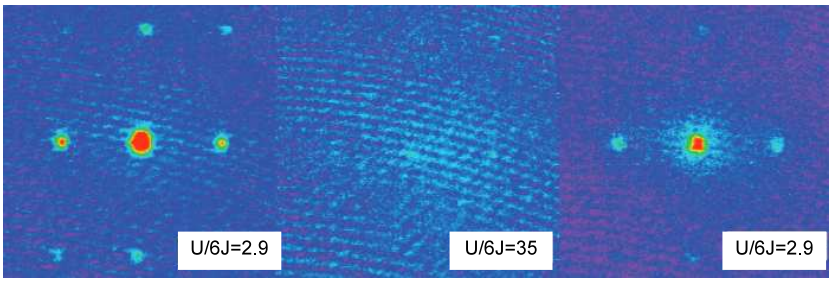

Figure 5.1: Example of interference patterns of a condensate loaded in a three-dimensional lattice. Clear interference peaks of superfluid regime (**left**) disappear when the system enter in the Mott insulator regime (**center**). The coherence is restored (**right**) when the lattice depth is decreased below the critical value of U/(6J).

5.1.1 Harmonic potential and the appearance of shells

In the realistic case of an ensemble of atoms contained in a harmonic trap there is no perfect commensurability between the number of sites and the number of atoms. This confiment can be introduced in the Bose Hubbard Hamiltonian 3.3 by adding an energy term ϵ_l which depends on the position of the atoms:

$$H = -J \sum_{\langle l,j \rangle} a_l^\dagger a_j + \frac{U}{2} \sum_l n_l(n_l - 1) + \sum_l (\epsilon_l - \mu) n_l \tag{5.4}$$

where we also introduced the chemical potential μ. It acts as a Lagrangian multiplier to fix the mean number of particles when a grand canonical ensemble is considered. The confinement potential term ϵ_l can be approximated at the center of the trap with a parabolic profile $\frac{1}{2} m\omega^2 d_L^2 l^2$.

In the inner part of the trap the probability of finding more than one atom per site will be higher and the above threshold of $U/(zJ)$ for one atom per site is no longer valid. Hence by increasing the lattice depth, the external region will be the first where the phase transition will take place while in the central region the system will be superfluid with an average number of atoms larger than one. At larger lattice depth a second region characterized by two atoms per site will enter the MI regime. This structure made of different shells (usually refered to as "wedding cake" structure) has been observed using microwave spectroscopy ([7]) or the visibility of the pattern ([36]). Figure 5.2 **a** shows the different thresholds in $U/(zJ)$ of the different insulating shells in a three dimensional lattice.

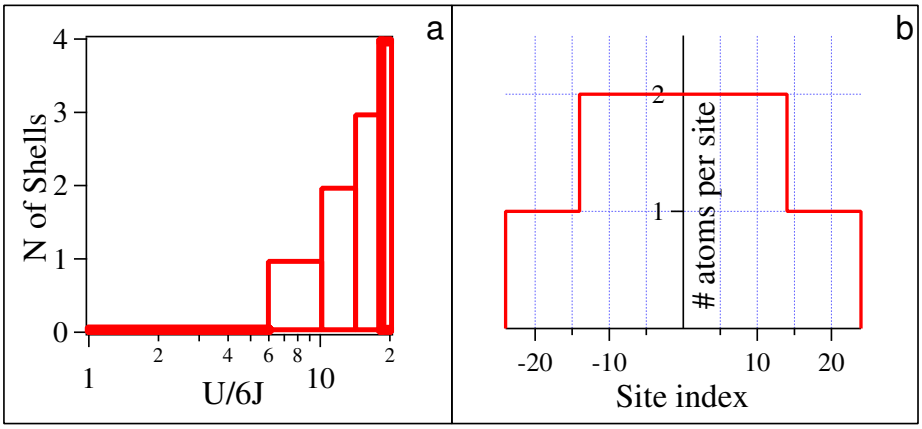

Figure 5.2: **a**. Critical values of $U/(6J)$ for the formation of insulator regime with different numbers of atoms per site in a three dimensional lattice. The values are obtained by using the parameters of our set-up. **b**. Two-shell cake structure for the parameters of our system. The number of atoms is $6 \cdot 10^4$ and the trap frequency $\omega_{x,y,z} = 68, 68, 96$ Hz.

By using the parameters of the trap and of the lattice, it is possible to evaluate the number of shells created in the presence of a deep lattice as a function of the total number of atoms in the condensate([23]). For the parameters of our apparatus the Mott insulator should exhibit a two-shell structure as shown in figure 5.2 **b**.

5.1.2 The excitation gap in the Mott insulator

One of the fundamental features of the Mott insulator is the presence of an energy gap in the excitation spectrum. In fact, in the superfluid regime, any small amount of energy released into the system can be acquired as a collective excitation of the superfluid, leading to a gapless excitation spectrum. In the Mott regime, on the other hand, the lowest possible excitation is the passage of an atom to a site that is already occupied. The energy difference between the atom and hole excitations can be evaluated and it is equal to U. At $T = 0$ the atom cannot move to a neighbouring site due to the energy gap and the insulating properties are natural consequences. In the literature the gapped spectrum has been observed ([39]) and numerically studied ([12]) by introducing a periodic modulation of the lattice depth. The perturbative study of the resulting hamiltonian is quite a hard task and can only be solved numerically. The Hamiltonian without the lattice depth modulation is the

Eq. 3.3

$$H_0 = U_0 H_U - J_0 H_J \tag{5.5}$$

where the compressed notation $H_J = \sum_{\langle l,j \rangle} a_l^\dagger a_j$ and $H_U = \frac{U}{2} \sum_l n_l(n_l - 1)$ is used. As the modulation of the depth $V = V_0 + \Delta V \sin(\Omega_{BH} t)$ affects both U and J, it corresponds in the linear response regime to a perturbed Hamiltonian.

$$\begin{aligned} H_0 &= (U_0 + \delta U)\, H_U - (J_0 + \delta J)\, H_J \\ &= H_0 + \delta U\, H_U - \delta J\, H_J \\ &= H_0 + \delta H. \end{aligned} \tag{5.6}$$

The perturbation of the Hamiltonian contains, as expected, contributions coming both from the hopping term and from the on site energy. For simplicity, δH can be written as:

$$\begin{aligned} \delta H &= \delta U\, H_U && && - \delta J H_J \\ &= \frac{U_0}{U_0}\delta U\, H_U - \frac{J_0}{U_0}\delta U\, H_J && + \frac{J_0}{U_0}\delta U\, H_J && - \frac{J_0}{J_0}\delta J\, H_J \\ &= \frac{\delta U}{U_0} H_0 && + J_0 \left(\frac{\delta U}{U_0} - \frac{\delta J}{J_0} \right) H_J \\ &= \frac{\delta U}{U_0} H_0 && + \kappa H_J \end{aligned} \tag{5.7}$$

where δU and δJ will be evaluated at the optical lattice depth V_0 as $\Delta V [\partial U / \partial V]_{V0}$ and $\Delta V [\partial J / \partial V]_{V0}$. The first term of Eq. 5.7 is simply an offset in the energy and cannot induce excitations while the second term is a contribution to the hopping. The probability of exciting the system will be proportional to κ^2 and to the hopping term $|\langle g | H_J | n \rangle|^2$ where $\langle g|$ and $|n\rangle$ are the ground state and an excited level. The problem is to find the energy spectrum of the excitation. The numerical simulations show that for lattice depths below the transition the system is characterized by a continuos spectrum; on the contrary, in deep lattices the spectrum is characterized by a peak of excitation at the frequency U/h.

Figure 5.3 shows measurement of gapless and gapped spectra (the peak at $2U/h$ is related to excitation in lattice sites with two atoms). In order to characterize the Mott insulator we measured the excitation spectrum in two different configurations. In the first case only one lattice depth was modulated with 30% amplitude (spectrum **b** of figure 5.3) and in the second case all three lattice depths were modulated with 10% of amplitude (spectrum

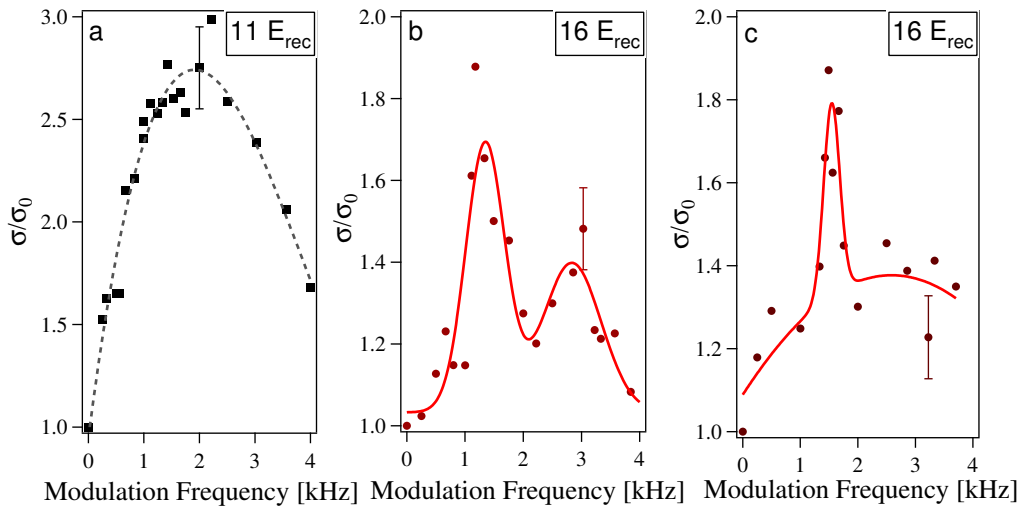

Figure 5.3: **a, b**. Spectra of the Superfluid (left $\rightarrow U/(6J) = 3.5$) and Mott-Insulator (right $\rightarrow U/(6J)$=13.9) obtained by modulating the depth of one of the lattices at 30% for 15 ms. After a ramp down to 4 E_{rec} for the thermalization of the ensemble the ratio between the width with and the width without the lattice depth modulation are measured. The appearance of the gapped peak is evident in the spectrum of the Mott insulator. **c**. Excitation spectrum obtained by modulating the depth of all the three lattices at 10% for 15 ms. The peak at U/h is narrower and closer to the expected value of 1.6 kHz.

c of figure 5.3). We find from equations 3.4

$$\begin{aligned}
\left[\frac{\delta U_{V_0}}{U_0}\right]_{10\%\times 3} &= \sum_{i=x,y,z}\left[\frac{\delta U_{V_{0,i}}}{U_0}\right]_{10\%} = 3\times 2.5\% \\
\left[\frac{\delta U_{V_0}}{U_0}\right]_{30\%\times 1} &= \left[\frac{\delta U_{V_{0,x}}}{U_0}\right]_{30\%} = 7.5\% \\
\left[\frac{\delta J}{J_0}\right]_{10\%} &= \left[\frac{\delta J}{J_0}\right]_{30\%}.
\end{aligned} \tag{5.8}$$

Therefore equivalent results should be found applying the larger one-dimensional modulation and the weaker three dimensional one, on the contrary it is evident in figure 5.3 that the width of the peak is more than halved in the case of three lattice depths modulated at 10%. This feature can be interpreted as a more precise spectroscopy of the system when a more isotropic perturbation is applied (a feature not taken into account in the linear response approximation and in the approximated analytical solution for

U and J of equations 3.4).

The presence of the gapped energy spectrum has been used in ([39]) as a demonstration of reaching the Mott Insulator regime even if theoretical works ([57]) have disagreed on that statement by stressing that this peak can appear also for an ensemble close to the MI regime but characterized by several defects (like holes in the atomic distribution). However, a narrow peak excitation for frequency U/h is cited in [12] as a clear evidence of the transition.

5.1.3 The compressibility

The gapped excitation spectrum leads to a peculiar behavior of the Mott Insulator regime: the incompressibility. The classical definition of isothermal compressibility is related to how easily the volume of an ensemble can be reduced by increasing the external pressure:

$$\kappa_{classical} = -\frac{1}{\mathcal{V}}\left(\frac{\partial \mathcal{V}}{\partial \mathcal{P}}\right)_T \tag{5.9}$$

where $\mathcal{V}$ is the volume, $\mathcal{P}$ the pressure and T the temperature.

If an external compression is applied to an ideal Mott Insulator, in order to reduce the volume of the system, atoms have to occupy a smaller number of sites, thus increasing the on-site energy. The smallest energy necessary for the compression is thus the gap previously discussed. In simulations ([3]) the global compressibility takes into account the long range correlations and is defined as

$$\kappa_{global} \propto \left[\langle \sum_{i,j} n_i n_j \rangle - \langle n \rangle^2\right] \tag{5.10}$$

The *global* compressibility has been observed by looking directly at the *in situ* size of the cloud after a single adiabatic compression of the trap (experiment and theory for fermions in [77]). A *local* compressibility can be defined as related to the local fluctuations in the number of atoms per site:

$$\kappa_{local} \propto \left[\langle n_i \rangle^2 - \langle n \rangle^2\right]. \tag{5.11}$$

i.e. for a completely flat distribution of atoms in a single shell Mott insulator, this value is trivially zero. These quantities were used in the experiment done with fermions reported in [51] where the concentration of doubly occupied sites was observed.

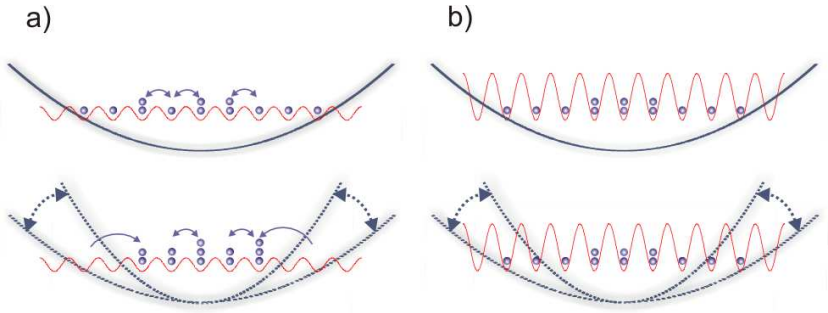

Figure 5.4: Scheme of the detection for dynamical compressibility of an ensemble of cold atoms in an optical lattice. **a)** In the superfluid regime repeated compressions of the trap lead to a compression of the condensate and hence to excitations; **b)** whereas in the Mott insulator regime the condensate becomes incompressible and no excitation takes place.

5.2 Dynamical compression

The numerical and experimental realization of the compression of the BEC presented in this thesis has been achieved by a periodic modulation the trap frequency and by observing the *time of flight* width of the cloud. A wider distribution of the cloud after such periodical *compression* phase reflects a release of energy into the system, which means that the trap compression has induced double or more occupancy in the lattice sites. In order to avoid that the system adiabatically follows the minimum energy ground state, the modulation of the trap frequency was chosen to be higher than the tunneling rate J between neighbouring sites. Hence the quantity measured with this technique should be defined as a *dynamic compressibility* and future theoretical efforts are needed to understand how it is related to the static global and local compressibilities.

5.3 1D system

5.3.1 Numerical calculations

The periodical compression of the condensate has been numerically studied[1] by fixing the number of atoms and the lattice depth and by substituting the

[1]Theoretical work done by R. Fazio and S. Montangero (SNS Pisa) and G. Pupillo (ICQC Innsbruck).

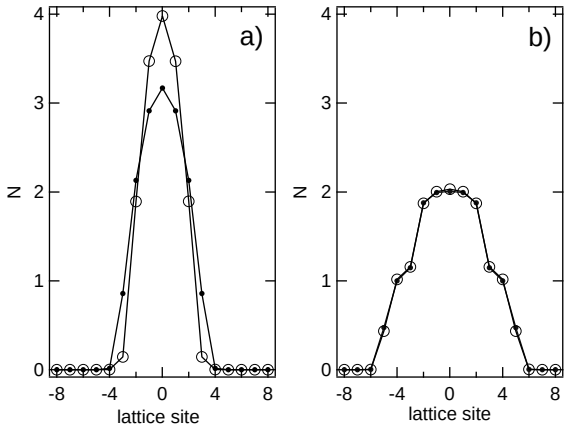

Figure 5.5: Distribution of 15 atoms in a one-dimensional lattice after a periodical compression with $\delta\omega/\omega$=1. (The filled circles represent the atomic distribution at $t = 0$, while the open circles show the distribution after the compression). **a)** In the superfluid regime ($U/(2J)$=2) the density in the center increases and with that the energy of the system; **b)** whereas in the Mott insulator regime ($U/(2J) = 9$) the atom distributions are indistinguishable.

frequency ω of the harmonic potential with a periodically modulated one:

$$\omega(t) = \omega_0 \left(1 + \frac{\delta\omega}{\omega} \sin^2(\frac{\Omega}{2}t)\right), \tag{5.12}$$

where $\delta\omega$ is the peak-to-peak modulation depth and $\Omega/2\pi$ the modulation frequency. The calculation of this scheme in one dimension was done using a time-dependent Density Matrix Renormalization Group (tDMRG) algorithm. (For details of the simulations see reference [61]). In figure 5.5 the numerical simulations for the two regimes are reported. When the lattice depth is lower than the critical depth for the superfluid—Mott-insulator transition, the distribution of the atoms in the lattice sites after the application of the trap modulation (open circle) is different from the one that at $t = 0$ (filled circle), which has a smaller number of multiply-occupied sites. In the Mott insulator regime, on the other hand, the initial and final distributions are indistinguishable from each other, which demonstrates that the system has not been excited by the repeated trap compressions.

In order to compare simulations and experimental data, the quantities

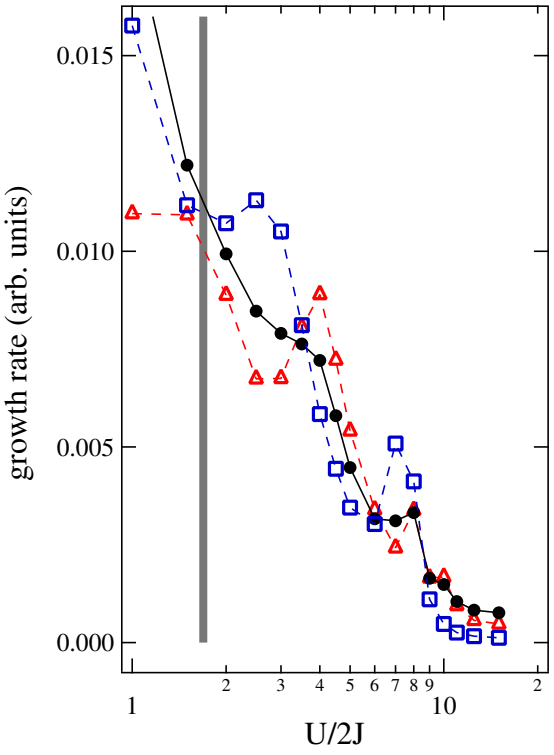

Figure 5.6: Numerical calculation for the relative energy growth rate in a 1D system. The trap modulation strength $\delta\omega/\omega$ is 0.22 and the total number of atoms $N = 15$ (△) and $N = 10$ (□), corresponding to occupation numbers $n = 2$ and $n = 1.5$ in the central sites. The filled circles • are the average over total numbers $N = 5, 10$ and 15. The vertical line is the QMC prediction for the formation of the first shell.

obtained from the tDMRG are the relative energy growth rate[2], defined as:

$$\frac{(acquired\,energy)}{(initial\,energy)(t_{comp})} \tag{5.13}$$

where t_{comp} is the duration of the trap modulation. Figure 5.6 was obtained by evaluating the relative growth rate at different values of $U/(2J)$ with $\delta\omega/\omega = 0.22$ for a total number of atoms $N = 15$ (open triangles) and $N = 10$ (open squares), corresponding to occupation numbers $n = 2$ and $n = 1.5$ of the central lattice site which are typical values for our experiment. The error in the values obtained are around 20% for $U/(2J) > 2$ and around 40% for smaller values.

We note here that while in our experiment J is changed through V_0 (which has little effect on U in the range of parameters used here), in the numerical simulation J is kept constant and U is varied. Nevertheless, the agreement between our experimental results and the simulation proves that it is the ratio U/J rather than the two individual parameters that governs the systems behaviour.

[2]In the literature this is also called the energy acquisition rate EAR ([47]).

5.3.2 Experimental procedure

The experimental procedure was the following:

- adiabatic loading of the condensate into an optical lattice of depth V_0;
- periodical modulation of the dipolar laser power between P_0 and $P_0(1+\alpha)$ for a time t_{comp} with a frequency $\Omega/2\pi$;
- the modulation was switched off and the optical lattice was ramped down in 15 ms to $V_0 = 4\ E_{\rm rec}$ for a 10 ms thermalization period;
- 23.3 ms of time of flight and measurement of the width σ of the central peak of the interference pattern (see figure 4.6).

The same procedure applied with $\delta\omega/\omega = 0$ has been used to measure the width σ_0 of the cloud expanded without modulation.

As the frequency of the harmonic confinement ω depends on the square root of the laser power, for $\alpha < 1$ the resulting frequency modulation strength can be approximated as:

$$\delta\omega = \omega\left(\sqrt{1+\alpha} - 1\right). \tag{5.14}$$

In our realization P_0 corresponds to a mean trap frequency $\omega/2\pi$ of the trap around 80 Hz.

5.3.3 Compression of a 1D system

The first realization of the compressed system was done in a configuration that was as similar as possible to the numerical simulations. The condensate was adiabatically loaded into the lattices with two of them ramped to a value of 26 $E_{\rm rec}$. The atoms were thus confined in parallel tubes and the tunneling between neighbouring tubes was suppressed. By modulating the power of one of the dipolar trap beams, the tubes are compressed in the longitudinal direction. In order to verify that the compression in the transversal direction didn't lead to additional excitations, first we performed the compression procedure by modulating only the power of the dipolar beam collinear with the lattice beam direction. The result of this investigation allowed us to verify the absence of excitations due to the compression in the direction where the lattice was 26 $E_{\rm rec}$. We also verified that the effects of the compression on the cloud were independent of the frequency $\Omega/2\pi$ when it is higher than the tunneling rate J/h. Figure 5.7 shows the ratio σ_x/σ_{x0} obtained at three

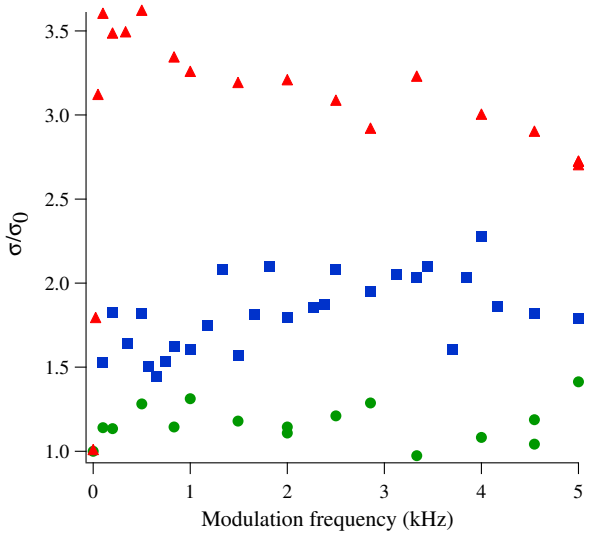

Figure 5.7: Ratio σ/σ_0 for different modulation frequencies in a modulated 1D system (two lattices at 26 $E_{\rm rec}$). The lattice depths are 9 $E_{\rm rec}$ (▲, $\delta\omega/\omega = 0.41$), 13.5 $E_{\rm rec}$ (■, $\delta\omega/\omega = 0.41$) and 16 $E_{\rm rec}$ (●, $\delta\omega/\omega = 0.80$). The trap frequencies are $\omega_{x,y,z} = 69$, 68, 96 Hz and t_{comp} 5 ms.

different lattice depths by modulating in a frequency range between 0 and 5 kHz. In particular for the lattice depth 9 $E_{\rm rec}$, it's evident that the ratio σ/σ_0 increased quite fast with frequency for $\Omega/2\pi < 100$ Hz and than stabilized to a value around 3. The slight residual dependence on the frequency for $\Omega/2\pi > 1000$ Hz can be a spurious effect of the PID controllers stabilization that decreases its precision for frequencies closer to 6 kHz, which is their technical limit.

In order to compare the experimental results with the simulation of Figure 5.6, the same parameters are used: the modulation was applied for 5 ms with $\delta\omega/\omega = 0.22$ and $\Omega/2\pi = 1$ kHz. The theoretical and experimental vertical scales are linearly matched by imposing that:

- when the relative growth rate is zero, the ratio σ/σ_0 has to be one;
- at a fixed shallow lattice depth the growth rate and the σ/σ_0 are proportional. Therefore the vertical axes of the quantities were matched.

For our configuration, this corresponds to a relation between the values of the two axes: $\sigma/\sigma_0 = \frac{2.5}{0.014}$ (*relative growth rate*) + 1. The slope of experimental data is in good agreement with the numerical simulations and demonstrate that the energy released in the system during the compression can be directly connected to the width growth rate obtained from the simulations.

In our experimental results the relative ratio between compressed and uncompressed width decreases with increasing values of $U/(2J)$ and no evident steps are visible. In particular for the 1D system experimentally realized with two very deep lattices and a harmonic external confinement, the density and

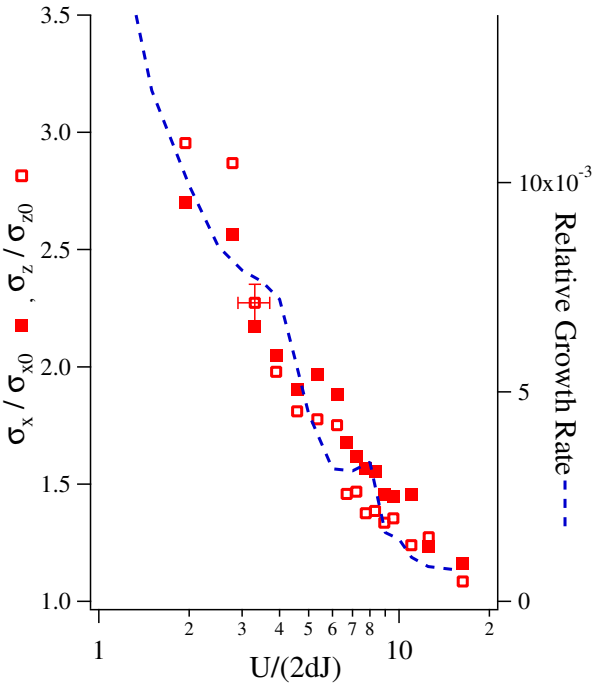

Figure 5.8: Ratio σ_x/σ_{x0} (■) and σ_z/σ_{z0} (□) in a modulated 1D system (two lattices at 26 $E_{\rm rec}$) with $\delta\omega/\omega$ = 0.22. The trap frequencies are $\omega_{x,y,z}$=69, 68, 96 Hz, $\Omega/2\pi = 1$ kHz and t_{comp} 5 ms. The dashed line are the results of simulation shown in Figure 5.6 and the theoretical vertical scale is matched to the experimental data.

the total number of atoms is not the same for a tube close to center of the trap and those on the edge of the cloud and for different tubes the transition takes place at different values of $U/(2J)$. By looking at the total effects on the condensate, one doesn't expect to observe a precise value $U/(2J)$ at which the total ensemble changes its dynamical compression but instead a smooth transition to an insulator regime should be observed. In fact the quantum MonteCarlo simulation is not able to determine a precise value for the formation of the second shell.

5.4 Compression of the 3D Mott insulator

The characterization of the response of the system in a three dimensional configuration is a very interesting goal as we can perform various *traditional* tests (visibility of the interference pattern, excitation spectrum (figure 5.3)) in order to identify the critical value $(U/J)_{\rm crit}$ of the superfluid—Mott-insulator transition.

The condensate was adiabatically loaded into the three mutually perpendicular lattice beams and the trap modulation was applied with $\delta\omega/\omega = 0.41$ and $\Omega/2\pi = 1$ kHz. The first evidence of a different behavior of the system was observed by looking at the ratio σ/σ_0 and applying the modulation for

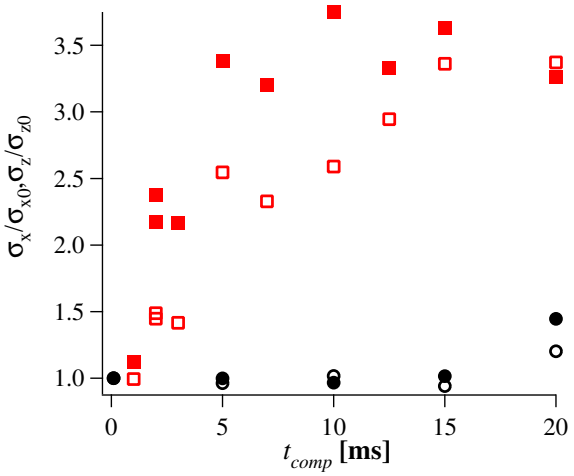

Figure 5.9: Ratio σ_x/σ_{x0} and σ_z/σ_{z0} for a condensate compressed in a three dimensional optical lattice for increasing values of t_{comp} with $\delta\omega/\omega = 0.41$. The trap frequencies were $\omega_{x,y,z} = 68$, 68, 96 Hz and the modulation frequency was $\Omega/2\pi = 1.5$ kHz. Data at $V_0 = 10$ $E_{\rm rec}$ (U/(6J) = 2.6): ■ = σ_x/σ_{x0}, □ = σ_z/σ_{z0} below the Mott insulator transition; Data for $V_0 = 16$ $E_{\rm rec}$ (U/(6J) = 13.9): ○ = σ_x/σ_{x0}, ● = σ_z/σ_{z0}, above the Mott insulator transition.

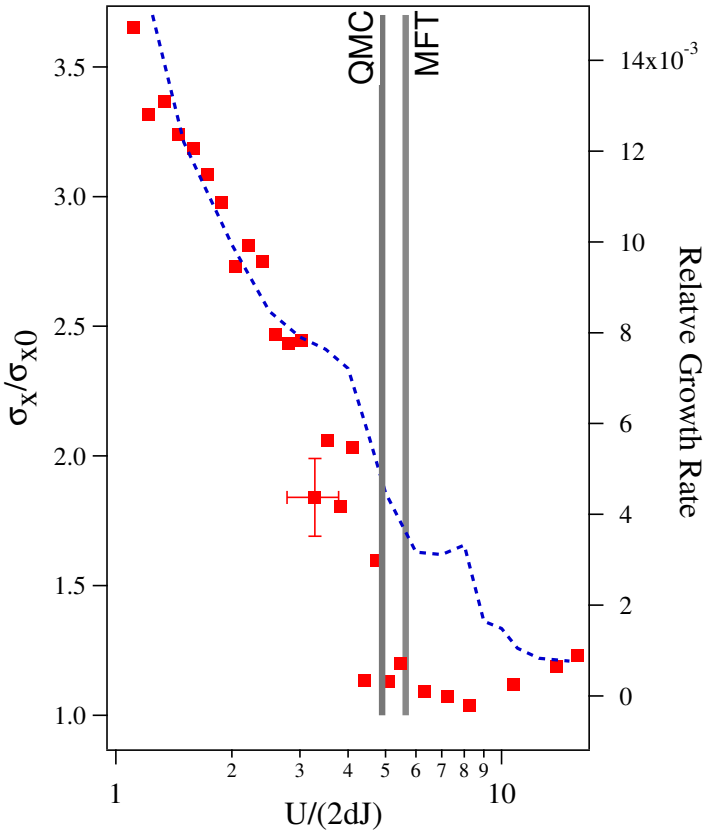

Figure 5.10: Ratio σ_x/σ_{x0} (■) for $\delta\omega/\omega = 0.41$ in a three dimensional lattice, The trap frequencies are $\omega_{x,y,z} = 69$, 68, 96 Hz and the trap modulation is applied for 10 ms with $\Omega/2\pi = 1$ kHz. The dashed line is the result of the 1D simulation and the grey lines are the MFT and QMC thresholds for the SF-MI transition.

different values of t_{comp} (Figure 5.9).

Below the SF-MI transition ($V_0 = 10\ E_{\rm rec}$) the *t.o.f.* width of the compressed condensate increased initially proportionally to the time of application and then saturated for $t_{comp} > 10$ ms. In the Mott insulator regime ($V_0 = 16\ E_{\rm rec}$), on the contrary, the compression didn't excite the condensate and the ratio σ/σ_0 was around unity up to 20ms. This behavior is in good agreement with the theoretical picture of the incompressibility of the Mott insulator.

Fixing the time t_{comp} at 10 ms, we measured the ratio σ/σ_0 in the three dimensional configuration for lattice depths in the range 4-16 $E_{\rm rec}$ (figure 5.10). The results show how σ/σ_0 decreases with increasing $U/(6J)$, reaching unity around $U/(6J)$=5. For larger values of $U/(6J)$ σ/σ_0 is approximately constant and equal to one. Compared to the slope of the 1D simulation, the deviation from the linear behavior is evident when the system approaches the critical value $(U/(6J))_{\rm crit}$. This dramatic change of behavior can be interpreted as a sign of the passage to an incompressible regime. The energy released into the system doesn't simply decrease with the probability of tunneling between sites and there is a sudden suppression of the system's excitability at the formation of the first insulator shell.

5.4.1 Observation of Shells

The presence of a shell is a key features of the Mott insulator regime and one can expect that the compression of the cloud should be able to detect the *wedding cake* structure. This possibility is strictly connected to the amplitude of the modulation and the consequent energy shift. The value ϵ_l in equation 5.4, in fact, changes quadratically with the distance from the center of the trap and during the modulation the energy variation at the center of the trap will be smaller than the ones in the peripheral regions. An easy estimate of the energy difference can be made by considering the energy offset between two neighbouring lattice sites during the compression as a function of the radial position of the site and of the modulation amplitude. One finds:

$$\begin{aligned} \epsilon_l^{comp} &= \frac{m d_L^2 l^2}{2} \left(\omega + \delta\omega \sin^2(\Omega/2t)\right)^2 \\ &= \epsilon_l + \frac{\alpha}{2}\epsilon_l - \frac{\alpha}{2}\epsilon_l \cos(\Omega t) \\ &= \epsilon_l + \Delta\epsilon_l, \end{aligned} \tag{5.15}$$

where we use the dependence of $\delta\omega$ on the amplitude modulation of the dipolar trap power αP_0. In order to obtain the mean energy offset between

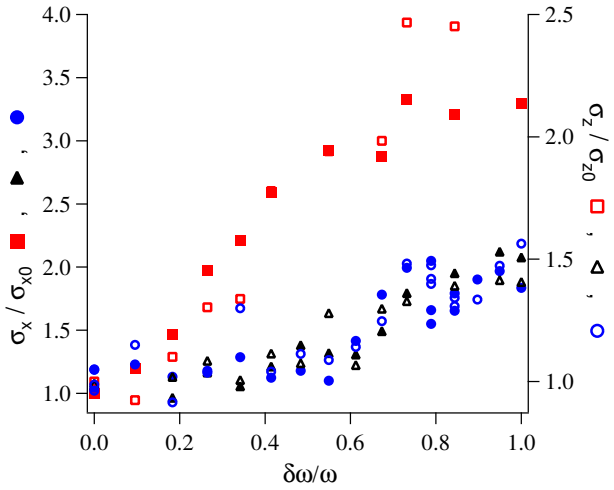

Figure 5.11: Ratio σ_x/σ_{x0} and σ_z/σ_{z0} for a variable compression amplitude $\delta\omega/\omega$. The trap frequencies was $\omega_{x,y,z}$ = 68, 68, 96 Hz and the compression frequency $\Omega/2\pi$ is 1kHz. Data in the superfluid phase at V_0 = 11 E_{rec}(U/(6J)=3.5) :■ = σ_x/σ_{x0}, □ = σ_z/σ_{z0}; Data in the Mott insulator phase at V_0 = 13.5 $E_{\rm rec}$ ($U/(6J)$ = 7.2):△ = σ_x/σ_{x0}, ▲ = σ_z/σ_{z0}; and at V_0 = 14.5 E_{rec}(U/(6J)=9.5) :● = σ_x/σ_{x0}, ○ = σ_z/σ_{z0}.

two lattice site at a distance l from the center of the trap, the derivation of $\Delta\epsilon_l$ with respect to the lattice position can be calculated and averaged in time

$$\langle\frac{\partial\Delta\epsilon_l}{\partial l}\rangle = \epsilon_l \times \frac{\alpha}{l} = \epsilon_l \times \frac{(\delta\omega/\omega+1)^2-1}{l} \tag{5.16}$$

If we request that this energy offset has to be higher than the excitation energy U of an atom in the neighboring occupied site, in an outer site ($l = 25$ in our case) with one atom per site, this condition is fulfilled when $\delta\omega/\omega > 0.71$. When the modulation amplitude is higher than this value, one expects the Mott insulator shell created at the edge of the cloud to *melt down* and the system to become compressible again[3].

In order to validate this picture, we applied the modulation for 5 ms at increasing values of $\delta\omega/\omega$ with $\Omega/2\pi = 1$ kHz (figure 5.11) The ratios σ_x/σ_{x0} and σ_z/σ_{z0} have been obtained for three different values of $U/(6J)$ (3.5, 7.2 and 9.5), one below and two above the Mott insulator transition. For $U/(6J)$ = 3.5 σ_x/σ_{x0} increases linearly with $\delta\omega/\omega$. By contrast in the insulator regime the ratio is constant to one and than starts to increase linearly only at $\delta\omega/\omega$ around 0.6, not so far from the previous rude estimate.

By fixing $\delta\omega/\omega$ at 0.73, the ratio σ_x/σ_{x0} and σ_z/σ_{z0} have been measured for different values of $U/(6J)$ as shown in Figure 5.12. For this parameters, σ_x/σ_{x0} and σ_z/σ_{z0} decrease for increasing $U/(6J)$; a step is evident around

[3]By using a higher value of $\delta\omega/\omega$ it should be possible to study the compression of the inner shell with two atoms.

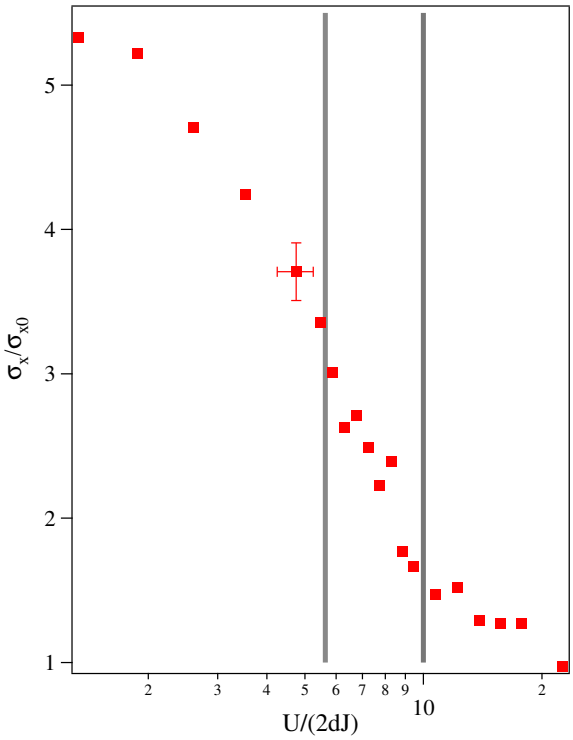

Figure 5.12: Ratio σ_x/σ_{x0} (■) for $\delta\omega/\omega = 0.73$, trap frequencies ($\omega_{x,y,z}$=68, 68, 96 Hz) and the trap modulation was applied for 15ms at $\Omega/2\pi = 1$ kHz. The vertical lines are the two values of $U/(2dJ)$ predicted for the first and second shell.

$U/(6J) = 6$ while σ_x/σ_{x0} stops decreasing for values higher than $U/(6J) = 9$. This behavior can be interpreted as follows:

- for a shallow lattice ($U/(6J) < 5$) the modulation at higher $\delta\omega/\omega$ releases energy into the system which is in superfluid regime;
- for $5 < U/(6J) < 9$ the system is less compressible but the first shell is melted down because $\delta\omega/\omega$ is large. The ratio σ_x/σ_{x0} is well larger than one and keeps decreasing
- for $U/(6J) > 9$ also the second shell starts to form and the whole system cannot be excited anymore.

This last value of $U/(6J)$ is compatible with the lattice depth necessary for achieving a Mott insulator regime with the two shells in for our system.

Two phenomena lead to a residual excitability at the system: First of all the cake structure at finite value of $U/(6J)$ is characterized by a superfluid shell between the two insulator ones where the density of atom per site $1 < n < 2$. The modulation of the trap releases always energy into this part of the ensemble even if the other region have already a gapped spectrum. Moreover, as we underlined in the theoretical introduction, the SF-MI

phase transition takes place at $T = 0$, which is not realistic for an experimental realization. Numerical simulations for system at finite temperature show how the wedding cake profile completely disappears when $k_B T/U >$ 0.1-0.2 ([35]). It isn't a trivial problem to determine the temperature of the condensate inside an optical lattice. Before the formation of the shell its temperature decreases and it can be estimated[4] from effective mass in the bands ($m_{\text{eff}} = 2\hbar^2\partial^2 J/\partial k_L^2$, [4]) and analytical evaluation of the system entropy ([44], [74]). For our parameters the ratio $k_B T/U$ at $(U/(6J))_{\text{crit}}$ is 0.12 and 0.19, which means that in our system a small amount of energy acquired by the system can compromise the cake structures. Future improvement in the condensate temperature can be done especially by decreasing the frequency of the confinement trap. However the determination of this temperature is so complex that smoothness of the shell structures itself has been suggested for the direct determination of the temperature of the condensate ([33] and [74]).

5.4.2 Compressibility of a dephased ensemble

In order to demonstrate that the observed response is not due only to the decrease of the tunneling rate but is strictly related to the many-body ground state of the Bose-Hubbard Model, an additional test was done. For this purpose we loaded the condensate into a deep lattice with a diabatic ramp and tested the compressibility of the resulting excited state. The diabatic ramp was realized by adiabatically loading the atoms into a lattice of depth 5 E_{rec} and by adding a linear ramp in 0.1 ms to the final value V_0. By ramping the lattice depth back to zero after a holding time of 5 ms, we checked in the *time of flight* pictures that there were no atoms with momentum $\pm 2\hbar k_L$ (typical of the first excited band). The larger width of the central peak is a clear sign of low energy excitation inside the fundamental band. These tests confirms that we have a condensate loaded in the fundamental band but not in the ground state of the Bose Hubbard Hamiltonian

To minimize side effects due to the loading process we performed trap modulation spectroscopy for the same time used for the previous investigations ($t_{comp} = 5$ ms). Figure 5.13 shows how the sudden decrease of the σ/σ_0 close to $U/(6J) = 5$ disappears when the condensate is diabatically loaded in deep lattice. In fact the condensate can be well excited also above the critical value of $U/(6J)$ and this feature is in good agreement with the idea that the compressibility is related to the excitability of the ensemble.

[4]The two ways here discussed suffer both for the approximations on the effect of the

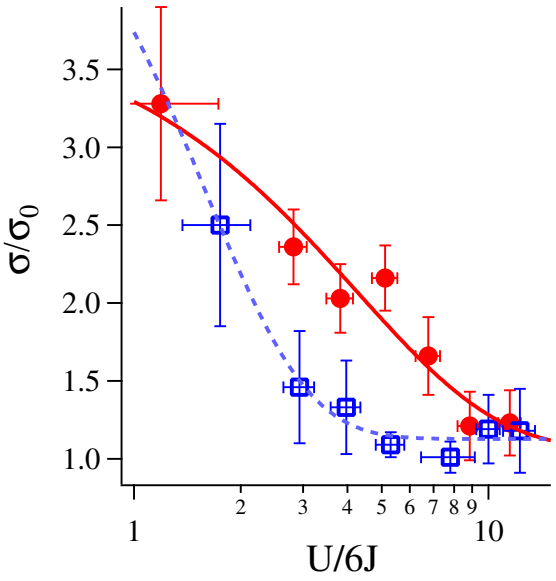

Figure 5.13: Ratio σ/σ_0 for trap modulation of a BEC loaded adiabatically (□) and diabatically (●) into final the lattice depth. The modulation frequency $\Omega/2\pi$ is 1 kHz and applied for 5 ms with $\delta\omega/\omega = 0.43$. The continuous and dashed lines are guides to the eye.

confining potential and the presence of the shells

Chapter 6

Dynamical realization of the Mott Insulator regime

In Chapter 4 we presented how the strong driving of an optical lattice can be efficient in reaching regimes which cannot be reached with *standard* techniques. In Chapter 5 we discovered how the increase of dimensionality in the system can enrich the physics of ultra cold gases confined in a periodic potential. In this Chapter we will combine these two topics by showing our results for shaken 2 and 3-dimensional systems. In particular we report the possibility of carrying the condensate from a superfluid regime to a Mott insulator phase by adiabatically changing the driving parameters.

6.1 Shaking in higher dimensions

As we stressed in Chapter 4, the adiabaticity and the coherence of the driving are strongly connected to the energy spectrum and to the presence of avoided crossings that the system has to pass. The presence of a additional lattice in one of the other two spatial directions introduces more complexity to the spectrum 4.2. Moreover, the condition

$$\hbar\omega \gg U \tag{6.1}$$

becomes more restrictive especially for a three dimensional lattice where, close to the SF-MI transition, $U \sim$1.3 kHz. On the other hand the upper limits in frequency due to the excited band of the lattice are not expected to change. For these two reasons the range of possible driving frequencies is expected to be smaller than the one observed in the presence of only one lattice.

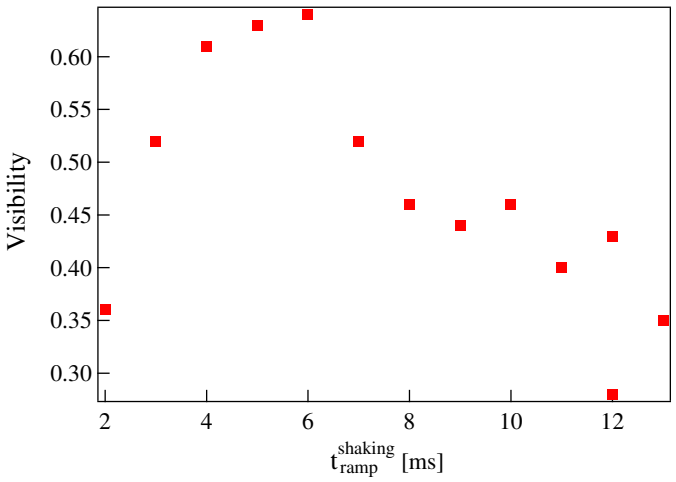

Figure 6.1: Visibility as a function of the ramp time $t_{ramp}^{shaking}$ for a system with two shaken lattice directions. The lattice depth is 10 E_{rec}, the frequency of the sinusoidal shaking is 3 kHz, $K_0^{test} = 2.4$ and $\Delta t^{shaking} = 5$ ms.

At the same time, the presence of an additional lattice could be a good way to suppress the excitations in the transversal directions. For our typical condensates in the one dimensional configuration every lattice site contains hundreds of atoms and the collective Bogoliubov-like excitations of each ensemble contribute to the complexity of the spectrum of the system. Moreover collisions lead to a transfer of energy to the spatial directions perpendicular to the lattice, complicating the interpretation of the adiabaticity of the driving.

6.2 Is two better than one?

As done for the system with only one lattice direction, we tested the different parameters that characterize the energy spectrum and the condition for an adiabatic following of the driving amplitude variations in two- and three-dimensional lattices. The optimized loading of the atoms in a static two-dimensional lattice was done with a 200 ms ramp with an exponential curve of characteristic time 7 ms (see figure 2.5) and the procedure was the same as in Figure 4.5.

In Figure 6.1 the visibility of a system with two driven lattices is shown. As seen in Chapter 4, the result of this test confirms the presence of a narrower range of ramp times that can be used for driving. From the absolute value of the visibility, it is also evident that even in the best conditions, the maximum value is around only 0.65 despite of the larger lattice depth, low compared to the values observed in the 1D case.

The starting depth is, also in this case, a fundamental parameter to be analyzed. By fixing $t_{ramp}^{shaking}$ at 5 ms and the holding time $\Delta t^{shaking}$ at 5 ms,

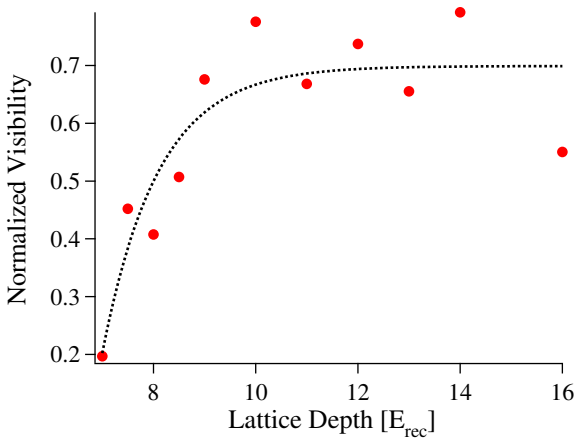

Figure 6.2: Visibility of the interference pattern with two driven lattices as a function of the starting lattice depth. The visibility is normalized to the value obtained without driving for a system with two shaken lattice directions. The shaking frequency is 3 kHz, $K_0^{test} = 2.4$, $t_{ramp}^{shaking} = 5$ ms and $\Delta t^{shaking} = 5$ ms.

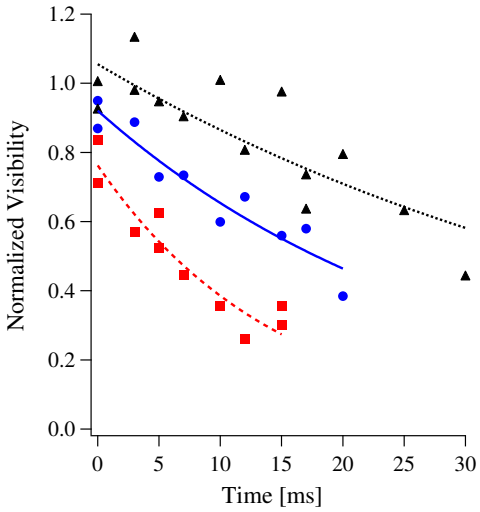

Figure 6.3: Visibility of the interference pattern with two driven lattices as a function of the holding time. The visibility is normalized at the value obtained without driving. The shaking frequency is 3 kHz, K_0^{test} 2.4, $t_{ramp}^{shaking}$= 5 ms . ■ 7 $E_{\rm rec}$ (lifetime = 14.7 ms), • 9 $E_{\rm rec}$ (29.4 ms) and ▲ 12 $E_{\rm rec}$ (50.4 ms).

the visibility was measured for different starting depths. In order to avoid effects due to a different lifetime in lattices with different depths, the visibility is normalized to the value obtained by holding the BEC for the same time but without shaking. The result of this test (Fig 6.2) confirms that the coherence is better preserved for a deeper lattice. The distance between two levels in the energy spectrum is in fact larger for a deeper lattice. This feature decreases the number of avoiding crossings to pass and so the adiabatic driving is less problematic.

This idea is confirmed by the measurement of the lifetime in a 2D-driven system. Figure 6.3 shows the visibilities observed for three different lattice depths with the following procedure: ramp up in 5 ms of the driving to K_0^{test} = 2.4, variable holding time and ramp down to K_0 =0 in 5 ms.

As done for the configuration with a single lattice, the visibility of a two-

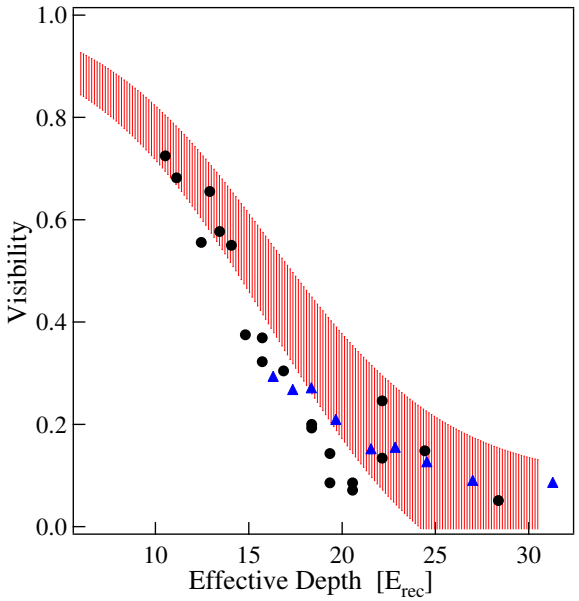

Figure 6.4: Visibility of the interference pattern for two different starting depths (• 10 $E_{\rm rec}$ and ▲ 15 $E_{\rm rec}$) in the presence of driving. The driving frequency was 3 kHz, the ramp time $t_{ramp}^{shaking}$ 5 ms and the holding time $\Delta t^{shaking}$ 5 ms . The shaded area is the visibility obtained for an undriven lattice.

dimensional shaken system is shown in Fig. 6.4 as a function of the effective lattice depth. The data shown confirm how the visibility measured for a static lattice (the shaded area) is comparable with the ones obtained by shaking the optical lattice.

As done for the 1D system we can consider the possibility to observe the Mott insulator regime in the two-dimensional configuration. Its feasibility in a static 2D configuration has been demonstrated in a recent experiment [81] and one can expect that the problems seen for the 1D Mott insulator transition are less critical in this case. For the same parameter considered in paragraph 4.7.3, in a small condensate of our apparatus there are around 10 atoms per site and the critical ratio $(U/(4J))$ is ~ 40. Starting the ramp of driving in a lattice of 25 $E_{\rm rec}$ ($J = 3.7$ Hz), the threshold value of U/(4J) is reached for K_0 is 1.87, corresponding to a suppression of tunneling of a factor 3.3 only.

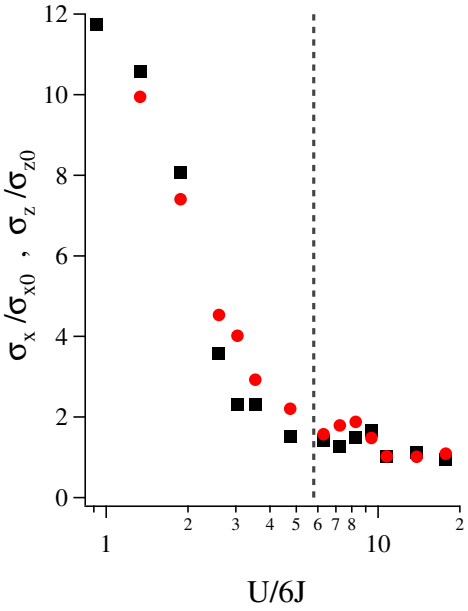

Figure 6.5: Ratio σ_x/σ_{x0} (■) and σ_z/σ_{z0} (●) in 3-dimensional lattice. The driving frequency is 4 kHz and the strength $K_0^{test} = 2.39$. The ramp time is $t_{ramp}^{shaking}$ is 5 ms and $\Delta t^{shaking}$ is 5 ms. The vertical line is the 3D threshold value predicted by the mean-field theory.

6.3 Towards the 3-dimensional adiabatic driving

In the previous section we demonstrated the possibility to adiabatically introduce the driving for a condensate loaded into a two dimensional lattice. The next step is to find the conditions in a three-dimensional configuration and try to induce the quantum phase transition studied in Chapter 5. As we saw, *superfluid* and *Mott insulator* are notions related to the ground state of the bare Bose-Hubbard model and so it becomes necessary that the condensate in the ground state of the undriven system H_0 (with B.H. parameters U and J) follows adiabatically the ground state of the shaken system $H_0 + H_1(t)$ (with U and J_{eff}) during the ramp of the driving amplitude. As we saw in Chapter 4 the photons of energy $\hbar\omega$ fold the energy spectrum in figure 4.2. In three dimensions this coupling is present in all the spatial directions and the density of avoided crossings should be higher. So the choice of the experimental protocol for carrying the system trough the quantum phase transition is not trivial.

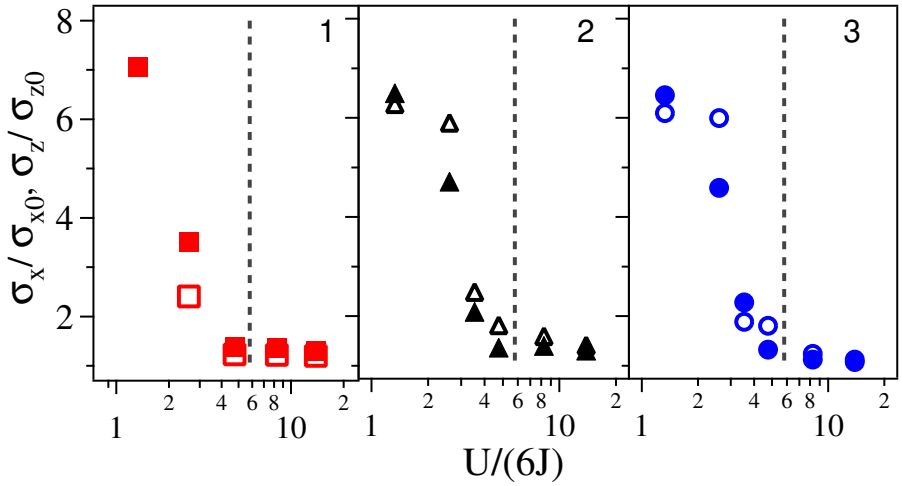

Figure 6.6: Ratio σ/σ_0 in three dimensional lattices with different numbers of shaken lattices, on to three from left to right. The driving frequency is 3 kHz, $t_{ramp}^{shaking} = 8$ ms, $\Delta t^{shaking} = 0$. The full symbols are σ_x/σ_{x0} and the empty ones are σ_z/σ_{z0}.

6.3.1 Lower limit for the lattice depth in three dimensions

For our final goal it is fundamental to find an adiabatic protocol that allows us to ramp up the shaking strength starting from a lattice depth lower than the limit for the SF-MI transition. As we saw in Chapter 5 the limit for the transition is $U/6J \sim 5.8$, corresponding to $V_0 \sim 12.7\, E_{\rm rec}$. In order to find the minimum value V_0 from which adiabatic ramping of K_0 is possible we applied the modulation to the three dimensional system for different values of V_0. The minimum depth is very close to the SF-MI transition threshold. Moreover, it's evident that in the insulator regime the already small value of the tunneling rate $J/\hbar$ allows to ramp adiabatically the shaking. In the Mott insulator regime, in fact, the wavefunction of the single sites are decoupled and a further suppression of tunneling is trivial.

Since the Bose-Hubbard Model the parameter J is separable in the contributions from the three spatial directions J_x, J_y and J_z, it could be plausible to think that introducing the shaking only in one or two lattice directions should simplify the energy spectrum. Hence we looked at the differences of the 3D Bose gas response by changing the number of shaken lattices. For this study we performed the usual test procedure[1] and by measuring the mini-

[1]In all the investigation performed with three lattices the thermalization of the cloud

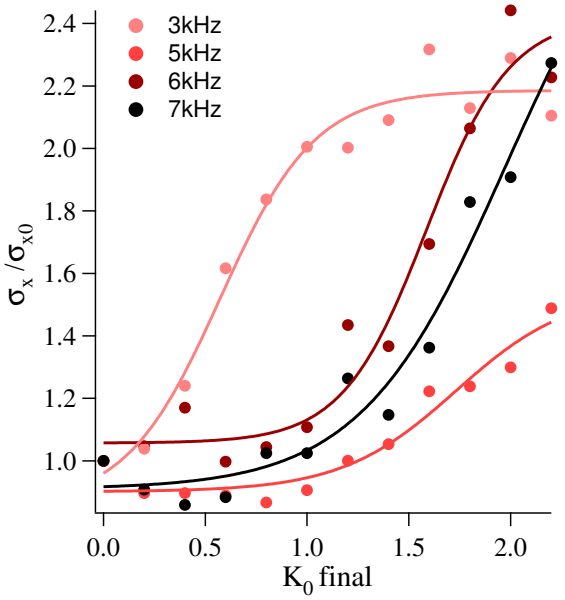

Figure 6.7: Ratio σ_x/σ_{x0} in a shaken lattice with $K_0/t_{ramp}^{shaking}$ kept constant for different driving frequencies. The total shaking time 20 ms ($\Delta t^{shaking} + 2t_{ramp}^{shaking}$) and the lattice depth 11.5 $E_{\rm rec}$.

mum value of $U/(6J)$ from which the system could be adiabatically driven, as in Figure 6.5. We changed the number of shake dimensions at a fixed lattice depth when the shaking was at 3 kHz with $K_0 = 2.38$. Figure 6.6 shows that there are no evident differences between the three configurations, contrary to our intuition.

More complicated combinations of the three lattices have been tested (a driven lattice with the other two at a larger depth, two shaken lattices with a deeper third one, etc) but none of this consideration has shown any evident advantage in terms of adiabaticity towards the realization of the MI regime.

6.3.2 Ramp time for a three-dimensional lattice

In the previous sections and chapters we studied the driving ramp by fixing the final value of K_0 and changing the quantity $t_{ramp}^{shaking}$. In that way the deviations from adiabaticity during the ramp were measured as a larger width in the momentum distribution after reaching the final value of K_0. Figure 6.7 shows the ratio σ_x/σ_{x0} obtained by maintaining constant the slope of K_0 ($K_0 = 1$ reached in 1 ms, $K_0 = 2$ in 2 ms and so on) and stopping the ramp of the driving at different values of shaking strength and, after a holding time, ramping K_0 down to zero. Moreover, the total shaking time ($\Delta t^{shaking} + 2t_{ramp}^{shaking}$) was kept constant at 20 ms.

after the driving was done for 10 ms at 8 $E_{\rm rec}$ after a ramp of 15 ms from the previous depth.

As we have seen in systems with lower dimensionality, the frequency plays a critical role in the adiabaticity. The frequency for which the σ_x/σ_{x0} is smallest at higher values of K_0 is 6 kHz. A driving frequency of 3 kHz, which in the 1D gave the best results, is in this case the frequency which gives the worst adiabatic following. The degree of adiabaticity that can be achieved with a driving frequency of 6 kHz and $K_0 = 1.7$ ($\sigma_x/\sigma_{x0} = 1.2$) is remarkable. For this value of suppression of the tunneling rate ($\mathcal{J}_0 = 0.4$), one can change U/J from a superfluid regime (for example $U/J = 3$) to an insulator phase ($U/J_{eff} = 7.5$). However a modest suppression of the tunneling, i.e. K_0 =1 (J/J_{eff}=0.77), can be adiabatically achieved also for other frequencies.

The fact that in a 3D lattice the driving ramp time for an adiabatic following is less than 5 ms seems surprising. The time required for adiabaticity should increase in fact, for large lattice depths, as the tunneling time is larger. However a time of 5 ms for the ramp of the driving at a fixed lattice depth is comparable with the time interval required to scan 11 E_{rec} and 16 E_{rec} using an exponential ramp of 150 ms and $\tau = 7$ ms of the lattice depth in the experiments without driving.

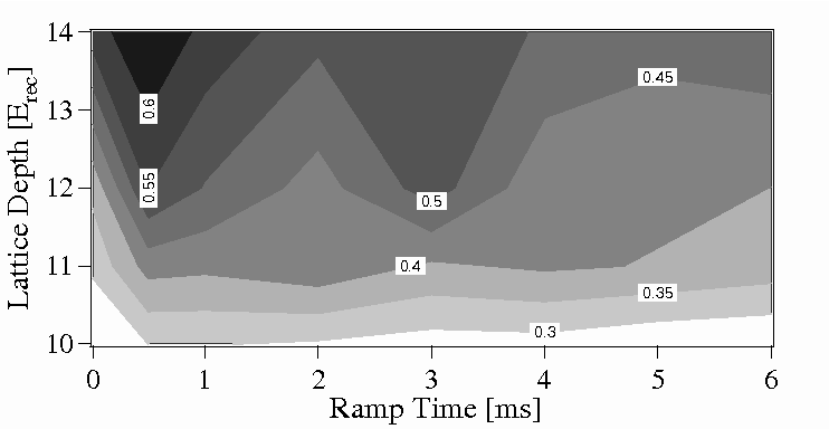

Figure 6.8: Contour plot of the ratio σ_0/σ by varying lattice depth and ramp time $t_{ramp}^{shaking}$ in a configuration with three driven lattices. The driving frequency is 6 kHz and the shaking amplitude $K_0^{test} = 2.2$.

As a final test in the three dimensional configuration, the best ramp time $t_{ramp}^{shaking}$ was searched for $K_0^{test} = 2.2$ and $\omega/2\pi = 6$ kHz shaking frequency. For such a strong driving, the adiabaticity is low despite the depth of the lattice however it is clear from the data in figure 6.8 that $t_{ramp}^{shaking}$ should be in the range $1 \div 4$ ms.

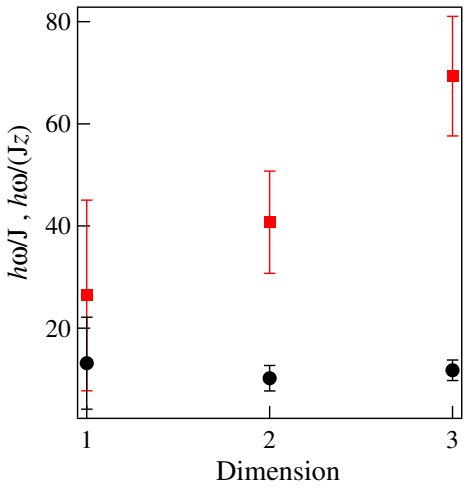

Figure 6.9: Critical values of $\hbar\omega/J$ (■) and $\hbar\omega/(zJ)$ (•) for different dimensionalities of the system. The error bars are the standard deviations of the values of $\hbar\omega/J$ obtained in the different combinations of the lattice depth and of the driving frequency.

6.3.3 Conclusions about dimensionality

The dependence on the dimensionality of the system is an important features connected to a possible universality in the strongly-driven systems. One of the most evident features in quantum phase transition is, in fact, the importance of the number of the neighboring atoms. The physics of spin systems and the QCD physics are typical examples.

The increase of number of lattices d in a Bose Hubbard model corresponds to

- an increasing number of nearest neighboring sites $z = 2d$ (2→4→6),
- an increased site energy U, i.e. at 10 E_{rec} for our dipole trap parameters 7.7→111→ 1150 Hz (see Paragraph 3.1),

From our tests it is evident that :

- the optimum ramp time $t_{ramp}^{shaking}$ decreases and also the range of possible values gets smaller;
- the lowest possible lattice depth increases and consequently the starting value of J decreases (remember that it depends exponentially on V_0);
- the frequency range decreases in width and the lowest possible frequency increases.

As discussed in 4.1 and [30], we could expect that the critical value of ω is given by the condition:

$$\hbar\omega \gg J. \tag{6.2}$$

Evaluating the ratio $\hbar\omega/J$ for all the tested configurations, we found that this value increases linearly with the dimensionality and so the normalized ratio $\hbar\omega/zJ$ is constant at about 12 (see Fig. 6.9). We also found that changing ω and J independently for a given d does not always give the same critical value of $\hbar\omega$ (as indicated by the error bars in Fig. 6.9). As already seen in Fig. 4.9 the conditions for good adiabatic following depend on the system's parameters J and ω in a more complicated way. All the possible conditions cannot be tested because of the very large number of combinations of different parameters and we performed experiments always at the extremes of the parameter ranges in order to define the borders of the problem. Therefore the present conclusions are only a first step in understanding the adiabaticity of Floquet state in strongly driven systems. Nevertheless they show that there is a wide range of parameters for which adiabatic control is possible.

6.4 Reaching and probing a driven Mott Insulator

The realization of the Mott Insulator regime has been considered one of the most outstanding demonstrations of the manifold possibilities of cold atoms in simulating quantum processes. In Chapter 5 I have explained the basic ideas behind the SF-MI phase transition and how we obtained and probed it by varying the lattice depth. In this chapter the realization of the Mott insulator regime will be used as a tool for confirming how the driving can be powerful in changing the properties of *dressed matter-waves*. To do so, I present the experimental probes presented for the static regime and now applied to the driven system.

6.4.1 Visibility of the interference pattern

The visibility of the interference pattern has been used also in this case for comparing the system in the traditional regime ([36]) to the one with driving. The typical interference pattern is shown in figure 6.10. Due to the existing relative angles between the lattice beams and the lines of sight of the camera, the peaks of the two horizontal lattices lie on the top of each other. The background signal is taken at the positions $\pm d_H/2, \pm d_L/\sqrt{2}$ with respect to the central peak. Hence the visibility is defined as

$$\mathcal{V} = \frac{\bar{n}_{max} - \bar{n}_{min}}{\bar{n}_{max} + \bar{n}_{min}}. \tag{6.3}$$

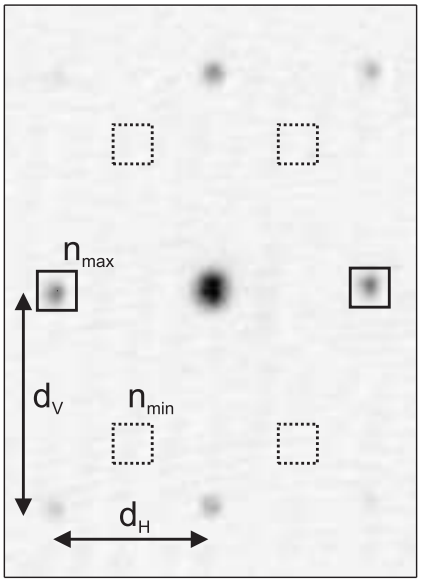

Figure 6.10: Typical interference pattern for a three dimensional lattice where the areas of the pictures used for the evaluation of the visibility are marked. n_{min} is measured at a horizontal distance of $d_H/2$ and vertical one $d_V/\sqrt{2}$ and it is averaged on the four different positions. n_{max} is taken on the horizontal peaks (they are the sum of the peaks of the two lattice directions on the plane).

where $\bar{n}_{max}$ and $\bar{n}_{min}$ are the averaged number of atoms on the side peaks and on the background reagions as shown in Figure refvisibilita. First we performed the *traditional* scan of the lattice depth (indicated by the shaded area of figure 6.11). For the driven regime scans, the lattice depth was exponentially ramped to two different initial values ($V_0 = 11\ E_{\rm rec}$ (•) and $V_0 = 12.2\ E_{\rm rec}$ (□)) and by mantaining constant the lattice depth, the driving amplitude was increased to the final value K_0 in 4 ms. After the sudden switching off of the lattice, the interference pattern was acquired. The data of visibility versus $U/(6J)$ are in good agreement with the results of the static lattice. The adiabaticity of the driving has been demonstrated by ramping the value of K_0 back to zero in 4 ms. The horizontal dashed lines represent the averaged visibility of the returns from different values of K_0 and they are clearly higher than the visibility without the ramp down of K_0. In particular for the data at $V_0 = 11\ E_{\rm rec}$, the return visibility is perfectly restored. The three cornerstones of this scan are shown in the tridimensional figure 6.12. The first picture is the interference pattern after the ramp of the lattice to $V_0 = 11\ E_{\rm rec}$. The second one is the dephased pattern of the ensemble in the driven Mott Insulator regime and the third one is the restored pattern after ramping down of the driving amplitude.

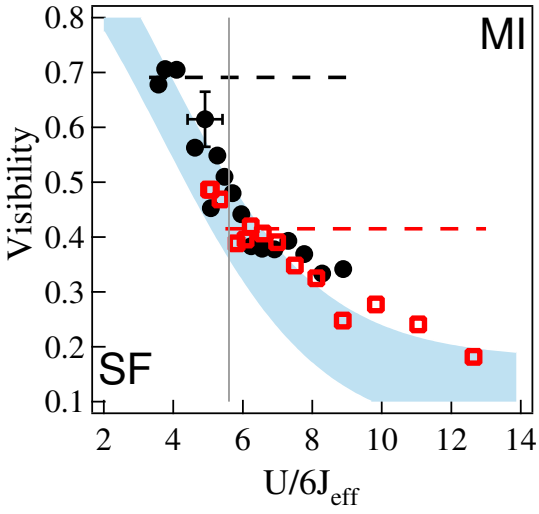

Figure 6.11: Visibility of the interference pattern as a function of $U/6J_{\text{eff}}$. For the two constant lattice depths $V_0 = 11\ E_{\text{rec}}$ (•) and $V_0 = 12.2\ E_{\text{rec}}$ (□) the driving strength was varied. The dotted black and red lines indicate the mean visibility after the return to $K_0 = 0$. The blue region is a fit (with the thickness of the region indicating the statistical error) to the experimental data taken for a varying lattice depth without driving, and the vertical grey line indicates the border between the superfluid (SF) and Mott insulator (MI) regions.

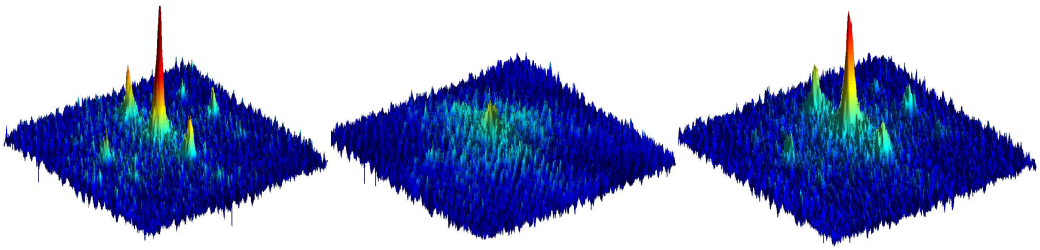

Figure 6.12: Realization of a driven Mott insulator regime in a 3D optical lattice. The lattice depth is constant at 11 E_{rec} (U/J=3.5) and the driving frequency is 6 kHz, the driving strength K_0 was ramped from 0 (left picture) to 1.62 (center picture, U/J_{eff}=7.9) in 4 ms and back again to 0 (right picture). The disappearance of the distinctive interference peaks in the middle figure marks the onset of the Mott insulator transition.

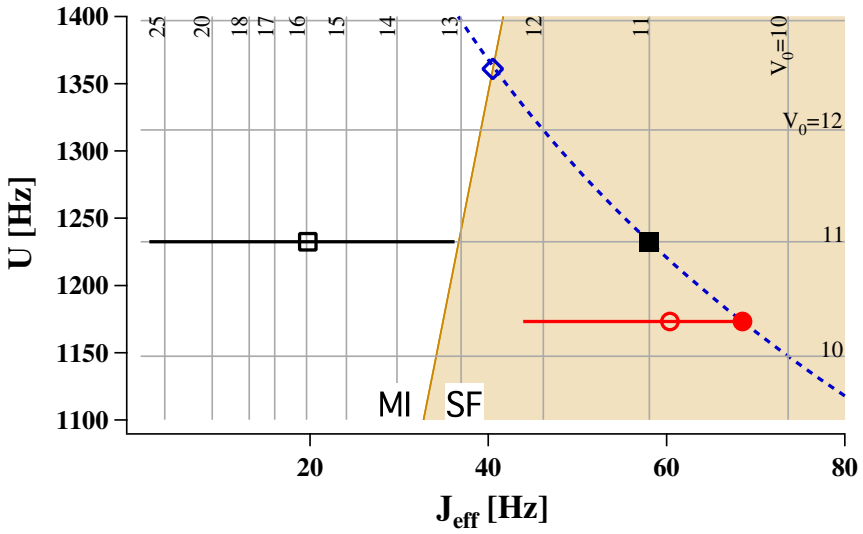

Figure 6.13: Phase space plot of the Bose Hubbard Model. The system is superfluid in the shaded area, Mott insulator in the white one. The dashed line follows the parameters of the undriven system: the diamond indicates the point of the transition by simple ramping the lattice depth. ● and ■ are the starting point of the shaken superfluid ○ and shaken insulator □. The horizontal thick lines show the ranges of J scanned during the amplitude modulation of the shaking strength K_0. The grey grid shows the values of lattice depth for the quantities U and J_{eff} on the axis.

6.4.2 Excitation spectrum of the driving-induced Mott insulator

One feature of the Mott insulator phase is the appearance of a gap between the ground state and the first excited level. We saw in Chapter 5 how this gap has been observed experimentally and how its presence changes the compressibility of the system. In the traditional spectroscopy of the Mott insulator spectrum, the periodical modulation of the lattice depth changes both J and U. On the contrary, the modulation of the driving amplitude is equivalent to applying a periodic perturbation only to the tunneling parameter J. In the third line of equation 5.7, in fact, the first term is zero and κ is simply equal to δJ_0. This means that the energy of the perturbed system has no offset introduced by the modulation and U doesn't change during the probing. Moreover the problem of a periodic vertical displacement of the the center of the confinement potential due to the dipolar effect of the lattice beams is avoided in this way.

In order to compare the gapless and gapped excitation spectra in the driven regime, we performed a modulation of the amplitude of the the shaking strength in two different regimes. In the first case the lattice depth was ramped to 10.3 $E_{\rm rec}$ and then the shaking strength K_0 was ramped to 0.7 in 6 ms ($J_{\rm eff}/J = 0.84$, $V_{\rm eff} = 10.8\ E_{\rm rec}$ and $U/6J_{\rm eff} = 2.85/0.84 = 3.39$) Hence the Bose gas remains in the superfluid regime. The strength K_0 was sinusoidally modulated for 14 ms with an amplitude of 0.54 in order never to enter in the range of parameters where $U/6J_{\rm eff}$ is higher than 5.8 (see Fig. 6.13 for a clearer view). Figure 6.14 **a** shows the thermal fraction normalized at the value without excitation, calculated from a bimodal fit to the condensate after ramping down the lattice to $V_0 = 4\ E_{\rm rec}$. The fraction increases with frequency without showing any particular features. We performed the same kind of test in a regime that is expected to be in the MI phase: V_0 11 $E_{\rm rec}$ with $K_0 = 1.8$ ($J_{\rm eff}/J = 0.34$, $V_{\rm eff} = 16\ E_{\rm rec}$ and $U/6J_{\rm eff} = 3.53/0.34 = 10.38$). The modulation amplitude of K_0 was 0.56. The excitation spectrum reveals the presence of a peak at 1.2 kHz, close to the prediction from Eq 3.4 (1.23 kHz). This feature confirms the appearance of a gap in the system.

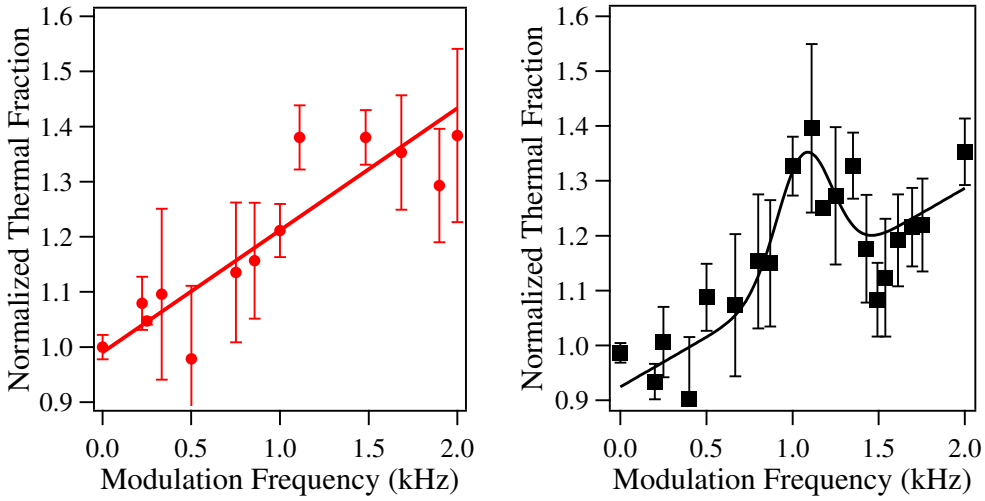

Figure 6.14: Excitation spectra in the superfluid (●) and the Mott insulator (■). Plotted here are the thermal part normalized at the value without excitation calculated from a bimodal fit to the condensate after ramping down the lattice to $V_0 = 4\ E_{\rm rec}$. On the left the lattice depth was $V_0 = 10.3\ E_{\rm rec}$ with $K_0 = 0.7$, while on the right $V_0 = 11\ E_{\rm rec}$ with $K_0 = 1.8$. The effective tunneling rate $J_{\rm eff}$ was varied with sinusoidal modulation of K_0 with an amplitude of 0.56 and 0.54, respectively. The solid lines are fits to guide the eye.

The complexity of our measurement is due to the two frequencies which play a role in the system. The one needed for detecting the gap is equal to U/h which is $\sim$1.3 kHz and the driving frequency on the other hand is only a factor four bigger (6 kHz). This proximity introduces clearly effects on the adiabatic following of system and the maintaining of the state in the ground state of the effective Hamiltonian in critical. However a narrow peak is a clear sign of reaching the Mott insulator regime

6.5 Probing the driven MI with trap modulation spectroscopy

The application of the trap modulation (see Chapter 5) should be a possible way of probing the driven Mott insulator regime. We tried to compress the system in a regime of parameters where the spectroscopy of the excitation spectrum showed the existence of a Mott insulating state, but the time of flight pictures showed very large widths also for small amplitude of the compression. These tests were performed by choosing the frequencies of the driving (6 kHz) and of the compression (1 kHz) used for the measurements of the previous sections. This means that the confining potential changes slowly on the timescale of the driving period, so that the atoms moved backwards and forwards experience a changing potential. This (relatively) slow variation of the harmonic trap could introduce further excitations in the driven regime not considered in the models used for driving and compression. We conclude that, at least for the parameters tested, the two techniques cannot be used simultaneously. More detailed investigations will have to be done in order to understand this restriction and possibly identify parameter regimes for which trap modulation can be used to probe the driven Mott insulator regime.

Conclusion and perspectives

In this thesis I studied the peculiar characteristics of time-periodically forced systems of ultracold gases in optical lattices. In particular I demonstrated the possibility of adiabatically transferring a Bose Einstein condensate from the ground state of a static regime to the corresponding one of a driven regime.

The results presented in Chapter 3 show how the driving can change the tunneling rate between two lattice sites independently of the atom-atom interactions. This rate has been studied by direct observation of the expansion of a Bose-Einstein condensate in different experimental conditions and the data are in perfect agreement with Floquet theory. Moreover, I have shown how the shape of the driving can be used for the selective suppression of different neighbouring orders of tunneling, and signs of this behavior have been observed.

I also demonstrated how the driving can be used for the adiabatic creation of a many-body ground state with modified fundamental properties. The tests and the examples of driven systems shown in Chapter 4 are a large step towards an understanding the possibilities and the limits for the adiabatic preparation of ultra cold atoms in strongly driven periodic potentials. The ranges of parameters where adiabaticity is preserved have been extensively studied, paying attention to the possible effects due to lattice depth, driving frequency and ramp time. In particular we observed a dependence of the adiabatic condition on the dimensionality of the system.

Owing to the results of these tests, we realized already well known quantum mechanical configuration and we also characterized new regimes that have been impossible to create with static potentials. The driven Mott insulator regime presented in Chapter 6 is a demonstration that the driving can adiabatically transfer the ground state from the static regime to the driven one also preserving all the coherence necessary for the observation of a quantum phase transition. The visibility of the interference pattern and the gapped excitation spectrum are two clear signs that the phase transition actually took place. Moreover in the study of the Mott insulator regime, I presented a novel technique (Chapter 5) which allows to characterized the

features of the dynamically compressed insulator.

The results of this thesis represent the first extensive experimental study on the adiabaticity in strongly driven regimes and demonstrate the perfect correspondence between the theory and the experimental systems. In the last years the interest in the scientific community on this subject was increased as analytical solutions of these regimes are impossible and the numerical simulation are limited to small systems. Examples are the precise mapping of the energy spectra of the driven system and the determination of the positions and the widths of the avoided crossings. Moreover the study of these regimes have large importance in the understanding of solid state systems in the presence of a strong external perturbation.

With ultra cold atoms it becomes possible to choose a Hamiltonian, simulate it with a large ensemble of particle and measure physical quantities important for the characterization of the system. Further implementations can be also done by adding a control on the atomic interactions (with Feshbach resonance) or by using fermions instead of bosons. In this way the condensate inside the optical lattice becomes a quantum *simulator* and can substitute the most powerful computational tools.

Publications and Useful Constants

List of publications based on the results of this thesis

- H. Lignier, C. Sias, D. Ciampini, Y. Singh, A. Zenesini, O. Morsch, and E. Arimondo. Dynamical control of matter-wave tunneling in periodic potentials. Phys. Rev. Lett., 99:220403, 2007. (*Chapter three*).

- A. Zenesini, H. Lignier, D. Ciampini, O. Morsch, and E. Arimondo. Coherent control of dressed matter wave. cond-mat: 0809.0768. Accepted for publication in PRL, 2008. (*Chapter four and six*).

- H. Lignier, A. Zenesini, D. Ciampini, O. Morsch, E. Arimondo, S. Montangero, G. Pupillo, R. Fazio. Trap modulation spectroscopy of the Mott-insulator transition in optical lattices. cond-mat: 0812.3005 . Submitted to PRA, 2008. (*Chapter five*)

- A. Eckardt, M. Holthaus, H. Lignier, A. Zenesini, D. Ciampini, O. Morsch and E. Arimondo. Exploring dynamical localization with a Bose-Einstein condensate. cond-mat: 0812.1997. Physics Review A 79, 013611 2009 (*Chapter three*).

- A. Eckardt, M. Holthaus, A. Zenesini, H. Lignier, D. Ciampini, O. Morsch and E. Arimondo. Signatures of dressed macroscopic matter waves. In preparation, 2009. (*Chapter four*).

Other publications

- C. Sias, H. Lignier, Y. P. Singh, A. Zenesini, D. Ciampini, O. Morsch, and E. Arimondo. Observation of photon-assisted tunneling in optical

lattices. Phys. Rev. Lett., 100:040404, 2008.

- C. Sias, A. Zenesini, H. Lignier, S. Wimberger, D. Ciampini, O. Morsch, and A. E. Resonantly enhanced tunneling of Bose-Einstein condensates in periodic potentials. Phys. Rev. Lett., 98:120403, 2007.

- A. Zenesini, C. Sias, H. Lignier, Y. Singh, D. Ciampini, O. Morsch, R. Mannella, E. Arimondo, A. Tommadin, and S. Wimberger. Resonant tunneling of Bose-Einstein condensates in optical lattices. New Journal of Physics, 10:053038, 2008.

- A. Zenesini, H. Lignier, G. Tayebirad, J. Radogstowicz, D. Ciampini, R. Mannella, S. Wimberger, O. Morsch, E. Arimondo, Time-resolved measurement of Landau-Zener tunneling in periodic potentials, in preparation, 2009

Useful Constant

m	$= 1.44 \cdot 10^{-25}\,\mathrm{kg}$		
$d_L = \lambda/2$	$= 421 \cdot 10^{-9}\,\mathrm{nm}$		
w_L	$= 100\,\mu\mathrm{m}$		
$v_{\mathrm{rec}} = v_{bloch}/2$	$= 5.45 \cdot 10^{-3}\,\mathrm{m/s}$		
E_{rec}	$= h \times 3.3\,\mathrm{kHz}$	$= 155$ nK	
w_{dip}	$= 100\,\mu\mathrm{m}$		
$\omega_{dipolar}^{min}$	$= 68(x,y)\,\&\,96(z)\,\mathrm{Hz}$	$\rightarrow \overline{\omega}_{dip}$	$= 76$ Hz
$U/6J_{crit}$	$= 5.8$		
$V_{0,crit}$	$= 12.7\,E_{\mathrm{rec}}$	$=1.97\ \mu$K	
U_{crit}	$= h \times 1.23$ kHz	$= 66$ nK	$= 0.42\ \nu_{\mathrm{rec}}$
J_{crit}	$= h \times 35$ Hz	$= 1.9$ nK	$= 0.012\ \nu_{\mathrm{rec}}$

Bibliography

[1] M. Anderson, J. Ensher, M. Matthews, C. Wieman, and E. Cornell. Observation of Bose-Einstein condensation in a dilute atomic vapor. *Science*, 269:198, 1995.

[2] N. Ashcroft and N. Mermin. *Solid state physics*. Saunders College, 1976.

[3] G. G. Batrouni, R. V., R. T. Scalettar, M. Rigol, A. Muramatsu, P. J. H. Denteneer, and M. Troyer. Mott domains of bosons confined on optical lattices. *Phys. Rev. Lett.*, 89(11):117203, Aug 2002.

[4] P. B. Blakie and J. V. Porto. Adiabatic loading of bosons into optical lattices. *Phys. Rev. A*, 69(1):013603, Jan 2004.

[5] M. Born and V. Fock. Beweis des Adiabatensatzes. *Z. Phys*, 51:165, 1928.

[6] S. Bose. Planck's law and the hypothesis of light quanta. *Z. Phys.*, 26:178, 1924.

[7] G. K. Campbell, J. Mun, M. Boyd, P. Medley, A. E. Leanhardt, L. G. Marcassa, D. E. Pritchard, and W. Ketterle. Imaging the Mott insulator shells by using atomic clock shifts. *Science*, 313(5787):649, Aug 2006.

[8] B. Capogrosso-Sansone, N. V. Prokof'ev, and B. V. Svistunov. Phase diagram and thermodynamics of the three-dimensional bose-hubbard model. *Phys Rev. B*, 75:134302, 2007.

[9] S. Chu. The manipulation of neutral particles. *Rev. Mod. Phys.*, 70(3):685, 1998.

[10] S. Chu, J. Bjorkholm, A. Ashkin, and A. Cable. Experimental observation of optically trapped atoms. *Phys. Rev. Lett.*, 57(3):314, 1986.

[11] S. Chu, L. Hollberg, J. Bjorkholm, A. Cable, and A. Ashkin. Three-dimensional viscous confinement and cooling of atoms by resonance radiation pressure. *Phys. Rev. Lett.*, 55(1):48, 1985.

[12] S. Clark and D. Jaksch. Signature of the superfluid to Mott-insulator transition the excitation spectrum of ultracold atoms. *New Journal Of Physics*, 8:160, Aug 2006.

[13] C. Cohen-Tannoudji. In M. Lévy, editor, *Cargése Lectures in Physics*, volume 2, page 347. Gordon and Breach, Amsterdam, 1968.

[14] C. Cohen-Tannoudji. Manipulating atoms with photons. *Rev. Mod. Phys.*, 70(3):707, 1998.

[15] M. Cristiani, O. Morsch, N. Malossi, M. Jona-Lasinio, M. Anderlini, E. Courtade, and E. Arimondo. Instabilities of a Bose-Einstein condensate in a periodic potential: an experimental investigation. *Optics Express*, 12(1):4, 2004.

[16] M. Cristiani, O. Morsch, J. H. Müller, D. Ciampini, and E. Arimondo. Experimental properties of Bose-Einstein condensates in one-dimensional optical lattices: Bloch oscillations, Landau-Zener tunneling, and mean-field effects. *Phys. Rev. A*, 65(6):063612, 2002.

[17] M. Dahan, E. Peik, J. Reichel, Y. Castin, and C. Salomon. Bloch oscillation of atoms in an optical potential. *Phys. Rev. Lett.*, 76(24):4508, 1996.

[18] F. Dalfovo, S. Giorgini, L. Pitaevskii, and S. Stringari. Theory of Bose-Einstein condensation in trapped gases. *Rev. Mod. Phys.*, 71(3):463, 1999.

[19] J. Dalibard and C. Cohen-Tannoudji. Dressed-atom approach to atomic motion in laser light: the dipole force revisited. *J. Opt. Soc. Am. B*, 2(11):1707, 1985.

[20] J. Dalibard and C. Cohen-Tannoudji. Laser cooling below the Doppler limit by polarization gradients: simple theoretical models. *J. Opt. Soc. Am. B*, 6(11):2023, 1989.

[21] K. Davis, M. Mewes, M. Andrews, N. van Druten, S. Durfee, D. Kurn, and W. Ketterle. Bose-Einstein condensation in a gas of sodium atoms. *Phys. Rev. Lett.*, 75(22):3969, 1995.

[22] G. Della Valle, M. Ornigotti, E. Cianci, V. Foglietti, P. Laporta, and S. Longhi. Visualization of coherent destruction of tunneling in an optical double well system. *Phys. Rev. Lett.*, 98:263601, 2007.

[23] B. DeMarco, C. Lannert, S. Vishveshwara, and T.-C. Wei. Structure and stability of Mott-insulator shells of bosons trapped in an optical lattice. *Phys. Rev. A.*, 71:063601, 2005.

[24] J. Denschlag, J. Simsarian, H. Häffner, C. McKenzie, A. Browaeys, D. Cho, K. Helmerson, S. Rolston, and W. Phillips. A Bose-Einstein condensate in an optical lattice. *J. Phys. B: At. Mol. Opt. Phys.*, 35:3095, 2002.

[25] D. Dunlap and V. Kenkre. Dynamic localization of a charged particle moving under the influence of an electric field. *Phys. Rev. B*, 34:3625, 1986.

[26] A. Eckardt. *private comunication.*

[27] A. Eckardt and M. Holthaus. Ac-induced superfluidity. *Europhysics Letters*, 80(5):50004, 2007.

[28] A. Eckardt and M. Holthaus. Dressed matter waves. *Journal of Physics: Conference Series*, 99:012007, 2008.

[29] A. Eckardt, T. Jinasundera, C. Weiss, and M. Holthaus. Analog of photon-assisted tunneling in a Bose-Einstein condensate. *Phys. Rev. Lett.*, 95:200401, 2005.

[30] A. Eckardt, C. Weiss, and M. Holthaus. Superfluid-insulator transition in a periodically driven optical lattice. *Phys. Rev. Lett.*, 95:260404, 2005.

[31] A. Einstein. *Sitzber. Kgl. Preuss. Akad. Wiss.*, page 261, 1924.

[32] A. Einstein. *Sitzber. Kgl. Preuss. Akad. Wiss.*, page 3, 1925.

[33] S. Fölling, A. Widera, T. Müller, F. Gerbier, and I. Bloch. Formation of spatial shell structure in the superfluid to Mott insulator transition. *Phys Rev. Lett.*, 97:060403, 2007.

[34] J. K. Freericks and H. Monien. Phase diagram of the Bose-Hubbard model. *Europhysics Letters*, 26:7, 1994.

[35] F. Gerbier. Boson Mott insulators at finite temperatures. *Phys Rev. Lett.*, 99:120405, 2007.

[36] F. Gerbier, A. Widera, S. Fölling, O. Mandel, T. Gericke, and I. Bloch. Interference pattern and visibility of a Mott insulator. *Physical Review A*, 72:053606, 2005.

[37] T. Gericke, F. Gerbier, A. Widera, S. Fölling, O. Mandel, and I. Bloch. Adiabatic loading of a Bose-Einstein condensate in a 3d optical lattice. *Jou*, page condmat/0603590, 2007.

[38] P. Gould, G. Ruff, and D. Pritchard. Diffraction of atoms by light: the near-resonant kapitza-Dirac effect. *Phys. Rev. Lett.*, 56(8):827, 1986.

[39] M. Greiner, O. Mandel, T. Esslinger, T. Hänsch, and I. Bloch. Quantum phase transition from a superfluid to a Mott insulator in a gas of ultracold atoms. *Nature*, 415:39, 2002.

[40] R. Grimm, M. Weidemüller, and Y. B. Ovchinnikov. Optical dipole traps for neutral atoms. *Advances in Atomic, Molecular and Optical Physics*, 42:95–170, 2000.

[41] E. Gross. *Nuovo Cimento*, 20:454, 1961.

[42] F. Grossmann, T. Dittrich, P. Jung, and P. Hänggi. Coherent destruction of tunneling. *Phys. Rev. Lett.*, 67:516, 1991.

[43] S. Haroche and C. Cohen-Tannoudji. Modified zeeman hyperfine spectra observed in H^1 and Rb^{87} ground states interacting with a nonresonant rf field. *Phys. Rev. Lett.*, 24(16):861, 1970.

[44] T.-L. Ho and Q. Zhou. Intrinsic heating and cooling in adiabatic processes for bosons in optical lattices. *Phys Rev. Lett.*, 99:120404, 2007.

[45] M. Holthaus. Coherent control of quantum localization. In W. Pötz and W. Schroeder, editors, *Coherent Control in Atoms, Molecules, and Semiconductors*, page 171. Kluwer, Dordrecht, 1999.

[46] K. Huang. *Statistical Mechanics*. John Wiley & Sons, Inc., third edition, 1966.

[47] A. Iucci, M. A. Cazalilla, A. F. Ho, and T. Giamarchi. Energy absorption of a Bose gas in a periodically modulated optical lattice. *Phys Rev. Lett.*, 94:130404, 2005.

[48] V. V. Ivanov, A. Alberti, M. Schioppo, G. Ferrari, M. L. C. M. Artoni, and G. M. Tino. Coherent delocalization of atomic wave packets in driven lattice potentials. *Phys. Rev. Lett.*, 100:043602, 2008.

[49] R. Iyer, J. Stewart Aitchison, M. Dignam, and C. de Sterke. Exact dynamic localization in curved AlGaAs optical waveguide arrays. *Opt. Expr.*, 15:3212, 2007.

[50] D. Jaksch, C. Bruder, J. Cirac, C. Gardiner, and P. Zoller. Cold bosonic atoms in optical lattices. *Phys. Rev. Lett.*, 81(15):3108, 1998.

[51] R. Jördens, N. Strohmaier, K. Günter, H. Moritz, and T. Esslinger. A Mott insulator of fermionic atoms in an optical lattice. *Nature*, 455:204–207, 2008.

[52] R. P. K. Sheshadri, H. R. Krishnamurthy and T. V. Ramakrishnan. Superfluid and insulating phases in an interacting-boson model: Mean-field theory and the RPA. *Europhysics Letters*, 22:257, 1993.

[53] B. J. Keay, S. Zeuner, S. J. Allen, K. D. Maranowski, A. C. Gossard, U. Bhattacharya, and M. J. W. Rodwell. Dynamic localization, absolute negative conductance, and stimulated, multiphoton emission in sequential resonant tunneling semiconductor superlattices. *Phys. Rev. Lett.*, 75(22):4102, 1995.

[54] W. Ketterle, S. Durfee, and D. Stamper-Kurn. Making, probing and understanding Bose-Einstein condensates. In M. Inguscio, S. Stringari, and C. Wieman, editors, *Bose-Einstein condensation in atomic gasses, Proceedings of the International School of Physics "Enrico Fermi", Course CXL*, page 67. IOS press, Amsterdam, 1999.

[55] C. Kittel. *Introduction to solid state physics*. John Wiley & sons, seventh edition, 1996.

[56] A. Klumpp, D. Witthaut, and H. J. Korsch. Quantum transport and localization in biased periodic structures under bi- and polychromatic driving. *J. Phys. A: Math. Theor.*, 40(10):2299–2311, 2007.

[57] C. Kollath, A. Iucci, T. Giamarchi, W. Hofstetter, and U. Schollwöck. Spectroscopy of ultracold atoms by periodic lattice modulations. *Phys. Rev. Lett*, 97:050402, 2006.

[58] L. Landau. *Phys. Z. Sowjetunion*, 2:46, 1932.

[59] P. Lett, R. Watts, C. Westbrook, W. Phillips, P. Gould, and H. Metcalf. Observation of atoms laser cooled below the Doppler limit. *Phys. Rev. Lett.*, 61(2):169, 1988.

[60] H. Lignier, C. Sias, D. Ciampini, Y. Singh, A. Zenesini, O. Morsch, and E. Arimondo. Dynamical control of matter-wave tunneling in periodic potentials. *Phys. Rev. Lett.*, 99:220403, 2007.

[61] H. Lignier, A. Zenesini, D. Ciampini, O. Morsch, E. Arimondo, S. Montangero, R. Fazio, and G. Pupillo. Trap modulation spectroscopy of the Mott-insulator transition in optical lattices. *submitted to PRL*, 2008.

[62] S. Longhi, M. Marangoni, M. Lobino, R. Ramponi, P. Laporta, E. Cianci, and V. Foglietti. Observation of dynamic localization in periodically curved waveguide arrays. *Phys. Rev. Lett.*, 96:243901, 2006.

[63] K. Madison, M. Fischer, R. Diener, Q. Niu, and M. G. Raizen. Dynamical Bloch band suppression in an optical lattice. *Phys. Rev. Lett.*, 81(23):5093, 1998.

[64] G. Mazzarella, S. M. Giampaolo, and F. Illuminati. Extended Bose Hubbard model of interacting bosonic atoms in optical lattices: From superfluidity to density waves. *Physical Review A*, 73:013625, 2006.

[65] H. Metcalf and P. van der Straten. *Laser Cooling and Trapping*. Springer, 2002.

[66] O. Morsch, M. Cristiani, J. H. Müller, D. Ciampini, and E. Arimondo. Free expansion of a Bose-Einstein condensate in a one-dimensional optical lattice. *Phys. Rev. A*, 66(2):021601, Aug 2002.

[67] O. Morsch, J. H. Müller, M. Cristiani, D. Ciampini, and E. Arimondo. Bloch oscillations and mean-field effects of Bose-Einstein condensates in 1d optical lattices. *Phys. Rev. Lett.*, 87(14):140402, 2001.

[68] O. Morsch and M. Oberthaler. Bose-Einstein condensates in optical lattices. *Rev. Mod. Phys.*, 78:179, 2004.

[69] C. Orzel, A. Tuchman, M. Fenselau, M. Yasuda, and M. Kasevich. Squeezed states in a Bose-Einstein condensate. *Science*, 291:2386, 2001.

[70] P. Pedri, L. Pitaevskii, S. Stringari, C. Fort, S. Burger, F. Cataliotti, P. Maddaloni, F. Minardi, and M. Inguscio. Expansion of a coherent array of Bose-Einstein condensates. *Phys. Rev. Lett.*, 87(22):220401, 2001.

[71] E. Peik, M. Dahan, I. Bouchoule, Y. Castin, and C. Salomon. Bloch oscillations of atoms, adiabatic rapid passage, and monokinetic atomic beams. *Phys. Rev. A*, 55(4):2989, 1997.

[72] W. Phillips. Laser cooling and trapping of neutral atoms. *Rev. Mod. Phys.*, 70(3):721, 1998.

[73] L. Pitaevskii. *Zh. Eksp. Teor. Fiz.*, 40:646, 1961.

[74] G. Pupillo, C. J. Williams, and N. Prokof'ev. Effects of finite temperature on the Mott-insulator state. *Phys. Rev A*, 73(1):013408, Jan. 2006.

[75] E. Raab, M. Prentiss, A. Cable, S. Chu, and D. Pritchard. Trapping of neutral sodium atoms with radiation pressure. *Phys. Rev. Lett.*, 59(23):2631, 1987.

[76] H. Sambe. Steady states and quasienergies of a quantum-mechanical system in an oscillating field. *Phys. Rev. A*, 7(6):2203, 1973.

[77] U. Schneider, L. Hackermüller, S. Will, T. Best, I. Bloch, T. A. Costi, R. W. Helmes, D. Rasch, and A. Rosch. Metallic and insulating phases of repulsively interacting fermions in a 3d optical lattice. *e-print*, 455:0809.1464v1, 2008.

[78] J. Shirley. Solution of the Schrödinger equation with a hamiltonian periodic in time. *Phys. Rev.*, 138(4B):B979, 1965.

[79] C. Sias, H. Lignier, Y. P. Singh, A. Zenesini, D. Ciampini, O. Morsch, and E. Arimondo. Observation of photon-assisted tunneling in optical lattices. *Phys. Rev. Lett.*, 100:040404, 2008.

[80] J. Slater. A soluble problem in energy bands. *Phys. Rev.*, 87(5):807, 1952.

[81] I. B. Spielman, W. D. Phillips, and J. V. Porto. Mott-Insulator transition in a two-dimensional atomic Bose gas. *Phys. Rev. L*, 98(8):080404, Feb 2007.

[82] T. Stöferle, H. Moritz, C. Schori, M. Köhl, and T. Esslinger. Transition from a strongly interacting 1d superfluid to a Mott insulator. *Phys. Rev. Lett.*, 92(13):130403, Mar 2004.

[83] D. van Oosten, P. van der Straten, and H. T. C. Stoof. Quantum phases in an optical lattice. *Phys. Rev. A*, 63(5):053601, Apr 2001.

[84] D. van Oosten, P. van der Straten, and H. T. C. Stoof. Mott insulators in an optical lattice with high filling factors. *Phys. Rev. A*, 67(3):033606, Mar 2003.

[85] D. Wineland and W. Itano. Laser cooling of atoms. *Phys. Rev. A*, 20(4):1521, 1979.

[86] B. Wu and Q. Niu. Landau and dynamical instabilities of the superflow of Bose-Einstein condensates in optical lattices. *Phys. Rev. A*, 64(6):061603, 2001.

[87] C. Zener. *Proc. R. Soc. London, Ser. A*, 137:696, 1932.

[88] W. Zwerger. Mott-Hubbard transition of cold atoms in optical lattices. *J. Opt. B: Quantum Semiclass. Opt.*, 5:S9, 2003.